

Locating Energy Levels of Lanthanide Ions in Inorganic Ionic Compounds

Andreas H. Krumpel



The research presented in this thesis was performed at the Radiation Detection & Medical imaging (RD&M) section of the department of Radiation, Radionuclides & Reactors (R³), Faculty of Applied Sciences, Delft University of Technology, Delft, The Netherlands. It was financially supported by the Dutch Technology Foundation STW.

Visiting address: Mekelweg 15, 2629 JB Delft, The Netherlands.

Locating Energy Levels of Lanthanide Ions in Inorganic Ionic Compounds

Proefschrift

ter verkrijging van de graad van doctor
aan de Technische Universiteit Delft,
op gezag van de Rector Magnificus prof. dr. K.C.A.M. (Karel) Luyben
voorzitter van het College voor Promoties,
in het openbaar te verdedigen op maandag 26 oktober 2009 om 10:00 uur

door
Andreas Heinz Krumpel

Diplom-Physiker
Westfälische Wilhelms-Universität Münster
geboren te Berlijn, Duitsland

Dit proefschrift is goedgekeurd door de promotor:

Prof. dr. P. Dorenbos

Copromotor:

Dr. E. van der Kolk

Samenstelling promotiecommissie:

| | |
|----------------------------|---|
| Rector Magnificus, | voorzitter |
| Prof. dr. P. Dorenbos | Technische Universiteit Delft, promotor |
| Dr. E. van der Kolk | Technische Universiteit Delft, copromotor |
| Prof. dr. F.M. Mulder | Technische Universiteit Delft |
| Prof. dr. P. Boutinaud | Ecole Nat. Supérieure de Chimie de Clermont-Ferrand |
| Prof. dr. C.W.E. van Eijk | Technische Universiteit Delft |
| Prof. dr. A. Meijerink | Universiteit Utrecht |
| Prof. dr. L.D.A. Siebbeles | Technische Universiteit Delft |
| Prof. dr. B. Wolterbeek | Technische Universiteit Delft |

© Copyright Shaker Publishing 2009

All rights reserved. No part of this publication may be reproduced, stored in a retrieval system, or transmitted, in any form or by any means, electronic, mechanical, photocopying, recording or otherwise, without the prior permission of the publishers.

Printed in The Netherlands.

ISBN 978-90-489-0377-5

Shaker Publishing BV
St. Maartenslaan 26
6221 AX Maastricht
Tel.: 043-3500424
Fax: 043-3255090
<http://www.shaker.nl>

To my family

Contents

| | |
|---|-----------|
| 1. Introduction | 1 |
| 1. Motivation | 1 |
| 2. Lanthanides and Their Luminescence – A Chronological Sketch | 2 |
| 3. Principles of Lanthanide Luminescence in Matter | 4 |
| 3.1. 4f and 5d Energy Level Splitting | 4 |
| 3.2. 4f-5d Transition Energy as a Function of Lanthanide and Host Crystal | 4 |
| 3.3. Charge Transfer | 5 |
| 3.4. Energy Transfer | 6 |
| 4. Energy Level Diagrams of Lanthanide Doped Compounds | 7 |
| 4.1. The Variation of Lanthanide 4f Ground States within an Energy Level Diagram | 7 |
| 4.2. 4f Level Location with Charge Transfer Energies | 8 |
| 4.3. Lanthanide 4f Energy Level Location by Means of Photoluminescence | 9 |
| 4.4. Temperature Dependent Luminescence Quenching | 10 |
| 4.5. Using and Explaining Thermoluminescence | 12 |
| 5. Thesis Outline | 12 |
| References | 14 |
| 2. Lanthanide 4f-Level Location in $AVO_4:Ln^{3+}$ ($A = La, Gd, Lu$) Crystals | 17 |
| 1. Introduction | 17 |
| 2. Experimental | 18 |
| 2.1. Sample Preparation | 18 |
| 2.2. Measurement Techniques | 19 |
| 3. Results | 20 |
| 3.1. $LaVO_4$ | 20 |
| 3.2. $GdVO_4 : 1\% Ce^{3+}$ and $LuVO_4 : 1\% Ce^{3+}$ | 21 |
| 3.3. $LaVO_4 : 1\% Pr^{3+}$, $GdVO_4 : 0.6\% Pr^{3+}$ and $LuVO_4 : 0.2\% Pr^{3+}$ | 23 |
| 3.4. $LaVO_4 : 1\% Eu^{3+}$, $GdVO_4 : 1\% Eu^{3+}$ and $LuVO_4 : 1\% Eu^{3+}$ | 26 |
| 3.5. $LaVO_4 : 1\% Tb^{3+}$, $GdVO_4 : 1\% Tb^{3+}$ and $LuVO_4 : 1\% Tb^{3+}$ | 29 |
| 4. Discussion and Conclusion | 32 |
| 4.1. Ln^{2+} 4f GS Energy Location | 33 |

| | |
|---|-----------|
| 4.2. Ln ³⁺ 4f GS Energy Location..... | 33 |
| Acknowledgements | 38 |
| References | 39 |
| | |
| 3. Lanthanide 4f-level Location in Lanthanide Doped and Cerium- Lanthanide Co-Doped NaLaF₄ by Photo- and Thermoluminescence | 41 |
| 1. Introduction | 41 |
| 2. Experimental | 42 |
| 2.1. Sample preparation..... | 42 |
| 2.2. Experimental techniques | 43 |
| 3. Results | 44 |
| 3.1. Photoluminescence..... | 44 |
| 3.2. Thermoluminescence..... | 48 |
| 3.2.1. Ln mono-doped NaLaF ₄ | 48 |
| 3.2.2. Ce-Ln co-doped NaLaF ₄ and NaLaF ₄ :2% Ce ³⁺ | 51 |
| 4. Discussion | 52 |
| 4.1. Photoluminescence and Energy Level Diagram | 52 |
| 4.1.1. Ln ²⁺ 4f GSE location..... | 52 |
| 4.1.2. Ln ³⁺ 4f GSE location..... | 53 |
| 4.2. Electron- and hole-traps | 53 |
| 4.3. Thermoluminescence..... | 54 |
| 4.3.1. Activation Energy..... | 55 |
| 4.3.2. Ce-Ln co-doped NaLaF ₄ | 56 |
| 4.3.3. Ln mono-doped NaLaF ₄ | 58 |
| 5. Conclusion..... | 62 |
| Acknowledgements | 62 |
| References | 63 |
| | |
| 4. Controlled Electron and Hole Trapping in YPO₄:Ce³⁺,Ln³⁺ and LuPO₄:Ce³⁺,Ln³⁺ (Ln = Sm, Dy, Ho, Er, Tm) | 65 |
| 1. Introduction | 65 |
| 2. Experimental | 66 |
| 2.1. Sample Preparation..... | 66 |
| 2.2. Measurement Techniques..... | 67 |
| 3. Results | 68 |
| 3.1. X-Ray Excited Emission Spectra | 68 |
| 3.2. VUV / UV Excitation Spectra | 68 |

| | |
|---|------------|
| 3.3. Thermoluminescence Studies..... | 76 |
| 4. Discussion | 80 |
| 4.1. Estimation of Exciton Creation And Band Gap Energy..... | 80 |
| 4.2. Charge Transfer Transitions..... | 81 |
| 4.3. Thermoluminescence Activation Energies..... | 82 |
| 4.4. Dependence of Ln ²⁺ Level Location on Experimental Method | 84 |
| 5. Conclusions | 85 |
| Acknowledgements | 85 |
| References | 87 |
| | |
| 5. Charge Transfer Transitions in the Transition Metal Oxides $ABO_4:Ln^{3+}$ and $APO_4:Ln^{3+}$ ($A = La, Gd, Y, Lu, Sc$; $B = V, Nb, Ta$; $Ln = Lanthanide$) | 89 |
| 1. Introduction | 89 |
| 2. Knowledge on CT Energies..... | 91 |
| 2.1. CT Energy and Related Numerical Parameters..... | 91 |
| 2.1.1. The Model of Jørgensen | 91 |
| 2.1.2. The Model of Boutinaud | 92 |
| 2.2. The Zig-Zag Curve of Binding Energies..... | 93 |
| 2.2.1. The Model of Dorenbos..... | 93 |
| 2.2.2. The Model of Nakazawa | 94 |
| 2.3. Relationship between IVCT Energy and 4f Electron Binding Energy | 95 |
| 3. Characterization and Analysis of the $ABO_4:Ln^{3+}$ System | 98 |
| 3.1. The Crystal Structures of the ABO_4 Compounds..... | 98 |
| 3.2. Energy of Charge Transfer from the Valence Band to Eu^{3+} | 100 |
| 3.3. The Energy of the $Pr^{3+} - B^{5+}$ Inter-Valence Charge Transfer | 104 |
| 3.4. The Band Gap Energy and its Relationship with Electronegativity and Ionization Potentials | 106 |
| 3.4.1. The Band Gap of Transition Metal Oxides | 106 |
| 3.4.2. The Band Gap of Non-Metal Orthophosphates..... | 109 |
| 4. Conclusion..... | 109 |
| Acknowledgements | 110 |
| References | 111 |
| | |
| Summary..... | 115 |

| | |
|-----------------------------------|-----|
| Samenvatting | 119 |
| List of Publications | 123 |
| Acknowledgements | 125 |
| Curriculum Vitae | 127 |

Chapter 1

Introduction

1. Motivation

Light has fascinated people at all times and has played a central role both in religion and philosophy in all cultures of the world. It was always assumed that there is a relationship between light and color and the understanding of both has changed as time passed. In the world picture of modern science, one consequence of the European *Enlightenment*, light is electromagnetic radiation that exhibit properties which can be described altogether only with the help of two mathematical approaches that are used for widely different concepts, namely particles and waves. Color on the other hand derives from the spectrum of light and is a property of the visual perception of an individual. Within this view an impressive technological control over light and color has been achieved which shows itself around us in everyday life. One broad research topic in the broad field of light technology, or photonics, deals with luminescent materials. A phosphor¹ or luminescent material is by definition a solid that “converts certain types of energy into electromagnetic radiation over and above thermal radiation” [1]. Such solids can be found among the transition metal compounds and the rare earth compounds of different types. A large variety of phosphors for various technological applications is known and the optical properties of the phosphors can be explained by the help of scientific models. Many phosphors nowadays are lanthanide (Ln) activated semi-conductor and insulator materials due to their serviceable luminescent properties, above all with regard to the generation and amplification of light.

In the present thesis an empirical model for semi-conductor and insulator materials with an Ln activator is used that not only explains the optical properties of phosphors but helps as well to find hitherto unknown materials with selected photoluminescence, thermoluminescence or charge carrier trapping properties for specific technological applications.

One objective of the present thesis was to localize the Ln 4f levels in different materials relative to the valence band (VB) and the conduction band (CB) by means of

¹ The name *phosphor* is of Greek origin and means *light-* (phos) *bearing* (phoros)

temperature- (T -) dependent photoluminescence (PL) spectroscopy and (wavelength resolved) thermoluminescence (TL). Another objective was to study possible regularities when going from one type of compound to another one. In this context I have not only analyzed own measured data but I have compared as well different models which all aim at explaining the very same phenomenon.

2. Lanthanides and Their Luminescence – A Chronological Sketch

Lanthanides are shiny and silvery-white, relatively soft, and reactive metals. It took more than 160 years until all of them were discovered, starting in 1787 when C.A. Arrhenius found a black stone in the vicinity of Ytterby (Sweden) from which several lanthanides could be isolated [2]. A hundred years later, all lanthanides were known except for one. Brauner announced in 1902 that for completion of the periodic behavior only nine elements would be missing up to uranium; among these nine elements he mentioned an element, “probably the trivalent element of a radioactive rare earth”, that he called “Ekalanthan”, and which he expected to have an approximated atomic weight of $230 \text{ g}\cdot\text{mol}^{-1}$ [3]. 45 years later, Marinsky *et al.* identified the last lanthanide, promethium (standard atomic weight: $145 \text{ g}\cdot\text{mol}^{-1}$), as a fission product of uranium [4]. There are mainly two reasons why the discovery took so long: Though being abundant in nature, lanthanides can be found only in very small concentrations in numerous rocks. In addition, they all behave similar in complex formation and solubility making it difficult to separate them. Their popularity in modern technology is due to the exceptional luminescence properties: All lanthanides, except for cerium, show atomic-like sharp line absorption and emission which has been observed already in the mid of the 19th century by Robert Bunsen on didymium that turned out to be a mixture of lanthanide elements [5]. First scientific explanations of some of these properties were given in the course of the development of quantum mechanics already in the twenties and thirty something of the 20th century. It became apparent that the dominant oxidation state of the lanthanides is (III) and that the electron configuration of a trivalent lanthanide ion is of the form $[\text{Xe}]4f^n$ [6, 7, 8]. Thus, lanthanides are f-block elements (apart from Lu which is a d-block element) characterized by the filling of the 4f electron shell. It was observed that parallel to the filling of the 4f electron shell also the atomic number increases. The increase of electrons and protons in equal shares causes the Ln^{3+} ions to decrease in size, an effect known as lanthanide contraction [9, 10, 11]. The small chemical differences between the lanthanides are down to the fact that only the outer 5s and 5p orbitals, which are equally filled for all lanthanides, contribute in chemical bonding and interactions with the neighboring ions.

At the beginning of the 1930's many physicists believed that the sharp line absorption and emission may rather be due to electronic transitions within the 4f electron shells [6, 7, 12, 13] rather than due to alternative transitions such as from the

Lanthanides and Their Luminescence – A Chronological Sketch

inner 4f shell to the outer 5d – 6s shells [14]. The 4f electron shell of an Ln^{3+} dopant ion is well shielded from the crystal field by the energetically higher lying s, p and d orbitals. Therefore, 4f-4f transitions do not contribute to chemical bonding and thus have a negligible effect on the metal-to-ligand distance, which would explain, within the configurational coordinate diagram, why the sharp lines positions in the luminescence spectra of Ln^{3+} ions in crystals and solutions resemble those of the free ions. Intraconfigurational transitions, however, are formally forbidden by the Laporte rule [15], and hence it has to be explained why the observed sharp lines are so strong in intensity. Although the 4f electrons are well shielded from the environment it was assumed that the crystal field could still have an effect of the 4f-4f transition probability [6]. Van Vleck suggested in 1937 that the presence of the forbidden 4f-4f transitions in the spectra might be due to “(I) quadrupole radiation; (II) magnetic dipole radiation; and (III) electric dipole radiation, caused by distortion of the electronic motion by the crystalline fields, so that the selection rules for the free atom no longer apply” [8]. The two first types of radiation occur also in the free ions. The third type of radiation, though, only appears in material in the following two cases: “(IIIa) The crystalline field does not have a centre of symmetry even at equilibrium position; (IIIb) The departures from holohedral symmetry are due entirely to atomic vibrations” [8]. In case (IIIa) the uneven components of the crystal field mix the 4f wave functions with small amounts of opposite-parity wave functions (as 5d). The atomic vibrations, case (IIIb), are found to have only a very weak influence [16]. Van Vleck gave a quantum mechanical solution to the problem of the strength of the sharp lines in the absorption and emission spectra even though his method had little impact on the development of atomic theory [17]. But one major problem was not solved yet: The large number of levels inside the 4f configuration that has been observed for several Ln ions [14, 16, 18]. At that time no theory was available that could describe the electronic structure and the resultant optical spectra; the mechanism was understood only qualitatively. A theoretical description of the 4f level configuration was developed in the period that followed by several researchers, particularly by Racah [15, 19, 20, 21]. As late as the early 1950's the sharp absorption and emission lines in the visible region could be ascribed to transitions within particular $4f^n$ configurations [22, 23, 24], whereas the more intense and somewhat broader lines at higher energies were assigned to parity-allowed interconfigurational $4f^n \leftrightarrow 4f^{n-1} 5d^1$ (4f-5d or 5d-4f) transitions [17]. The first energy level diagram displaying the 4f levels of the di- and trivalent free Ln ions in the infra-red (IR), visible and ultra-violet (UV) region of the spectrum was presented by Dieke in 1963 [25].

3. Principles of Lanthanide Luminescence in Matter

3.1. 4f and 5d Energy Level Splitting

The perturbation of the Ln 4f levels caused by the crystal field is rather weak compared to the Coulomb interaction between the electrons and spin-orbit coupling [26]. The Coulomb interaction between the electrons within the 4f shell has the largest contribution to the energy splitting; it produces terms separated from each other in the order of 10^4 cm^{-1} [27]. Each of these terms is then split further in the order of 10^3 cm^{-1} into several levels by the spin-orbit interaction. All these levels form the 4f configuration of the free Ln ions and each level can be characterized with the symbol $^{2S+1}L_J$, where **S** is the total spin, **L** the total orbital angular momentum, and **J** the total angular momentum of the 4f electrons. When the Ln ions are put into a host material, the crystal field not only affects the strength of the intraconfigurational 4f-4f transitions as mentioned in the previous section but also brings about an additional splitting of the single 4f states that depends on the site symmetry of the Ln ions [26]. Although the 4f electrons are well shielded from the crystal field, this splitting may be up to several tenths of electron volts [28].

The Ln 5d energy levels are largely perturbed by the crystal field. The magnitude of the splitting of the 5d levels depends strongly on the shape and the size of the anion polyhedron coordinating the Ln dopant ion [41]. In LaCl_3 , e. g., the crystal field splitting is 0.69 eV [42], whereas in $\text{Y}_3\text{Al}_5\text{O}_{12}$ it is 3.35 eV [44]. The dependence between the shape of the coordinating polyhedron and the crystal field splitting can be explained qualitatively within the point charge electrostatic model [26, 41, 42, 43, 44].

3.2. 4f-5d Transition Energy as a Function of Lanthanide and Host Crystal

The lowest 4f-5d transition energy varies irregularly with the number of electrons in the 4f shell when going from La, Ce, to Lu. Figure 1 shows that this variation reveals a characteristic curve. The amount of variation, that is the shape of the curve, is about the same for the neutral, singly, doubly or triply ionized lanthanides [45, 46]. When a Ln ion is doped in a host crystal *A*, the lowest 4f-5d transition energy is lowered, compared to that energy in the gaseous ion, by an amount of energy that is called spectroscopic redshift $D(A)$. The shape of the curve, however, remains the same again as can be seen in Figure 1. Dorenbos found that the value of $D(A)$ is about the same for every Ln ion that is doped in the same compound [45]. In Figure 1 this is shown by the lowered curves for CaF_2 and LiYF_4 . That means, once the lowest 4f-5d energy difference of a specific Ln ion is known in a given compound, the 4f-5d energy differences of all other Ln ions doped in that same compound can be predicted with an accuracy less than a tenth of an electron volt [45]. The spectroscopic redshift tends to increase in the order: Fluorides < chlorides < bromides < iodides < oxides < sulfides. It

can range from about 0.82 eV for KMgF_3 up to 4.13 eV in MgSc_2S_4 [47]. But also within each family of compounds the variation is quite large: Within the fluorides, e. g., Cs_2NaYF_6 shows a redshift of about 2.16 eV, whereas the value for LaF_3 is half of it, viz. 1.08 eV [47].

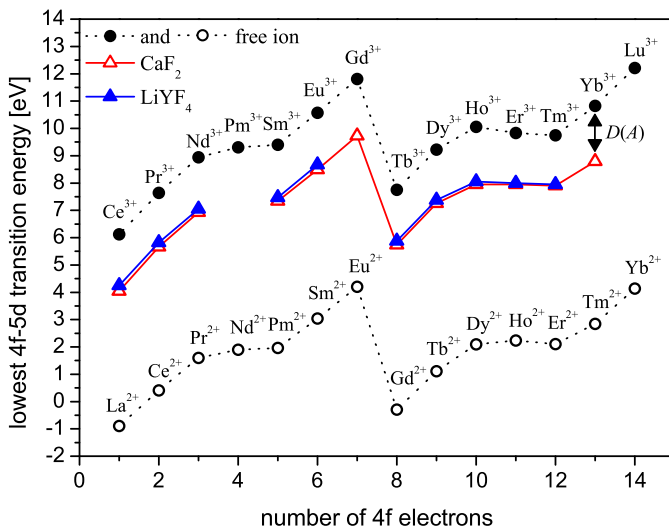


Fig. 1. Predicted lowest energy spin-allowed 4f-5d transition energies of the gaseous (free) Ln^{3+} [45] and Ln^{2+} [48] ions together with experimental values for the first electric dipole-allowed transition for the Ln^{3+} dopant ions in CaF_2 and LiYF_4 [45]. The arrow marked $D(A)$ indicates the redshift.

3.3. Charge Transfer

Beside the absorption and emission lines which can be attributed exclusively to transitions inside the Ln electron configurations, the excitation and emission spectra of Ln-containing compounds show sometimes broad bands which can be explained assuming charge transfer (CT) transitions between the Ln dopant and a host ion or between the host ions themselves. An example for the latter type of transition can be found in the excitation spectra of the orthovanadates with formula $\text{AVO}_4:\text{Ln}^{3+}$ and in the emission spectra of $\text{AVO}_4:\text{Ce}^{3+}$ ($A = \text{La}, \text{Gd}, \text{Lu}$) in which the VO_4^{3-} group transition can be regarded as a transition between the O^{2-} and the V^{5+} ions (see Chapter 2). Transitions between Ln ions and host ions can occur in both directions, either from the ligand to the Ln^{3+} ion, usually referred to as an Ln^{3+} CT (see also section 4.2.), or from the Ln^{3+} to a host cat-ion, a so-called inter valence charge transfer (IVCT). IVCT transitions have been observed so far only in the transition metal oxides [29]. The

conditions under which both host \rightarrow Ln and Ln \rightarrow host CT transitions occur are discussed in more detail in Chapter 5.

Even though no theory exists at the present that can describe such CT transitions, the CT energies can still be used in order to construct energy level diagrams that are able to predict the luminescence properties of particular Ln ions in a compound. This will be shown in Section 4.

3.4. Energy Transfer

An energy transfer (ET) from a sensitizer ion (S) to an impurity (activator) ion (A) brings about a concerted transition between the energy levels of both ions in such a way that S loses its energy whereas A gains energy and becomes excited (*):



S can either be another impurity ion or the host lattice. We consider the case where no photon is emitted and reabsorbed during the ET (non-radiative ET). The transition probability for such an ET can be expressed with the help of Fermi's golden rule,

$$P_{SA} = (2\pi/\hbar) \left| \langle S + A^* | \hat{H} | S^* + A \rangle \right|^2 \rho(\Delta E_S) \Big|_{\Delta E_S = \Delta E_A}, \quad (2)$$

where the states $|S^* + A\rangle$ and $|S + A^*\rangle$ are ascribed to the situations before and after the CT as shown in equation (1); $\rho(\Delta E_S)$ is the density of states at the energy of the initial state $|S^* + A\rangle$; ΔE_S is the energy difference between the ground state and the excited state of S; accordingly, the term ΔE_A means the corresponding energy of A. ΔE_S and ΔE_A must be approximately equal because of energy conservation (resonance condition). The Hamilton-operator, \hat{H} , can be written as the sum of all the Coulomb interactions of the outer electrons and the nucleus of S with those of A. By expanding this \hat{H} in a Taylor series about the vector \mathbf{R}_{SA} , the distance between the nuclei of S and A, it becomes apparent that an electric dipole-dipole interaction is the dominant Coulomb interaction [30]. As the electric field of an oscillating dipole falls off as r^{-3} , it can be seen already in view of equation (2) that in the case of an electric dipole-dipole interaction the transfer probability becomes proportional to R_{SA}^{-6} :

$$P_{SA} \propto R_{SA}^{-6} \quad (\text{electric dipole-dipole interaction})$$

The same holds for the quantum efficiency [31]. This type of interaction has a range in the order of 1 nm. Only in the special case where S is a line emitter and A is a broad-band absorber the ET still might take place over somewhat longer distances [1].

When effects of the electron spin are taken into consideration by writing the initial and final states in equation (2) as products of space and spin wave functions, the

Energy Level Diagrams of Lanthanide Doped Compounds

transition probability becomes proportional to [30]

$$P_{SA} \propto \exp(-2R_{SA}/L) \quad (\text{exchange effects})$$

where L is an effective average Bohr radius for the excited and ground states of S and A. The exchange effects are due to the selection rules of the spin wave functions in the exchange integrals of the matrix element of \hat{H} [30]. As the transfer probability falls off exponentially with R_{SA} , it only is effective for distances smaller than 1 nm. Because of this small distance which is required both for the electric dipole-dipole and the exchange interaction, S and A have to be nearest neighbors which means that at least one of the two ions has to be present in the material in rather high concentrations.

A special case of an ET is the cross-relaxation in which S transfers only a part of its energy to A [31].

An ET as described by equation (2) can be detected in PL spectroscopy either (i) in an excitation spectrum monitoring A emission that exhibits excitation peaks of A as well as of S, or (ii) in an emission spectrum that shows emission from A during excitation in energy states of S. In addition, a non-radiative, resonant ET can be identified within decay measurements with respect to the shape of the decay curve of A (showing a rise at the beginning) and the shortened decay time of the S emission.

4. Energy Level Diagrams of Lanthanide Doped Compounds

Diagrams showing the various energy levels of the $\text{Ln}^{3+}:4f^n$ configuration both of free and dopant ions are well known and widely used in Ln PL spectroscopy [25, 32, 33]. An energy level diagram combining both the electronic band structure of the host and the localized 4f levels of single Ln ions is theoretically not feasible yet. The differences between the energy of an electron in a localized state and in a delocalized band, however, can be measured (see section 4.2.). And they still can be depicted in one and the same energy difference diagram. Pieter Dorenbos [34, 35, 36, 37, 38] has presented diagrams which are not based on the calculated energy levels of a quantum mechanical system but which correlate energy differences relative to a common ionization level such like the CB or the vacuum.

4.1. The Variation of Lanthanide 4f Ground States within an Energy Level Diagram

It has been found experimentally that the energy difference between the lowest 5d level of a divalent lanthanide dopant and the CB, that is, the ionization energy of the 5d electron, is quite constant when going from La^{2+} to Gd^{2+} , and it decreases by about 0.5 eV when going from Gd^{2+} to Yb^{2+} [34]. This trend of the 5d electron ionization energy is indicated in Figure 2 with the help of the dashed line below the bottom of the CB. Together with the information on the lowest energy 4f-5d transition energies of the

divalent lanthanide ions displayed in Figure 1, the energy differences between the Ln^{2+} 4f ground states and the bottom of the CB (or the top of the VB) can be predicted as shown in Figure 2.

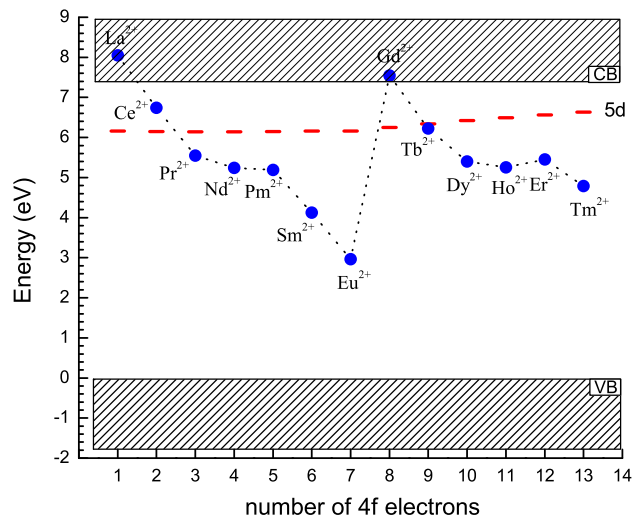


Fig. 2. Predicted energy differences between the 4f ground states (filled circles) and the bottom of the conduction band (CB). The values are based on the ionization energy of the 5d electron [34, 49] and the first 4f-5d transitions of the gaseous (free) Ln^{2+} [48] ions shown in Figure 1, assuming a spectroscopic redshift of 1 eV in this example.

4.2. 4f Level Location with Charge Transfer Energies

Figure 3 shows a comparison between an energy level diagram based on energy differences and a configurational coordinate diagram. In view of the width of the measured $\text{O}^{2-} \rightarrow \text{Ln}^{3+}$ CT excitation bands it can be concluded that the initial state in this CT absorption is close to the top of the VB [34]. The same can be assumed for the host absorption bands. The fact that the CT excitation bands of Sm^{3+} , Eu^{3+} , Tm^{3+} and Yb^{3+} luminescence have a similar width indicate that the most probable final state in the CT absorption is not one of the higher 4f levels but rather the $\text{Ln}^{2+}:4f$ GS [34]. Figure 3 illustrates, using the example of thulium, one of the problems we have to be aware of when using CT excitation band energies for energy level location. The CT energy that we measure corresponds, within a configurational coordinate diagram, to a transition that starts from the lowest vibrational level of the ground state parabola

Energy Level Diagrams of Lanthanide Doped Compounds

belonging to the electron on the anion ligand (point A in Figure 3) and that ends on the highest amplitude of an upper vibrational level (i.e. the edge) of the excited state parabola of Ln^{2+} (point B in Figure 3). After such an excitation, though, the lattice is not in equilibrium and the lattice ions will relax to the new equilibrium-positions belonging to the final state (point C in Figure 3). This relaxation energy, E_R , is represented by the grey area inside Figure 3; it can be up to several tenths of electron volts, corresponding to the width of the CT excitation bands.

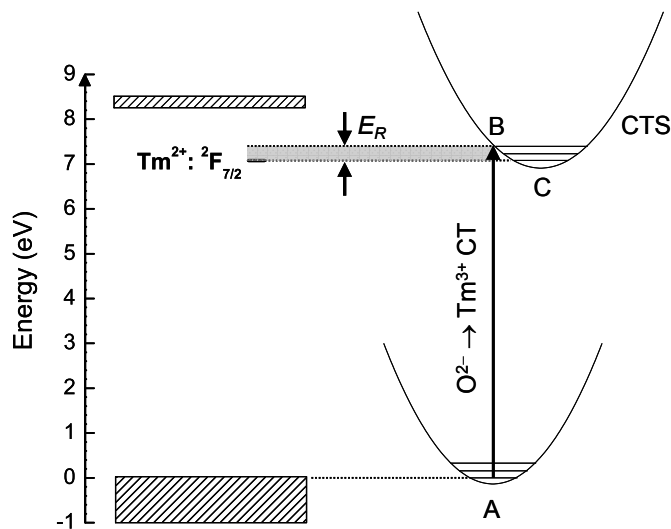


Fig. 3. Energy level diagram (left side) of $\text{LuPO}_4:\text{Tm}^{3+}$ and configurational coordinate diagram indicating the $\text{O}^{2-} \rightarrow \text{Tm}^{3+}$ CT energy as used for energy level location. Due to relaxation processes, the energy of the charge transfer state (CTS) will be lowered by an amount ΔE indicated in form of the grey area.

4.3. Lanthanide 4f Energy Level Location by Means of Photoluminescence

Using the example of $\text{LuPO}_4:\text{Ce}^{3+}, \text{Tm}^{3+}$, Figure 4 shows how a PL excitation spectrum can be converted into an energy level diagram. In this way, excitation spectra can reveal information on useful energies as for instance the band gap, host-guest and guest-host excitation bands, or 4f-4f and 4f-5d of the Ln guest. These two latter types of transitions that occur inside the Ln ion, however, do not place the 4f and 5d levels of the Ln dopant relative to the VB and the CB of the host. The 4f-5d transition of Ce^{3+} for instance, that can be seen in the excitation spectrum in Figure 4, is therefore drawn

within the energy level diagram on the left inside an oval frame. This oval frame indicates that we do not know the energetic location of the Ce^{3+} levels inside the diagram. As a matter of fact, the energetic locations of the energy levels of the trivalent Ln ions in such diagrams are much more difficult to establish than those of the divalent ions. As will be shown in chapters 2 and 5 of this thesis, the IVCT band energy might give information on the location of the trivalent lanthanide ground state energy relative to the CB. In addition to the excitation spectra, both the presence and the absence of emission bands may give information as well on the energy level configuration of the material.

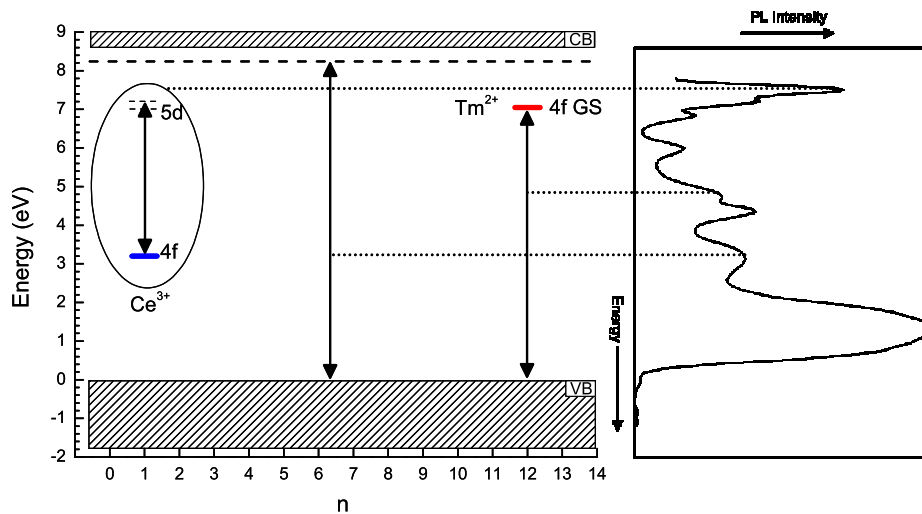


Fig. 4. Diagram displaying energy differences that are identified in the excitation spectrum of $\text{LuPO}_4:\text{Ce}^{3+}, \text{Tm}^{3+}$. From left to right we show inside the diagram: The 4f-5d transitions of Ce^{3+} , the exciton creation energy (dashed horizontal line at 8.2 eV), and the $\text{O}^{2-} \rightarrow \text{Tm}^{3+}$ CT. n represents the number of electrons in the 4f shell of the trivalent lanthanides.

The experimental information on the energy difference between the Tm^{2+} ground state and the bottom of the CB in $\text{LuPO}_4:\text{Tm}^{3+}$ can be used now together with the zig-zag curve shown in Figure 2 in order to predict the 4f ground state locations of all other possible lanthanide dopants in LuPO_4 . As shown in Figure 2, the shape of the zig-zag curve does not depend on the host crystal.

4.4. Temperature Dependent Luminescence Quenching

Once the energetic locations of the lanthanide 4f ground states are known within the

Energy Level Diagrams of Lanthanide Doped Compounds

energy level diagram, the locations of the higher excited 4f states are known as well with the help of the Dieke diagram [25]. In order to see how the energy level diagrams can explain the luminescence properties of a particular compound, we look at an example. Figure 5 shows the energy level diagram of $\text{GdVO}_4:\text{Tb}^{3+}$ as established in Chapter 2 of this thesis. The 4f ground state of Tb^{3+} has been located with the help of the observed IVCT excitation energy (see Chapter 2), i.e., the energy difference between the $\text{Tb}^{3+}:\text{F}_6$ ground state and the bottom of the CB. Using the Dieke diagram, it follows that the ${}^5\text{D}_4$ state is located within the energy level diagram somewhat below the CB, whereas the ${}^5\text{D}_3$ state is located inside the CB (see Figure 5). An electron that is excited to this latter ${}^5\text{D}_3$ state will ionize via the CB so that we do not expect to see ${}^5\text{D}_3 \rightarrow {}^7\text{F}_6$ emission. And indeed, the emission spectrum of $\text{GdVO}_4:\text{Tb}^{3+}$ shows emission from ${}^5\text{D}_4$ but no emission from the ${}^5\text{D}_3$ (see Chapter 2). The ${}^5\text{D}_4$ state, on the other hand, is located quite close to the bottom of the CB. By heating up the material, additional energy could be transferred to the ${}^5\text{D}_4$ electron so that it might be ionized via the CB as well. The experiment confirms that: The ${}^5\text{D}_4 \rightarrow {}^7\text{F}_6$ luminescence can be quenched by increasing the temperature, see Figure 5.

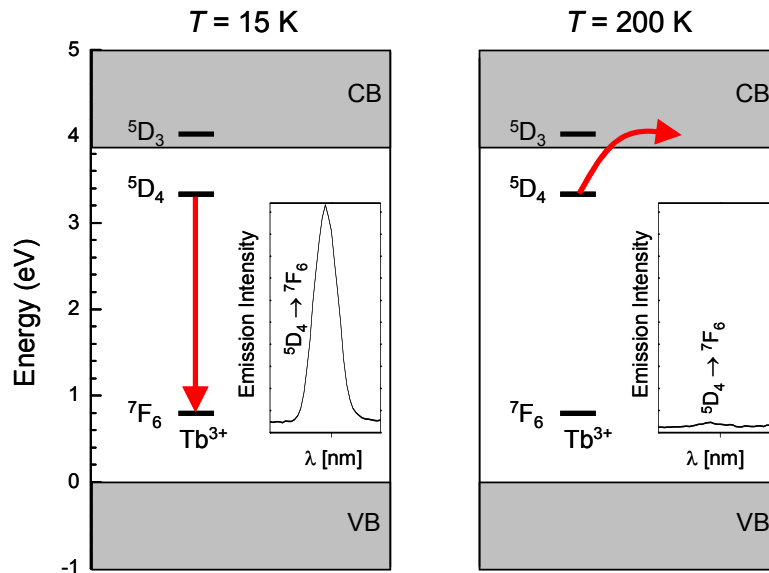


Fig. 5. Energy level diagram of $\text{GdVO}_4:\text{Tb}^{3+}$ together with the emission spectrum (inset) showing the ${}^5\text{D}_4 \rightarrow {}^7\text{F}_6$ emission of Tb^{3+} at 15 K (on the left) and at 200 K (on the right); VB = valence band; CB = conduction band.

When we assume that the ${}^5\text{D}_4$ electron, after being thermally ionized to the CB,

relaxes non-radiatively to the ground state of Tb^{3+} , we can make use of a simple model that enables us to derive from the behavior of the temperature dependent luminescence quenching an energy difference between the $^5\text{D}_4$ state and the bottom of the CB. This energy difference, the so-called activation energy, is usually in line with the expected energy difference based on the location of the 4f ground state and the Dieke diagram.

4.5. Using and Explaining Thermoluminescence

As already mentioned in the previous section, we have also used TL in order to localize the Ln 4f levels. TL plays an important role in archaeology (luminescence dating) and in radiation protection (dosimeters). So far, TL properties of materials could not be predicted or modeled beforehand, and the materials that are used these days were discovered accidentally. Now, for $\text{APO}_4:\text{Ce}^{3+},\text{Ln}^{3+}$ ($A = \text{Y}, \text{Lu}$) it could be shown [39, 40] that the energy level diagrams proposed by Dorenbos are able to explain the presence of Ln-related glow peaks. Actually, these glow peaks were predicted based on the energy level diagrams for $\text{YPO}_4:\text{Ln}^{3+}$ and $\text{LuPO}_4:\text{Ln}^{3+}$. The Ce-Ln co-doped materials were synthesized afterwards in order to verify the expectations. The idea is simple: Taking again $\text{LuPO}_4:\text{Ce}^{3+},\text{Tm}^{3+}$ as an example, we see from Figure 4 that the 4f GS of Tm^{2+} , which is lower in energy than the 5d states of Tm^{2+} (see Figure 2), is located inside the forbidden band gap. This implies that the Tm^{3+} ion should be able to trap an electron from the CB forming a stable Tm^{2+} ion. Heating up the material could provide enough energy in order to excite the electron from the 4f GS of Tm^{2+} into the CB. This freed electron might recombine then with a trapped hole at a luminescence centre producing TL. In view of the energy level diagram of $\text{LuPO}_4:\text{Ln}^{3+}$ it can be argued that Ce^{3+} might actually be such a luminescence centre able to trap a hole. So far, these are the expectations within the scope of the model. And indeed, in the experiment we really could identify Ce^{3+} luminescence at the temperature of the Tm-related glow peak. This is an exciting result as it opens possibilities for a TL technology, i.e., a technology where TL properties of materials can be predicted and materials properties can be designed beforehand. In addition to this, the activation energies which can be derived from the Ln-related glow peaks give a complementary information on the location of the Ln 4f levels: As shown in section 4.2. and Figure 3, the Ln^{3+} CT energy provides the energy difference between the top of the VB and an upper vibrational level of the Ln^{2+} 4f ground state. The initial state of the heat-supported CT in TL on the other hand is the 4f GS of the Ln^{2+} ion in equilibrium position (point C in Figure 3).

5. Thesis Outline

Chapter 2 presents a study on the orthovanadates with formula $\text{AVO}_4:\text{Ln}^{3+}$ ($A = \text{La}, \text{Gd}, \text{Lu} \mid \text{Ln} = \text{Ce}, \text{Pr}, \text{Eu}, \text{Tb}$). The vanadates belong to the transition metal oxides and have rather low band gap energies that depend on the size of the A^{3+} cation. Of these

Thesis Outline

materials we have recorded T-dependent PL excitation and emission spectra which provided us with enough information in order to construct energy level diagrams that explain the dependence of the luminescence properties on the Ln dopants for each host like the temperature dependent Pr^{3+} and Tb^{3+} luminescence quenching.

Chapter 3 presents both PL and TL measurements of $\text{NaLaF}_4:\text{Ce}^{3+},\text{Ln}^{3+}$ (Ln = Ce, Pr, Nd, Sm, Eu, Gd, Tb, Dy, Er, Tm). This study shows that the energy level diagram that has been constructed based on the energy differences identified in the PL spectra is not enough in order to explain the lanthanide-specific TL glow curves of both Ln mono- and Ce-Ln co-doped NaLaF_4 . In addition to the diagram two assumptions are needed, viz. the presence of two host related electron traps and the presence of V_{K} -centers.

In Chapter 4 we compare both PL and TL result of $\text{LuPO}_4:\text{Ce}^{3+},\text{Ln}^{3+}$ (Ln = Sm, Dy, Ho, Er, Tm) with the results of corresponding measurements done on $\text{YPO}_4:\text{Ce}^{3+},\text{Ln}^{3+}$. Due to the similarity in crystal structures we expected similar results for both types of materials. For both compounds the TL properties can be explained well with the help of the energy level diagrams. The diagrams that have been constructed based on both the PL spectra and the TL glow curves explain the differences between $\text{YPO}_4:\text{Ln}^{3+}$ and $\text{LuPO}_4:\text{Ln}^{3+}$ which are due to the different ionic radii of Y^{3+} and Lu^{3+} .

Chapter 5 analyzes the transition metal oxides $\text{ABO}_4:\text{Ln}^{3+}$ and the non-metal oxides $\text{APO}_4:\text{Ln}^{3+}$ ($A = \text{La, Gd, Y, Lu, Sc} \mid B = \text{V, Nb, Ta}$) with a view to systematic variations in important parameters as band gap, $\text{O}^{2-} \rightarrow \text{Ln}^{3+}$ CT energies, IVCT energies, etc. while going from one of these materials to another one. At the beginning of the 1970's, Jørgensen showed that the CT energy between a ligand and a central atom can be approximated roughly with the difference of the so-called optical electronegativities of these two ions. In this chapter we will show among other things how his simple equation can be modified in order to approximate the $\text{Pr}^{3+} \rightarrow B^{q+}$ ($B = \text{transition metal}$) inter-valence charge transfer (IVCT) and the $\text{O}^{2-} \rightarrow \text{Eu}^{3+}$ CT energies for the different $\text{ABO}_4:\text{Ln}^{3+}$ compounds.

References

- [1] Blasse G., Grabmaier B.C., *Luminescent Materials*, Springer-Verlag Berlin Heidelberg New York (1994), p. 1
- [2] Szabadvary F., *The History of the Discovery and Separation of the Rare Earths*, in: Handbook on the Physics and Chemistry of Rare Earths, edited by K.A. Gschneidner, Jr., and L. Eyring, Elsevier Science B.V. Amsterdam Lausanne New York, vol. **11** (1988) pp. 33-80
- [3] Brauner B., *Zeitschrift für anorganische Chemie*, **32** (1902) 1
- [4] Marinsky J.A., Glendenin L.E., Coryell C.D., *J. Am. Chem. Soc.*, **69** (1947) 2781
- [5] Emsley J., *Nature's Building Blocks – An A-Z Guide To The Elements*, Oxford University Press (2003), ISBN: 0198503407
- [6] Freed S., *Phys. Rev.*, **38** (1931) 2122
- [7] Tomaschek R., *Physik. Z.*, **33** (1932) 878
- [8] van Vleck J.H., *J. Phys. Chem.*, **41** (1937) 67
- [9] Goldschmidt V.M., Barth T., Lunde G., *Skrifter utgitt av Det Norske Videnskaps-Akademi i Oslo*, **7** (1925) 1
- [10] Barth T., Lunde G., *Zeitschrift für Physikalische Chemie – Stochiometrie und Verwandtschaftslehre*, **121** (1926) 78
- [11] von Hevesy G., *Die Seltenen Erden vom Standpunkte des Atombaues*, Julius Springer Berlin (1927)
- [12] Bethe H., *Z. Physik*, **60** (1930) 218
- [13] Kramers H.A., *Proc. Acad. Sci. Amsterdam*, **32** (1929) 1176
- [14] Spedding F.H., *Phys. Rev.*, **37** (1931) 777
- [15] Condon E.U., Shortley G.H., *The Theory of Atomic Spectra*, Cambridge University Press, Cambridge (1935), ISBN: 0521092094
- [16] Blasse G., *Int. Revs Phys. Chem.*, **11** (1992) 71
- [17] Judd B.R., *Atomic Theory and Optical Spectroscopy*, in: Handbook on the Physics and Chemistry of Rare Earths, edited by K.A. Gschneidner, Jr., and L. Eyring, Elsevier Science

References

- B.V. Amsterdam Lausanne New York, vol. **11** (1988) pp. 81-195
- [18] Spedding F.H., *Phys. Rev.*, **46** (1934) 975
- [19] Racah, G., *Phys. Rev.*, **62** (1942) 186
- [20] Racah, G., *Phys. Rev.*, **62** (1942) 438
- [21] Racah, G., *Phys. Rev.*, **76** (1949) 1352
- [22] Hellwege K.H., Hellwege A.M., *Z. Phys.*, **131** (1951) 98
- [23] Hellwege K.H., Kahle H.G., *Z. Phys.*, **129** (1951) 62
- [24] Hellwege K.H., Kahle H.G., *Z. Phys.*, **129** (1951) 85
- [25] Dieke G.H., Crosswhite H.M., *Appl. Opt.*, **2** (1963) 675
- [26] Görrler-Walrand C., Binnemans K., *Rationalization of Crystal-Field Parametrization*, in: Handbook on the Physics and Chemistry of Rare Earths, edited by K.A. Gschneidner, Jr., and L. Eyring, Elsevier Science B.V. Amsterdam Lausanne New York, vol. **23** (1996) pp. 121-283
- [27] Werts M.H.V., *Sc. Progr.*, **88** (2005) 101
- [28] Sheng K.C., Korenowski G.M., *J. Phys. Chem.*, **92** (1988) 50
- [29] Boutinaud P., Cavalli E., Bettinelli M., *J. Phys.: Condens. Matter*, **19** (2007) 386230
- [30] Dexter D.L., *J. Chem. Phys.*, **21** (1953) 836
- [31] Ronda C.R. (ed.), *Luminescence – From Theory to Applications*, Wiley-VCH Weinheim (2008), ISBN: 978-3-527-31402-7
- [32] Wegh R.T., Meijerink A., Lamminmäki R.-J., Hölsä J., *J. Lumin.*, **87-89** (2000) 1002
- [33] Ogasawara K., Watanabe S., Sakai Y., Toyoshima H., Ishii T., Brik M.G., Tanaka I., *Jap. J. Appl. Phys.*, **43** (2004) L611
- [34] Dorenbos P., *J. Phys.: Condens. Matter*, **15** (2003) 8417
- [35] Dorenbos P., *J. Lumin.*, **108** (2004) 301
- [36] Dorenbos P., *J. Lumin.*, **111** (2005) 89
- [37] Dorenbos P., *J. Lumin.*, **117** (2006) 147
- [38] Dorenbos P., *J. Lumin.*, **122** (2007) 315
- [39] Bos A.J.J., Dorenbos P., Bessière A., Viana B., *Rad. Meas.*, **43** (2008) 222
- [40] Krumpel A.H., Bos A.J.J., Bessière A., van der Kolk E., Dorenbos P., *Phys. Rev. B.*, **80**

(2009) 085103

- [41] Dorenbos P., *Phys. Rev. B*, **62** (2000) 15640
- [42] Dorenbos P., *Phys. Rev. B*, **62** (2000) 15650
- [43] Dorenbos P., *Phys. Rev. B*, **64** (2001) 125117
- [44] Dorenbos P., *J. Lumin.*, **99** (2002) 283
- [45] Dorenbos P., *J. Lumin.*, **91** (2000) 91
- [46] Brewer L., *J. Opt. Soc. Am.*, **61** (1971) 1666
- [47] Dorenbos P., *J. Lumin.*, **91** (2000) 155
- [48] Dorenbos P., *J. Phys.: Condens. Matter*, **15** (2003) 575
- [49] Dorenbos P., *J. Phys.: Condens. Matter*, **15** (2003) 2645

Chapter 2

Lanthanide 4f-Level Location in $AVO_4:Ln^{3+}$ ($A = La, Gd, Lu$) Crystals

Abstract

The spectral properties of $LaVO_4$, $GdVO_4$ and $LuVO_4$ crystals doped with Ce^{3+} , Pr^{3+} , Eu^{3+} or Tb^{3+} have been investigated in order to determine the position of the energy levels relative to the valence and conduction bands of the hosts along the trivalent and divalent lanthanide series. Pr^{3+} and Tb^{3+} ground state levels are positioned based on the electron transfer energy from those states to the conduction band, the so-called intervalence charge transfer (IVCT). This approach is compared and united with an alternative model that is based on electron transfer from the valence band to a lanthanide.

1. Introduction

Many lanthanide ($Ln = La, Ce, \dots, Lu$) doped orthovanadates of rare earth metals ($REVO_4:Ln^{3+}$; $RE =$ rare earth) are well known compounds for different applications as laser host crystals, solar cells or phosphor materials. Their luminescence properties depend strongly on the location of the 4f energy levels of the Ln dopants relative to the valence band (VB) and the conduction band (CB) of the host. Following up a previous work on $LaVO_4:Ln^{3+}$ [1], we have recorded temperature dependent photoluminescence emission and excitation spectra of $GdVO_4:Ln^{3+}$ and $LuVO_4:Ln^{3+}$ ($Ln = Ce, Pr, Eu, Tb$) crystals. The objective of this study was to construct energy level diagrams for the Ln doped orthovanadates of gadolinium and lutetium explaining the dependence of the luminescence properties on the Ln dopants for each host. Boutinaud *et al.* identified in $GdVO_4:Pr^{3+}$ and $LuVO_4:Pr^{3+}$ the ‘virtual recharge’ mechanism or intervalence charge transfer (IVCT), i.e. an electron transfer from Pr^{3+} to the VO_4^{3-} group [2]. The IVCT model of Boutinaud shows a linear correlation between the IVCT energy and the optical electronegativity of the transition metal cation divided by the shortest distance between the Ln dopant and the cation (here V^{5+}) to be reduced. The proposed

mechanism provides information on the 4f ground state (GS) energy of the trivalent Ln dopant ions relative to the VB and the CB and hence it is complementary to the Dorenbos model. This latter model relies on the observation that the energy difference between the Ln 4f ground state (GS) energy and the top of the VB reveals independently from the host a characteristic zig-zag shape when the number of electrons in the 4f shell increases from 1 (Ce^{3+} , La^{2+}) to 14 (Lu^{3+} , Yb^{2+}) [3]. This means that the knowledge of the absolute 4f GS energy location of only one Ln dopant ion, that is its location relative to the CB and the VB of the host matrix, suffices to predict the absolute 4f GS energy locations of all the other possible Ln dopants. The CT energies as well as the temperature quenching behaviour of some of the excitation and emission bands can provide indispensable information about the 4f GS energies of the Ln dopant ions relative to the electronic host states.

2. Experimental

2.1. Sample Preparation

All crystals were prepared by the flux growth method using $Pb_2V_2O_7$ as the solvent. Pure La_2O_3 , Lu_2O_3 , Gd_2O_3 , V_2O_5 , PbO and $Na_2B_4O_7$ were used as starting materials [4]. The composition of the growth mixtures was (in molar percent ratio): La_2O_3 (Gd_2O_3 , Lu_2O_3): V_2O_5 : PbO : $Na_2B_4O_7$ = 2.3: 31.5: 62.9: 3.3. The dopants were added as Eu_2O_3 , CeO_2 , Tb_4O_7 or Pr_6O_{11} with a Ln/La(Gd,Lu) = 1% nominal molar ratio. After careful mixing the starting mixtures were put in Pt crucibles and heated to 1270 °C in a horizontal programmable furnace. They were maintained at this temperature for 12 h (soaking time), then cooled to 800 °C at a rate of 1.8 °C and finally to room temperature at a rate of 15 °C. Transparent crystals in form of platelets having an average size $0.5 \times 2 \times 2$ mm³ were separated from the flux by dissolving it in hot diluted HNO_3 .

$LaVO_4$ has the monoclinic monazite-type structure with space group $P2_1/n$ (Nr. 14). The Ln^{3+} ions are coordinated by nine oxygen atoms, whereas the V^{5+} ions are tetrahedrally coordinated by oxygen atoms [5]. $GdVO_4$ and $LuVO_4$ against it have the tetragonal zircon-type structure of YVO_4 , with space group $I4_1/amd$ (Nr. 141). The Ln^{3+} ions are eight-fold coordinated by oxygen forming dodecahedral cages having D_{2d} point symmetry, whereas the V^{5+} ions are tetrahedrally coordinated by oxygen atoms [6, 7, 8]. The main differences between the two matrices are related to the presence of two cations, Lu^{3+} and Gd^{3+} , having different ionic radii and electronegativities, as summarized in Table 1. Despite the similarities of the structural properties and the same site symmetry, the luminescence properties of an activator can significantly differ on passing from one member to another of the $LnVO_4$ family. The $^5D_4 \rightarrow ^7F_J$ luminescence of Tb^{3+} for instance, can be observed in $GdVO_4$ and $LuVO_4$ but shows

Experimental

no emission at all in YVO_4 [9]. The effective ionic radii, r , of these rare earth elements with coordination number 8 increases as follows: $r(\text{Gd}^{3+}) > r(\text{Y}^{3+}) > r(\text{Lu}^{3+})$ [10]. Hence, the absence of Tb^{3+} luminescence in YVO_4 can neither be explained simply by the size of Y^{3+} nor by the symmetry of the coordination polyhedra.

Table 1. r = effective ionic radius [10]; SG = space group [11, 12, 13]; PG = point group symmetry (Schoenflies); χ_P = electronegativity (Pauling scale); $\langle d(R-O) \rangle$ ($R = A, V$) = average inter-atomic distance in polyhedra of the AVO_4 structure [11, 12, 13].

| AVO_4 | $r(A)$ [pm] | $\chi_P(A)$ | SG (Nr.) | $\langle d(A-O) \rangle$ [pm] | $\langle d(V-O) \rangle$ [pm] | PG |
|-----------------|-------------|-------------|--------------------------------|-------------------------------|-------------------------------|------------------------|
| LaVO_4 | 121.6 | 1.1 | $\text{P2}_1/\text{n}$ (14) | 259.7 | 170.9 | $\text{C}_{2\text{h}}$ |
| GdVO_4 | 105.3 | 1.2 | $\text{I4}_1/\text{amd}$ (141) | 248.3 | 160.4 | $\text{D}_{2\text{d}}$ |
| YVO_4 | 101.9 | 1.22 | $\text{I4}_1/\text{amd}$ (141) | 236.5 | 170.88 | $\text{D}_{2\text{d}}$ |
| LuVO_4 | 97.7 | 1.27 | $\text{I4}_1/\text{amd}$ (141) | 233.1 | 170.67 | $\text{D}_{2\text{d}}$ |

2.2. Measurement Techniques

The energy level locations were derived from temperature dependent photoluminescence spectroscopy.

A 450W xenon lamp (FL-1039) was used in combination with a double-grating monochromator (Gemini-180, HORIBA J. Y., USA) as an excitation source. The light emitted from the crystals was detected by a single photon counting module with a channel photomultiplier (CPM, model MP-1993, PerkinElmer) after traversing a 100 mm focal length monochromator (model MCG 910, Macam Photometrics Ltd.). Excitation spectra were corrected for background and lamp spectrum (obtained with a calibrated SXUV-type Si-ultraviolet photodiode from IRD) whereas the emission spectra were corrected for the background and the transmission of the Macam monochromator in combination with the CPM. Low temperatures (down to 8 K) were achieved with a SHI-APD helium compressor (model HC-4) connected to a two-stage cryogenic refrigerator (model DE204) whereas temperature control was achieved with a temperature controller (Model 331, Lake Shore Cryotronics, Inc.).

3. Results

3.1. $LaVO_4$

The excitation spectra of $LaVO_4$ at three different temperatures are shown in Figure 1. Two excitation bands (at about 4.57 eV, 271 nm and 4.26 eV, 291 nm) with different temperature dependences can be noticed. In the same figure the absorption curve at room temperature is shown as well. Please note that the excitation spectra are displayed on a logarithmic intensity scale.

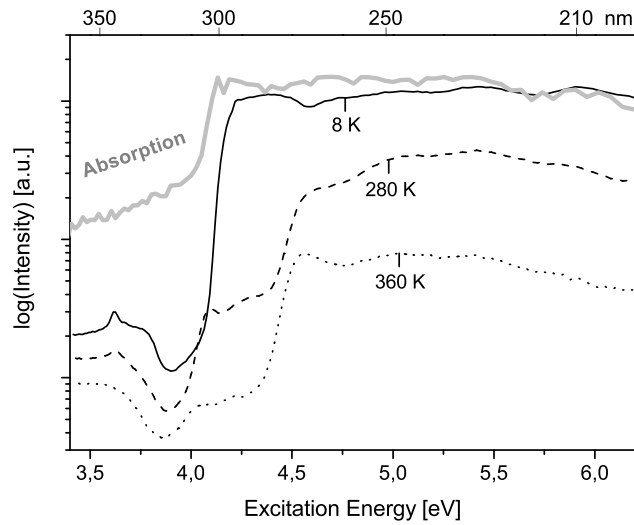


Fig. 1. Excitation and absorption spectra of $LaVO_4$ at three different temperatures monitoring the emission at 420 nm.

Fig. 2 shows two emission spectra at room temperature, one under excitation at 270 nm and the other under excitation at 290 nm; both spectra have the same shape with a broad band around 390 nm (below referred to as HE1) and differ only in their intensities

Results

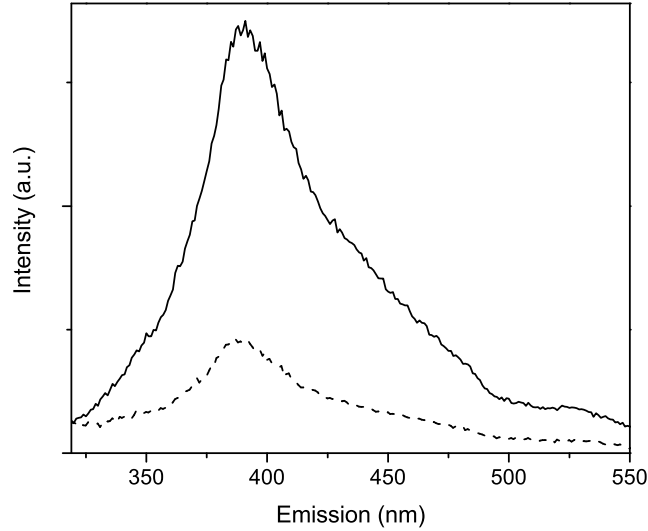


Fig. 2. Emission spectra of LaVO_4 at room temperature under 270 nm (solid line) and 290 nm (dashed line) excitation.

3.2. $\text{GdVO}_4 : 1\% \text{Ce}^{3+}$ and $\text{LuVO}_4 : 1\% \text{Ce}^{3+}$

The Ce^{3+} ion is known to be non-luminescent in vanadate lattices. Figure 3 shows the excitation spectra of $\text{GdVO}_4:\text{Ce}^{3+}$ and $\text{LuVO}_4:\text{Ce}^{3+}$ at 15 K monitoring the host emission at 447 nm. This spectrum is consistent with that reported and discussed by Ronde and Blasse for YVO_4 [14]. Accordingly, we assign the band at 4.96 eV (250 nm) to the $^1\text{A}_1 \rightarrow ^1\text{T}_2(t_1 \rightarrow e)$ (symmetry allowed) and the band at 3.87 – 4 eV (310 – 320 nm) to the $^1\text{A}_1 \rightarrow ^1\text{T}_1(t_1 \rightarrow e)$ (symmetry forbidden) absorption transition of the VO_4^{3-} ion. In Figure 4 the 15 K emission spectra of $\text{GdVO}_4:\text{Ce}^{3+}$ and $\text{LuVO}_4:\text{Ce}^{3+}$ are presented. They show the typical VO_4^{3-} group emission band with maxima at 436 nm ($\text{GdVO}_4:\text{Ce}^{3+}$) and 444 nm ($\text{LuVO}_4:\text{Ce}^{3+}$) which is assigned to the $^3\text{T}_1 \rightarrow ^1\text{A}_1$ transition [15, 16]. The weak features in the long wavelength tail of the emission band can be presumably ascribed to unwanted impurities [17].

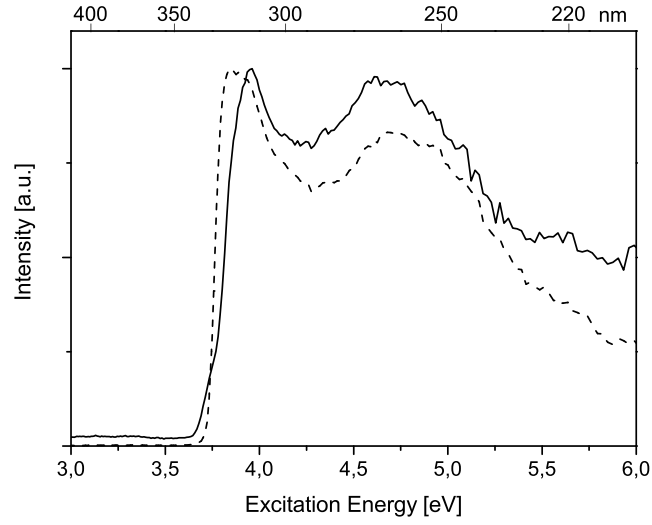


Fig. 3. Normalized excitation spectra at 15 K of GdVO₄:1%Ce³⁺ (solid line) and LuVO₄:1%Ce³⁺ (dashed line) monitoring the emission at 447 nm.

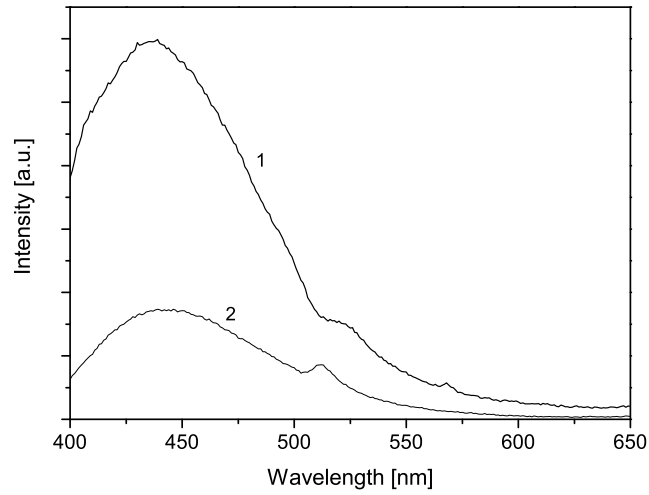


Fig. 4. Emission spectra of GdVO₄:1%Ce³⁺ (curve 1) and LuVO₄:1%Ce³⁺ (curve 2); the spectra were recorded at 15 K under 312 nm excitation.

Results

3.3. LaVO_4 : 1% Pr^{3+} , GdVO_4 : 0.6% Pr^{3+} and LuVO_4 : 0.2% Pr^{3+}

The excitation spectra of $\text{AVO}_4:\text{Pr}^{3+}$ ($A = \text{La, Gd, Lu}$) are presented in Figure 5. In the case of $\text{LaVO}_4:\text{Pr}^{3+}$ (Figure 5 (a)) the host related transition around 4.27 eV is broadened to longer wavelengths with a shoulder at about 4.13 eV (300 nm). We attribute this shoulder to the $\text{Pr}^{3+} \rightarrow \text{V}^{5+}$ IVCT. Boutinaud *et al.* identified the IVCT band in $\text{LaVO}_4:\text{Pr}^{3+}$ powders at about 3.57 eV (347 nm) but it should be noticed that the band appeared as a weak shoulder in a low resolved excitation spectrum recorded at room temperature and its position was not accurate. A better accuracy is provided by the spectra shown in Figure 5 (a) which were recorded on single crystals. A shift of the band is clearly evidenced while moving from room temperature (around 3.87 eV, 320 nm) to 8 K (around 4.13 eV, 300 nm). The optical properties of Pr^{3+} in gadolinium and lutetium orthovanadates have been investigated at room temperature in a previous study [2]. The 15 K and 200 K excitation spectra of $\text{GdVO}_4:\text{Pr}^{3+}$ and $\text{LuVO}_4:\text{Pr}^{3+}$ monitoring the ${}^3\text{P}_0 \rightarrow {}^3\text{H}_6$ (625 nm) emission are shown in Figure 5 (b) and (c), respectively. In $\text{GdVO}_4:\text{Pr}^{3+}$ three UV bands can be noticed: At 4.96 eV (250 nm), 3.87 – 4 eV (310 – 320 nm) and 3.2 eV (383 nm). The two former are due to transitions within the VO_4^{3-} complex as found in $\text{AVO}_4:\text{Ce}^{3+}$ ($A = \text{Gd, Lu}$). The latter band at 3.2 eV is ascribed to the IVCT although it differs somewhat from the previously reported value at about 3.4 eV [2]. At lower energies the ${}^3\text{H}_4 \rightarrow {}^3\text{I}_6, {}^3\text{P}_j$ excitation group (2.5 – 2.8 eV, 439 – 497 nm) can be seen. $\text{LuVO}_4:\text{Pr}^{3+}$ (Figure 5 (c)) shows beside the VO_4^{3-} group and ${}^3\text{H}_4 \rightarrow {}^3\text{P}_j$ multiplet transitions a broad band between 2.8 – 3.4 eV (360 – 440 nm) which is composed of at least two different bands with different temperature behavior.

Boutinaud *et al.* have identified the IVCT in $\text{LuVO}_4:\text{Pr}^{3+}$ at about 3.1 eV (396 nm). This is in agreement with the low excitation band at 200 K. At 15 K though the IVCT band is overlapped by a broad band (hereafter referred to as U transition) peaking at 2.97 eV (418 nm).

The emission spectra of $\text{LaVO}_4:\text{Pr}^{3+}$ are shown in Figure 6 (a). They show under 460 nm excitation (Figure 6 (a)) mainly ${}^3\text{P}_0 \rightarrow {}^3\text{H}_4$ (494 – 512 nm), ${}^3\text{H}_6, {}^3\text{F}_2$ (614 – 642 nm), ${}^3\text{P}_0 \rightarrow {}^3\text{F}_3$ (653 – 664 nm) emission. The structure between 596 – 607 nm is ascribed to the ${}^1\text{D}_2 \rightarrow {}^3\text{H}_4$ transition. The inset in Figure 6 (a) shows the temperature quenching behavior of the 502 nm peak.

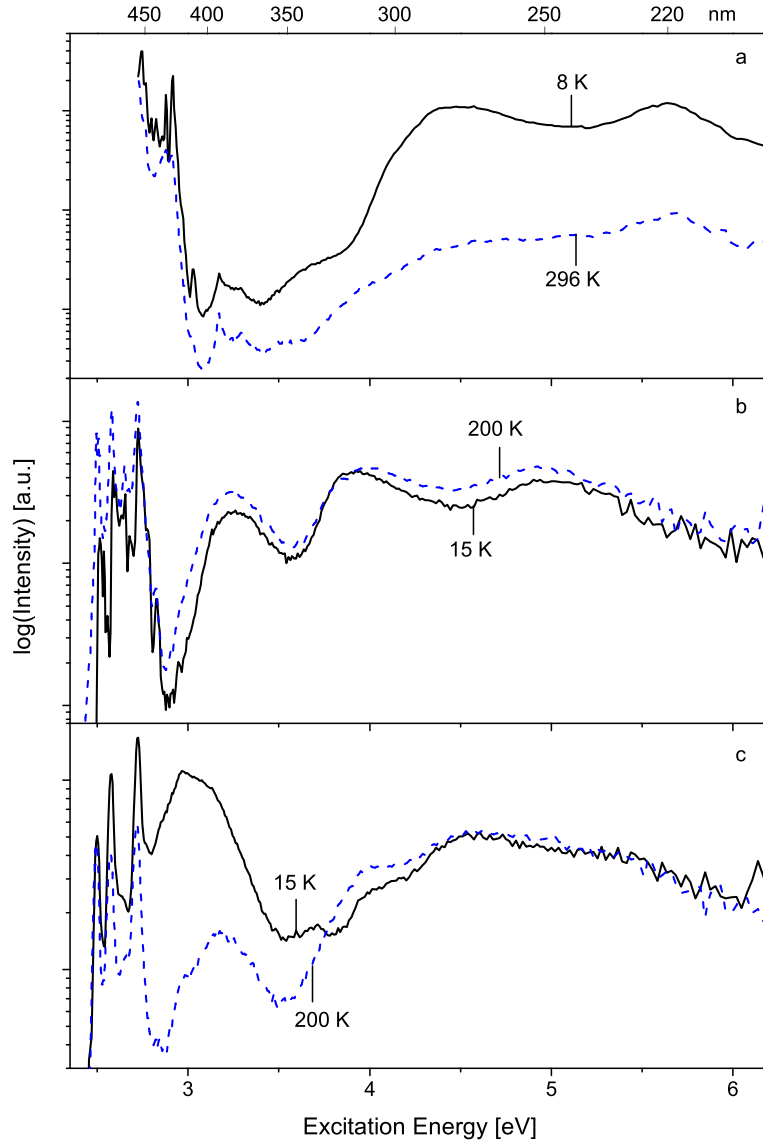


Fig. 5. Excitation spectra of $LaVO_4:1\%Pr^{3+}$ (a), $GdVO_4:0.6\%Pr^{3+}$ (b) and $LuVO_4:0.2\%Pr^{3+}$ (c); in the spectra of $LaVO_4$ the 497 nm emission was monitored, in the spectra of $GdVO_4$ and $LuVO_4$ the 625 nm emission was monitored.

Results

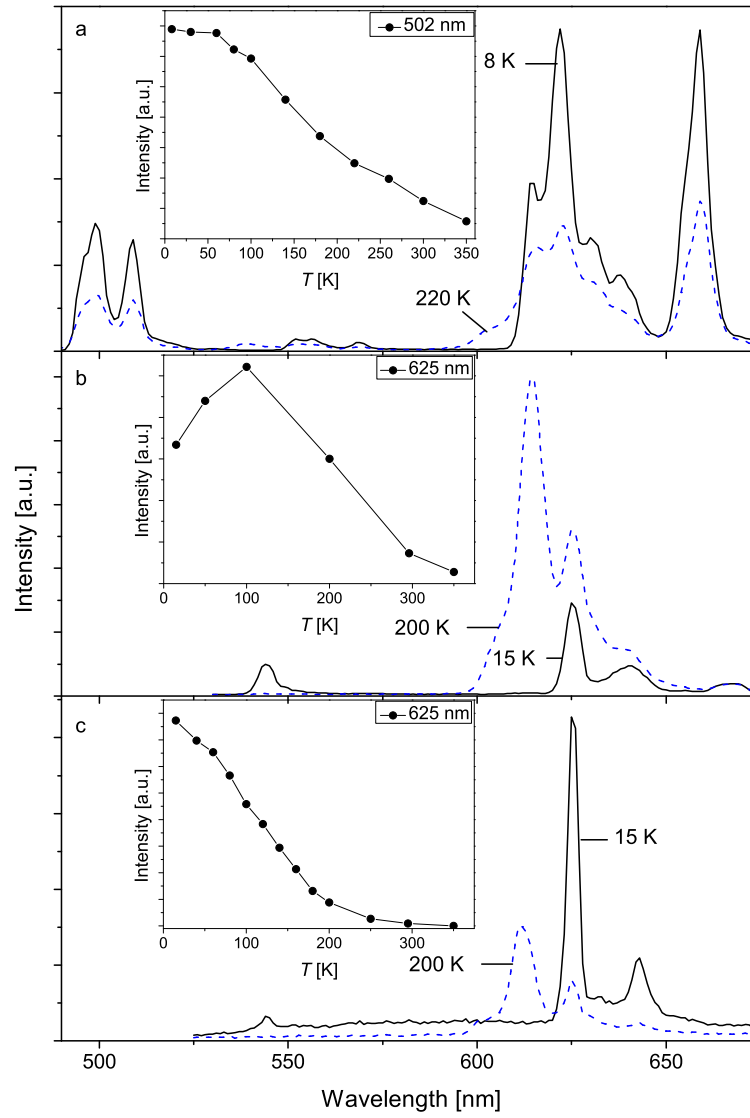


Fig. 6. Emission spectra of LaVO₄:1%Pr³⁺, Exc = 460 nm (a), GdVO₄:0.6%Pr³⁺, Exc = 480 nm (b) and LuVO₄:0.2%Pr³⁺, Exc = 483 nm (c).

Chapter 2. Lanthanide 4f Level Location in $AVO_4:Ln^{3+}$

Figures 6 (b) and (c) show the emission spectra of $GdVO_4:Pr^{3+}$ and $LuVO_4:Pr^{3+}$ under ${}^3H_4 \rightarrow {}^3P_1$ (480 nm) excitation at 15 K and at 200 K. The four prominent groups of emission are due to ${}^3P_0 \rightarrow {}^3H_5$ (544 nm), ${}^3P_0 \rightarrow {}^3H_6$ (625 – 644 nm), and ${}^3P_0 \rightarrow {}^3F_2$ (667 nm) transitions, similar to the ones identified in $YNbO_4:Pr^{3+}$ [18, 19]. In the 200 K spectra an additional red band is present, assigned to the ${}^1D_2 \rightarrow {}^3H_4$ (615 nm) transition. In the adopted experimental conditions in fact, the 1D_2 level can be populated by multi-phonon relaxation from the 3P_0 level or by radiationless relaxation through the IVCT state, thermally populated from 3P_0 . At 15 K, both processes are inefficient and the emission arises from the 3P_0 level only. As the temperature increases, the 1D_2 population progressively increases as well as the intensity of the corresponding red emission. It has to be noted that the low temperature spectrum of Pr^{3+} in $LuVO_4$ overlaps a weak broadband with maximum at around 600 nm, likely associated to the weak U excitation band. The insets of Figures 6 (b) and (c) show the temperature quenching behavior of the ${}^3P_0 \rightarrow {}^3H_6$ (625 nm) emission under ${}^3H_4 \rightarrow {}^3P_1$ (483 nm) excitation.

3.4. $LaVO_4:1\%Eu^{3+}$, $GdVO_4:1\%Eu^{3+}$ and $LuVO_4:1\%Eu^{3+}$

The temperature dependent excitation spectrum of $LaVO_4:Eu^{3+}$ which is presented in Figure 7 shows beside the typical ${}^7F_0 \rightarrow {}^5L_6$, 6D_2 transitions within the $4f^6$ configuration of Eu^{3+} the host related absorption band around 4.2 eV with a shoulder at about 3.9 eV (315 nm). We assign this shoulder to the $O^{2-} \rightarrow Eu^{3+}$ CT. Additionally a clear structure of unknown origin around 3.4 eV (360 nm) can be seen. Figures 7 (b) and (c) show the excitation spectra of $GdVO_4:Eu^{3+}$ and $LuVO_4:Eu^{3+}$ monitoring the ${}^5D_0 \rightarrow {}^7F_2$ (622 nm) emission at two different temperatures. Beside the ${}^7F_0 \rightarrow {}^5D_j$ multiplet transitions of Eu^{3+} the two VO_4^{3-} group-related bands at 4.96 eV and at about 3.87 eV can be seen. In the low temperature spectrum of $LuVO_4:Eu^{3+}$ the U excitation band appears at around 3.15 eV (394 nm). In both compounds the luminescence intensity increases with increasing temperature (see inset of Fig. 7 a). The temperature behavior of the intensity of the main excitation band around 3.87 eV is consistent with the character of the involved ${}^1A_1 \rightarrow {}^1T_1$ transition: forbidden in T_d symmetry, it takes allowance from the static and dynamic (then thermally activated) distortions from the perfect tetrahedral geometry trough the mixing of the low symmetry components of the 1T_1 and 1T_2 states [14].

The 15 K emission spectrum of $LaVO_4:Eu^{3+}$ is shown in Figure 8 (a). It features ${}^5D_0 \rightarrow {}^7F_1$ (582 – 601 nm), 7F_2 (613 – 633 nm), 7F_3 (647 – 660 nm), 7F_4 (687 – 713 nm) transitions [20].

Results

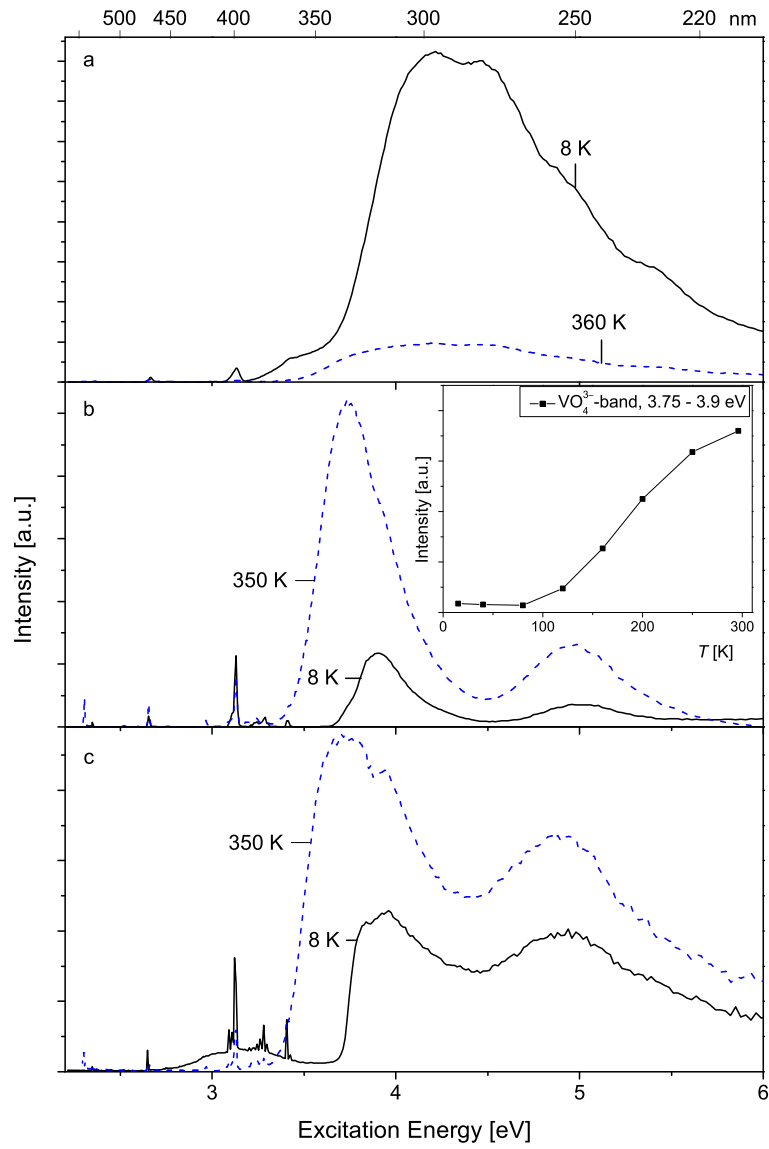


Fig. 7. Excitation spectra of LaVO₄:1%Eu³⁺, Em = 590 nm (a), GdVO₄:1%Eu³⁺, Em = 622 nm (b) and LuVO₄:1%Eu³⁺, Em = 622 nm (c).

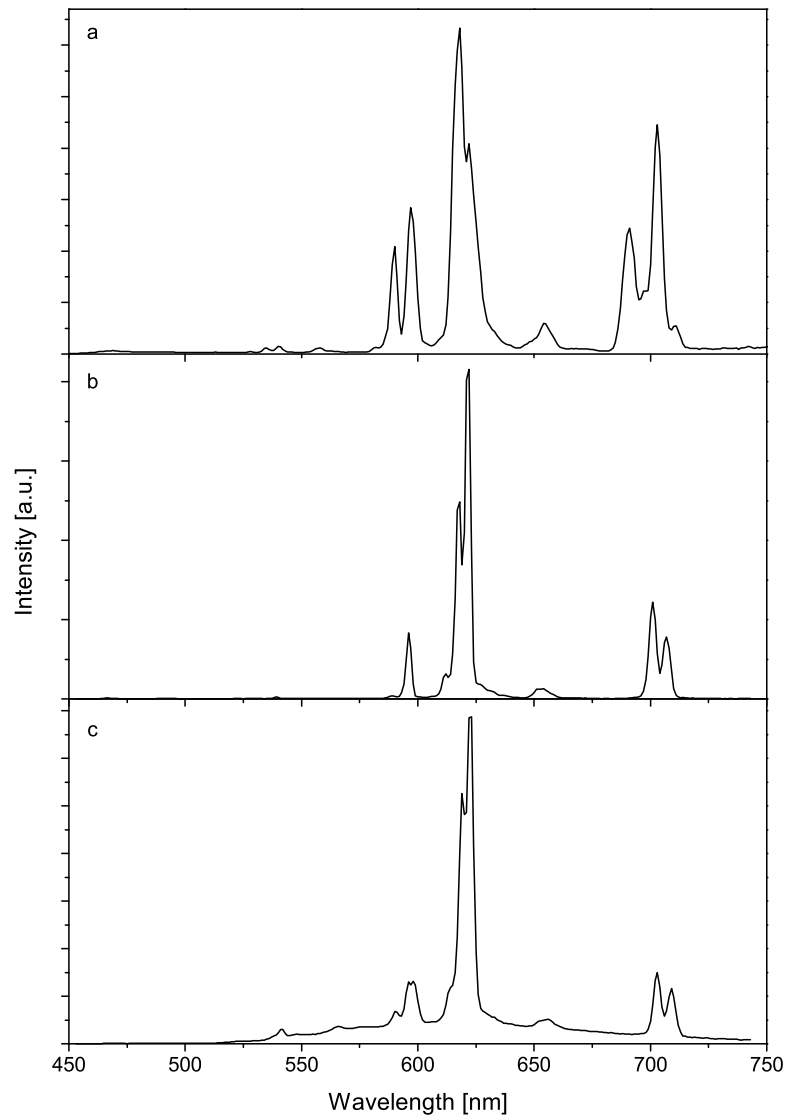


Fig. 8. 15 K emission spectra of $LaVO_4:1\%Eu^{3+}$, Exc = 395 nm (a), $GdVO_4:1\%Eu^{3+}$, Exc = 395 nm (b) and $LuVO_4:1\%Eu^{3+}$, Exc = 395 nm (c).

Results

In Figures 8 (b) and (c) the emission spectra of $\text{GdVO}_4:\text{Eu}^{3+}$ and $\text{LuVO}_4:\text{Eu}^{3+}$ are presented showing the same ${}^5\text{D}_0 \rightarrow {}^7\text{F}_j$ multiplet emission peaks of Eu^{3+} as in $\text{LaVO}_4:\text{Eu}^{3+}$. In addition, the spectra of all three orthovanadates present some barely observable features below 578 nm that can be ascribed to transitions from the ${}^5\text{D}_1$ level [21]. These are more intense in the spectra of $\text{LaVO}_4:\text{Eu}^{3+}$ and $\text{LuVO}_4:\text{Eu}^{3+}$; in the latter case they overlap a broad band between about 500 nm and 700 nm which could relate to the low energy U excitation band at about 394 nm.

3.5. $\text{LaVO}_4: 1\% \text{Tb}^{3+}$, $\text{GdVO}_4: 1\% \text{Tb}^{3+}$ and $\text{LuVO}_4: 1\% \text{Tb}^{3+}$

Looking at the low temperature (8 K) excitation spectrum of $\text{LaVO}_4:\text{Tb}^{3+}$, presented in Figure 9 (a), two peculiar features can be noticed: a first narrow band around 3.27 eV (379 nm) and a second broader one at about 3.8 eV (325 nm). The narrow 3.27 eV band is attributed in spite of its broadening to the ${}^7\text{F}_6 \rightarrow {}^5\text{D}_3$ transition. This assignment will be founded in the Discussion Section. The second band at about 3.8 eV is assigned to the $\text{Tb}^{3+} \rightarrow \text{V}^{5+}$ IVCT. In Figures 9 (b) and (c) the 15 K excitation spectra of $\text{GdVO}_4:\text{Tb}^{3+}$ and $\text{LuVO}_4:\text{Tb}^{3+}$ are shown, monitoring the ${}^5\text{D}_4 \rightarrow {}^7\text{F}_5$ (548 nm) emission. They present the 4.96 eV and 3.87 eV bands of the VO_4^{3-} group, whereas the 3.3 eV (376 nm) band in $\text{GdVO}_4:\text{Tb}^{3+}$ is assigned to the IVCT band of Tb^{3+} . The inset in Fig. 9 shows the temperature quenching behavior of this band.

Fig. 10 presents the 15 K emission spectra of $\text{AVO}_4:\text{Tb}^{3+}$ ($A = \text{La, Gd, Lu}$) during 370 nm excitation. The spectra show only ${}^5\text{D}_4 \rightarrow {}^7\text{F}_j$ multiplet emission lines. No emission from the $\text{Tb}^{3+} : {}^5\text{D}_3$ level can be seen. The inset in each panel of Figure 10 shows the temperature quenching behavior of the ${}^5\text{D}_4 \rightarrow {}^7\text{F}_5$ (547 nm) emission under ${}^7\text{F}_6 \rightarrow {}^5\text{D}_4$ (468 nm) excitation.

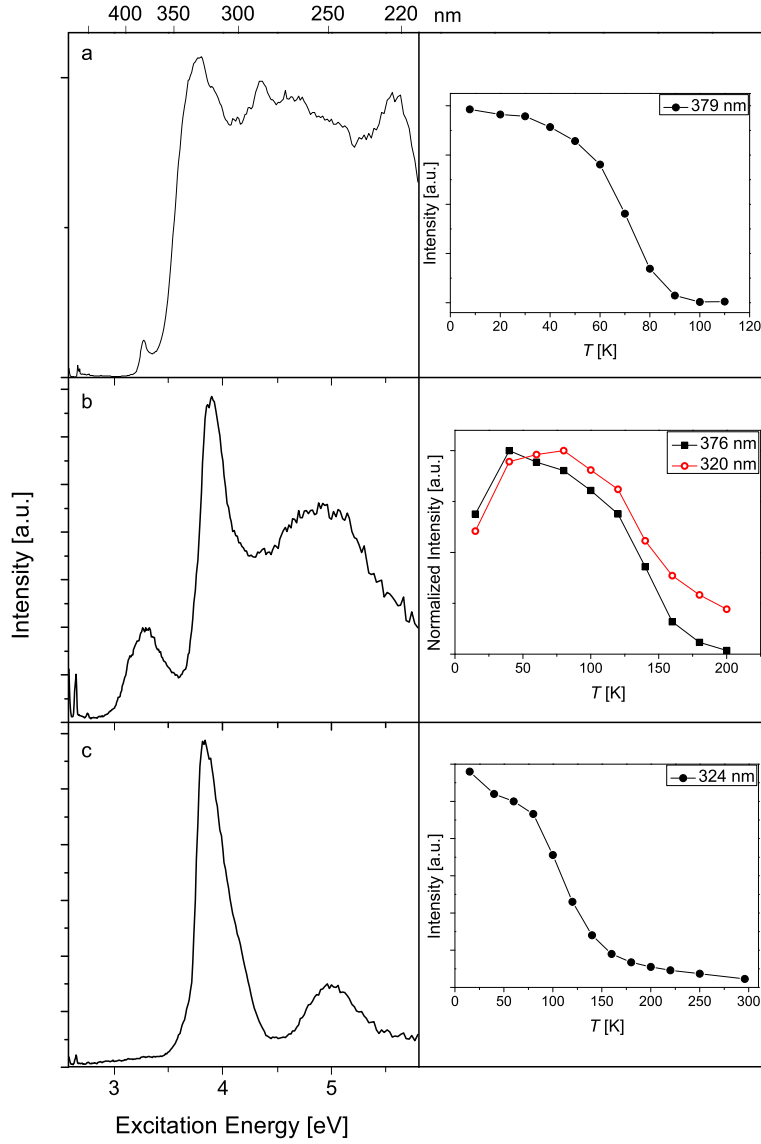


Fig. 9. Excitation spectra of $LaVO_4:1\%Tb^{3+}$ at 8 K, $Em = 548$ nm (a), $GdVO_4:1\%Tb^{3+}$ at 15 K, $Em = 548$ nm (b) and $LuVO_4:1\%Tb^{3+}$ at 15 K, $Em = 548$ nm (c).

Results

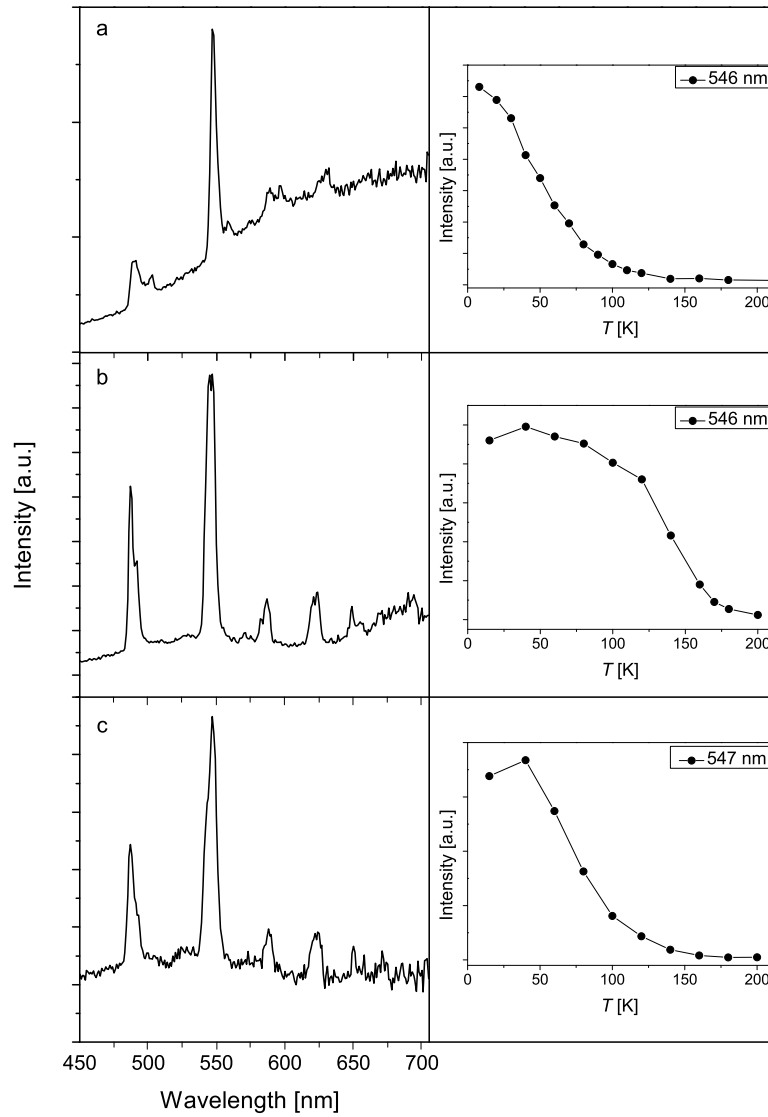


Fig. 10. 15 K emission spectra of LaVO₄:1%Tb³⁺, Exc = 370 nm (a), GdVO₄:1%Tb³⁺, Exc = 370 nm (b) and LuVO₄:1%Tb³⁺, Exc = 370 nm (c); Inset shows the temperature behavior of the peak intensity at about 547 nm under 468 nm excitation.

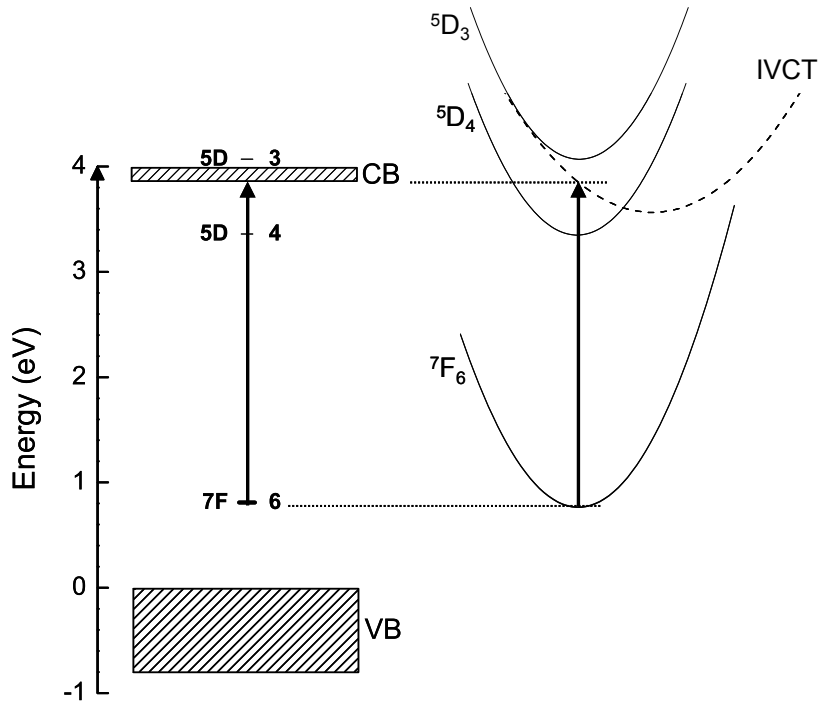


Fig. 11. Energy level diagram (left side) and configurational coordinate diagram (right side) of $GdVO_4:Tb^{3+}$; arrows indicate the IVCT transition as used for energy level location.

4. Discussion and Conclusion

The 4.26 eV band in $LaVO_4$ is taken as the first allowed VO_4^{3-} transition which defines the band gap energy. In both $GdVO_4$ and $LuVO_4$ this energy is lower, viz. 3.87 eV. For the sake of convenience the band gap energy will be regarded in the following as the energy between the top of the VB and the bottom of the CB. Figure 11 illustrates the $Ln^{3+} \rightarrow V^{5+}$ IVCT transition both within the energy level diagram and the configurational coordinate diagram for $GdVO_4:Tb^{3+}$. According to this depiction the bottom of the CB as defined by us is somewhat higher in energy than the IVCT state relaxed to the equilibrium configuration in the configurational coordinate diagram (see Figure 11).

Discussion and Conclusion

4.1. Ln^{2+} 4f GS Energy Location

The location of the Ln^{2+} GS energies is usually found by the help of the Eu^{3+} CT band. This band is due to the transfer of an electron from an oxygen ligand to Eu^{3+} thus forming Eu^{2+} in its ground state $4f^7$ level. In oxide compounds it is usually observed as a distinct broad excitation band with, depending on the type of compound, a maximum that may vary between 240 nm and 300 nm. From the energy $E^{CT}(\text{Eu}^{3+})$ of the Eu^{3+} CT band the CT energies of all other ions doped in the same compound can be derived via:

$$E^{CT}(\text{Ln}^{3+}) \cong E^{CT}(\text{Eu}^{3+}) + \Delta E^{CT}(\text{Ln}^{3+}) \quad (1)$$

The host independent constants $\Delta E^{CT}(\text{Ln}^{3+})$ are compiled in [3]. The Ln^{3+} CT energy gives information on the location of the 4f GS of the divalent ion relative to the top of the VB. In our measurements though we could not identify an $\text{O}^{2-}-\text{Eu}^{3+}$ CT in $\text{GdVO}_4:\text{Eu}^{3+}$ and $\text{LuVO}_4:\text{Eu}^{3+}$. As mentioned earlier, in all excitation spectra presented in this work, a band at around 250 nm can be seen which has the same temperature behavior as the band at about 320 nm. Therefore we assigned the 250 nm band to a higher VO_4^{3-} group transition and not to the Eu^{3+} CT as done by Liu *et al.* [22]. In any case we have to assume that the 4f GS of Eu^{2+} is energetically located above the bottom of the CB for both types of compounds.

4.2. Ln^{3+} 4f GS Energy Location

The method to locate the divalent lanthanide ground state energies is based on CT energy to the trivalent lanthanides. An analogous method is not applicable to locate the trivalent ground state energies because the Ln^{4+} valence is usually not stable in compounds. Another method was proposed by Dorenbos. The energy differences between the lowest 4f and lowest 5d states of both the divalent and the trivalent lanthanides are well known. Therefore once the 4f ground state locations are known those for the lowest 5d states can also be located. It turns out that the absolute location of the lowest 5d state of divalent lanthanide ions relative to the host bands gradually change when moving through the lanthanide series, but they never deviate more than 0.5 eV from each other. By assuming a similar constant energy for the lowest 5d states for the trivalent lanthanides, and by utilizing the known variation in 4f-5d energy differences with changing type of trivalent lanthanide ion, the 4f ground state energies of the trivalent lanthanides relative to the valence band can be found. An equation similar as Eq. (1) but with parameter values for the trivalent lanthanides was proposed. The proposed parameter values in Ref. [3] suggest that the Tb^{3+} ground state should be found 0.73 eV above the Pr^{3+} ground state. This would also imply that the IVCT band

from Tb^{3+} to the CB should be at 0.73 eV lower energy than that for Pr^{3+} . Recently, Boutinaud *et al.* found in $LaVO_4$, $YNbO_4$ and $CaNb_2O_6$ about the same energy for the Pr^{3+} and the Tb^{3+} IVCT transitions [19]. The 0.06 eV difference between the maxima of the IVCT bands in $GdVO_4:Pr^{3+}$ and $GdVO_4:Tb^{3+}$ observed in this work confirms the findings of Boutinaud *et al.* Beside the IVCT energy, supporting evidence can be derived from the luminescence quenching of the $Pr^{3+}:^3P_0$ and $Tb^{3+}:^5D_4$ emission in order to place the 4f energy levels of Pr^{3+} and Tb^{3+} relative to the bottom of the CB. In the case of $GdVO_4:Tb^{3+}$ an excitation at 370 nm shows $^5D_4 \rightarrow ^7F_J$ multiplet emission but no emission from 5D_3 which is rather uncommon for Tb-doped compounds. This indicates that the $Tb^{3+}:^5D_3$ energy level is located energetically above the IVCT state in the configurational coordinate diagram which thus provides a non-radiative relaxation route for the 5D_3 electron (see Figure 9). In $LuVO_4:Tb^{3+}$ the same excitation also gave rise only to $^5D_4 \rightarrow ^7F_J$ multiplet emission of Tb^{3+} . This shows that also in $LuVO_4:Tb^{3+}$ the 5D_3 level must energetically be located above the IVCT state or the bottom of the CB. In order to derive the activation-energies for the temperature quenching of the luminescence we assumed a simple model depicted in Figure 12 using the example of Tb^{3+} .

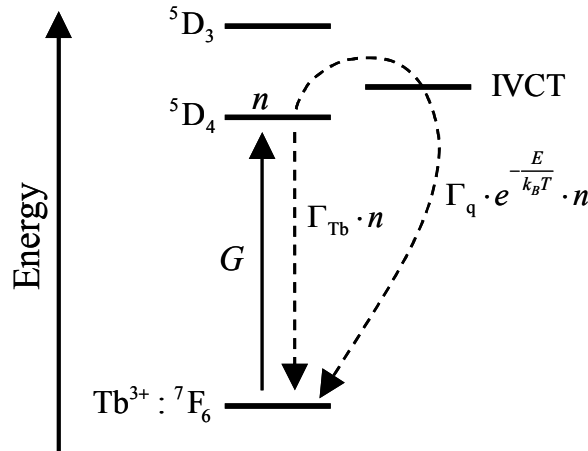


Fig. 12. Energy level scheme illustrating the temperature quenching of $Tb^{3+}:^5D_4$ luminescence. The steady state condition for this first order reaction is fulfilled when $dn/dt = G - (\Gamma_{Tb} + \Gamma_q \cdot \exp(-E/k_B T)) \cdot n = 0$.

Within that model the temperature-dependent emission intensity is proportional to the steady state population, n , of the 5D_4 level:

Discussion and Conclusion

$$I(T) \propto \Gamma_{\text{Ln}} \cdot n(T) = \frac{G}{1 + (\Gamma_0/\Gamma_{\text{Ln}})\exp(-E/k_B T)} \quad (2)$$

G is the excitation rate to ${}^5\text{D}_4$, $\Gamma_0 \cdot \exp(-E/k_B T)$ is the rate constant for temperature-dependent and radiationless relaxation via the IVCT state, Γ_{Ln} is the rate constant for radiative transitions from the Ln^{3+} emitting level, and k_B the Boltzmann constant. From equation (2) it follows that $I(T \rightarrow 0) \equiv I_0 \propto G$ is the luminescence intensity at low temperatures. The fitting parameters $\Gamma_0/\Gamma_{\text{Ln}}$ and E for temperature quenching behavior of the $\text{Pr}^{3+}:{}^3\text{P}_0$ and $\text{Tb}^{3+}:{}^5\text{D}_4$ emission in AVO_4 ($A = \text{La, Gd, Lu}$) are shown in Table 2. From Table 2 we see that the activation-energy for temperature quenching of the $\text{Pr}^{3+}:{}^3\text{P}_0$ emission is about the same in $\text{LaVO}_4:\text{Pr}^{3+}$ and $\text{LuVO}_4:\text{Pr}^{3+}$ and very close to the activation energies of the $\text{Tb}^{3+}:{}^5\text{D}_4$ emission in both compounds. Apparently, the ${}^3\text{P}_0$ and ${}^5\text{D}_4$ levels are at the same position in the band gap. As the $\text{Pr}^{3+}:{}^3\text{H}_4 - {}^3\text{P}_0$ and the $\text{Tb}^{3+}:{}^7\text{F}_6 - {}^5\text{D}_4$ energy differences just happen to be almost equally large, also the Pr^{3+} and Tb^{3+} ground states should be at the same position in the band gap. This is in agreement with the similarity of the Pr^{3+} and Tb^{3+} IVCT energies which has been identified by us in the excitation spectra. In the case of GdVO_4 the activation energies for temperature quenching of the Pr^{3+} and the Tb^{3+} emission are more than twice as large and also the PL intensities of $\text{LuVO}_4:\text{Ln}^{3+}$ are about 2 times weaker compared to the ones of $\text{GdVO}_4:\text{Ln}^{3+}$ ($\text{Ln} = \text{Pr, Tb}$; see Figures 6 and 10). All spectra were recorded under similar conditions. This suggests that the $\text{Pr}^{3+}:{}^3\text{P}_0$ as well as the $\text{Tb}^{3+}:{}^5\text{D}_4$ energy level is energetically located even closer to the CB in LaVO_4 and LuVO_4 than in GdVO_4 .

Table 2. Rounded thermal quenching parameters $\Gamma_0/\Gamma_{\text{Ln}}$ and E for emission spectra of $\text{GdVO}_4:\text{Tb}^{3+}$ and $\text{LuVO}_4:\text{Tb}^{3+}$. The emission spectra were recorded under $\text{Tb}^{3+}:{}^7\text{F}_6 \rightarrow {}^5\text{D}_4$ and $\text{Pr}^{3+}:{}^3\text{H}_4 \rightarrow {}^3\text{P}_1$ excitation, respectively.

| Sample | Emission band | $\Gamma_0/\Gamma_{\text{Ln}}$ [$\times 10^3$] | E [meV] |
|--------------------------------|--|--|--------------|
| $\text{LaVO}_4:\text{Pr}^{3+}$ | ${}^3\text{P}_0 \rightarrow {}^3\text{F}_2$ (659 nm) | 8 | 41 |
| $\text{LaVO}_4:\text{Tb}^{3+}$ | ${}^5\text{D}_4 \rightarrow {}^7\text{F}_5$ (546 nm) | 57 | 19 |
| $\text{GdVO}_4:\text{Pr}^{3+}$ | ${}^3\text{P}_0 \rightarrow {}^3\text{H}_6$ (625 nm) | 0.7 | 121 |
| $\text{GdVO}_4:\text{Tb}^{3+}$ | ${}^5\text{D}_4 \rightarrow {}^7\text{F}_5$ (546 nm) | 17 | 114 |
| $\text{LuVO}_4:\text{Pr}^{3+}$ | ${}^3\text{P}_0 \rightarrow {}^3\text{H}_6$ (625 nm) | 0.06 | 43 |
| $\text{LuVO}_4:\text{Tb}^{3+}$ | ${}^5\text{D}_4 \rightarrow {}^7\text{F}_5$ (547 nm) | 0.3 | 37 |

The fact that the Γ_0/Γ_{Ln} ratio of Tb^{3+} is always larger than the one of Pr^{3+} we attribute to the fact that the life time of Tb^{3+} is much longer than the life time of Pr^{3+} [23]. It can be seen, that the $Tb^{3+}:^5D_4$ and the $Pr^{3+}:^3P_0$ levels, when placed by means of the activation-energies given in Table 2, are about 0.5 eV closer to the bottom of the CB than when placed with the help of the IVCT energies. This difference can be understood in view of Figure 11. We have chosen to use the IVCT transition energies as a basis in order to place the Pr^{3+} and Tb^{3+} levels energetically in the energy gap. On this ground we can now predict the relative location of the 4f GS energies of all the other possible Ln^{3+} dopants in these orthovanadates by using the empirical model of Dorenbos. To account for the similar IVCT energies of Pr^{3+} and Tb^{3+} we have tilted the zig-zag curve of the trivalent Ln ions presented in earlier publications linearly with the difference of the ionic radii of Ln^{3+} and Ce^{3+} [24, 25]. The complete energy level diagrams are shown in Figure 13.

Based on excitation spectra, we concluded that the lowest VO_4^{3-} transition is about 0.5 eV higher in energy in $LaVO_4$ than in $GdVO_4$ and $LuVO_4$. Even though $LaVO_4$ (space group $P2_1/n$, [11]) has a different crystal structure than $GdVO_4$ and $LuVO_4$ (space group $I4_1/amd$, [12, 13]), in all cases the vanadium ions are coordinated by 4 oxygen atoms with similar interatomic distances between V^{5+} and O^{2-} [6, 7, 11]. Blasse and Brill [15] reported about the dependence of the maximum of the vanadate emission band on the choice of A in compounds with formula AVO_4 : The smaller the effective ionic radius of A with a certain coordination number is, the more the maximum of the vanadate emission band is shifted to longer wavelengths. This can also be seen in the emission spectra of $GdVO_4:Ce^{3+}$ and $LuVO_4:Ce^{3+}$ (see section 3.1.). None of the PL spectra shows 5d-4f emission or 4f-5d excitation. This indicates that in the three energy level diagrams presented in Figure 13 the 5d states of the Ln dopant ions are located inside the CB. The diagrams of $GdVO_4$ and $LuVO_4$ also explain why no $Tb^{3+}:^5D_3$ emission could be observed in these orthovanadates as this state is energetically located inside the CB. The ground state energies of the divalent ions are all energetically located inside the CB as well, except for $LaVO_4:Eu^{3+}$, from which follows that the orthovanadates, AVO_4 , can not contain Ln dopant ions with oxidation state (II). For the same reason these Ln dopant ions can not even serve as meta-stable electron-traps. On the other hand the ground state energies of Ce^{3+} , Pr^{3+} and Tb^{3+} are energetically located above the VB and could therefore serve as stable hole-traps.

Discussion and Conclusion

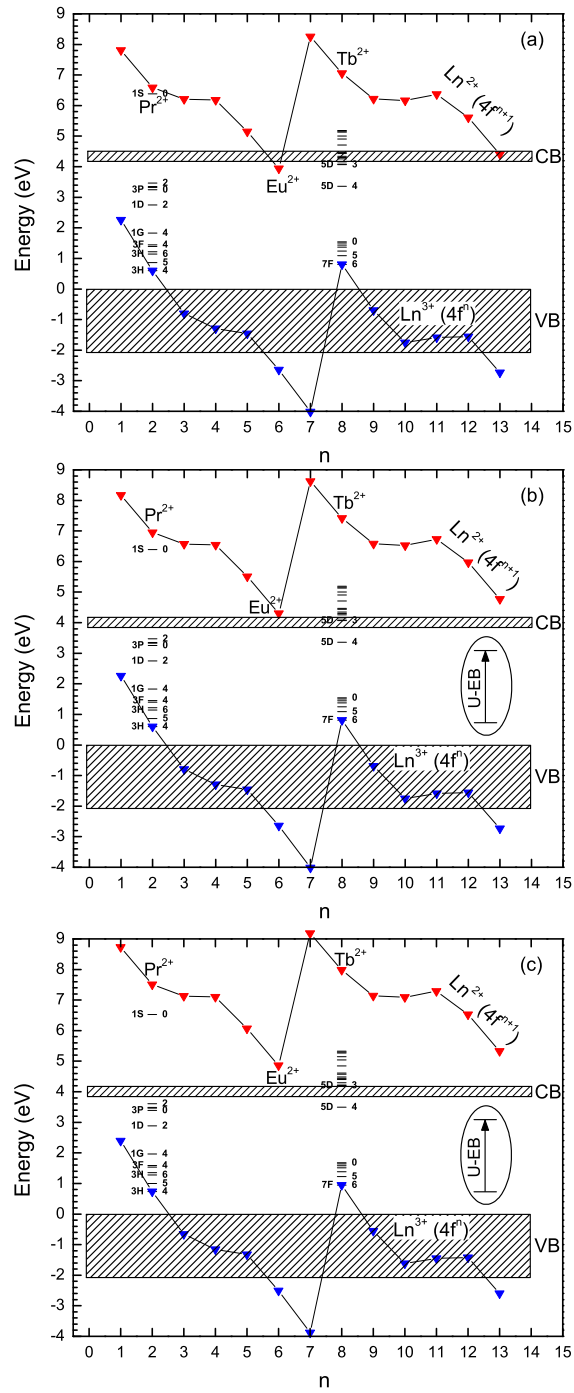


Fig. 13. Energy level diagrams of $\text{LaVO}_4:\text{Ln}^{3+}$ (a), $\text{GdVO}_4:\text{Ln}^{3+}$ (b) and $\text{LuVO}_4:\text{Ln}^{3+}$ (c); for Pr^{2+} and Tb^{2+} also the 4f energy levels are displayed; n = number of electrons in 4f shell of Ln^{3+} ; U-EB = U excitation band as specified in text (it does not hold for all $\text{GdVO}_4:\text{Ln}^{3+}$ and $\text{LuVO}_4:\text{Ln}^{3+}$ materials).

Acknowledgements

This work was supported by the Dutch Technology Foundation (STW).

References

References

- [1] Krumpel A.H., van der Kolk E., Dorenbos P., Boutinaud P., Cavalli E., Bettinelli M., *Mater. Sc. Eng. B*, **146** (2008) 114
- [2] Boutinaud P., Mahiou R., Cavalli E., Bettinelli M., *Chem. Phys. Lett.*, **418** (2005) 181
- [3] Dorenbos P., *J. Phys.: Condens. Matter*, **15** (2003) 8417
- [4] Smith S.H., Wanklyn B.M., *J. Cryst. Growth*, **21** (1974) 23
- [5] Rice C.E., Robinson W.R., *Acta Cryst.*, **B 32** (1976) 2232
- [6] Mahapatra S., Rahmanan A., *Journal of Alloys Compd.*, **395** (2005) 149
- [7] Chakoumakos B.C., Abraham M.M., Boatner L.A., *J. Solid State Chem.*, **109** (1994) 197
- [8] Wang X. Loa I., Syassen K., Hanfland M., Ferrand B., *Phys. Rev. B*, **70** (2004) 064109
- [9] Blasse G., Bril A., *Philips Res. Rep.*, **22** (1967) 481
- [10] Shannon R.D., *Acta Cryst.*, **A 32** (1976) 751
- [11] Rice C.E., Robinson W.R., *Acta Cryst.*, **B 32** (1976) 2232
- [12] Mahapatra S., Ramanan A., *J. Alloys Compd.*, **395** (2005) 149
- [13] Chakoumakos B.C., Abraham M.M., Boatner L.A., *J. Solid State Chem.*, **109** (1994) 197
- [14] Ronde H., Blasse G., *J. Inorg. Nucl. Chem.*, **40** (1978) 215
- [15] Blasse G., Bril A., *J. chem Phys.*, **50** (1969) 2974
- [16] Boulon G., *J. Phys. (Paris)*, **32** (1971) 333
- [17] W. Ryba-Romanowski, S. Gołab, P. Solarz, G. Dominiak-Dzik, P. Lukasiewicz, *Appl. Phys. Lett.*, **80** (2002) 1183
- [18] Schipper W.J., Hoogendorp M.F., Blasse G., *J. Alloys Compd.*, **202** (1993) 283
- [19] Boutinaud P., Cavalli E., Bettinelli M., *J. Phys. : Condens. Matter*, **19** (2007) 386230
- [20] Liu B., Shi C., Zhang Q., Chen Y., *J. Alloys Compd.*, **333** (2002) 215
- [21] Brecher C., Samelson H., Lempicki A., Riley R., Peters T., *Phys. Rev.*, **155** (1967) 178
- [22] Liu B., Shi C., Zhang Q., Chen Y., *J. Alloys Compd.*, **333** (2002) 215
- [23] Yen W.M., Shionoya S., Yamamoto H. (editors), *Phosphor Handbook*, 2nd ed. (2007) ISBN 0-8493-3564-7
- [24] Thiel C.W., Gruguel H., Wu H., Sun Y., Lapeyre G.J., Cone R.L., Equall R.W., Macfarlane R.M., *Phys. Rev. B*, **64** (2001) 085107

Chapter 2. Lanthanide 4f Level Location in $AVO_4:Ln^{3+}$

[25] Thiel C.W., Gruguel H., Sun Y., Lapeyre G.J., Macfarlane R.M., Equall R.W., Cone R.L.,
J. Lumin., **94** (2001)

Chapter 3

Lanthanide 4f-level Location in Lanthanide Doped and Cerium-Lanthanide Co-Doped NaLaF₄ by Photo- and Thermoluminescence

Abstract

Photo- and thermoluminescence spectra of NaLaF₄:Ln³⁺ (Ln = Ce, Pr, Nd, Sm, Eu, Gd, Tb, Dy, Ho, Er, Tm) and NaLaF₄:Ce³⁺, Ln³⁺ (Ln = Nd, Sm, Ho, Er, Tm) are presented and used together with the empirical Dorenbos model in order to establish the 4f energy level positions of all tri- and divalent lanthanide ions doped in NaLaF₄. The information will be presented in form of an energy level diagram. It is shown that in addition to this diagram only two assumptions, viz. the presence of two host related electron traps and the presence of V_k-centers, are necessary for explaining the lanthanide-specific TL glow curves of both Ln mono- and Ce-Ln co-doped NaLaF₄.

1. Introduction

Luminescence properties of lanthanide (Ln) doped phosphors depend strongly on the position of the excited 5d and the 4f levels, both relative to each other and relative to the electronic states of the host, i.e. the valence band (VB) and the conduction band (CB). Since a few years an empirical model developed by P. Dorenbos is available which helps to set the 4f and 5d levels of all lanthanides in an inorganic compound once the position for only one of them is known. The objective of this study on Ln doped sodium lanthanum fluoride, NaLaF₄, was the localization of the di- and trivalent Ln 4f and 5d energy levels by photoluminescence (PL) and thermoluminescence (TL) studies.

The Dorenbos model [1] relies on the observations that for all lanthanides the energy difference between the lowest 5d energy levels and the top of the VB is approximately the same and that the energy of the first 4f-5d transition relative to that in the free Ln ions is lowered nearly by the same amount for all lanthanides. This indicated an almost equal interaction of the Ln 5d levels with the crystal field and

*Chapter 3. Lanthanide 4f Level Location in NaLaF₄:Ln³⁺ and
NaLaF₄:Ce³⁺,Ln³⁺*

effectuates an inversion of the almost host-invariant Dieke diagram in such a way that the variation over the Ln series in the energy difference between the Ln 4f ground state energy (GSE) and the top of the VB reveals independently from the host a characteristic double-seated shape [2]. Thus, knowledge about the absolute 4f GSE location for only one Ln ion suffices to set the ground states of all other ions at the same time. Diverse theoretical attempts using band calculations and cluster models have been made in order to describe the role of the 4f electrons in chemical bonding and to position 4f levels relative to the VB of a host [3]. Unfortunately those calculations are difficult and labor-intensive. In contrast, the energy level scheme according to the Dorenbos model places the 4f and 5d energy levels of the lanthanides based on empirical laws and not on theoretical calculations. Despite its relative simplicity it allows for predictions with a high degree of accuracy. Using the empirical model together with experimental information from VUV spectroscopy, an energy level scheme for NaLaF₄:Ln³⁺ (Ln = La, Ce, Pr, ..., Lu) was constructed. Once such a scheme for NaLaF₄ was available we were able to hypothesize how the Ln ions would behave under high energy irradiation. In NaLaF₄:Ce³⁺,Ln³⁺ for instance, the 4f ground state (GS) of Ce³⁺, being energetically located several eV above the VB, could trap a hole as proposed in Y₂SiO₅ [4,5]. The GS of the second Ln dopant in the divalent form in contrast, if chosen correctly with regard to the energy level diagram, could serve as an electron-trap. By means of TL studies we could verify this kind of hypotheses. The application of the Dorenbos model to TL in this work is an example for its easy, practical use and its possible value in the search of new materials of economic and technological interest.

2. Experimental

2.1. Sample preparation

Powder samples of phase-pure hexagonal NaLaF₄:2% RE³⁺ (RE = Ce, Pr, Nd, Sm, Eu, Gd, Tb, Dy, Ho, Er, Tm) fluorides were prepared from rare-earth oxides Re₂O₃ (Re=La, Ce, Pr, Nd, Sm, Eu, Gd, Tb, Dy, Ho, Er, Tm) of 5N or 6N purity (Metal rare earth ltd.), Na₂CO₃ (Alfa, 5N), and aqueous 47% HBr and 40% HF acids (Merck, supra pure). Batches were typically calculated for 5 g of product. The stoichiometric mixture of the respective rare-earth oxides was dissolved in a small amount of HBr in a Teflon beaker, evaporated to dryness, dissolved in water, and the fluorides MF₃ precipitated with HF. The liquid is evaporated and HF is added again. The appropriate amount of Na₂CO₃ to obtain a 2:1 ratio of Na to M is dissolved in water in a separate beaker and slowly added to the mixture. Care has to be taken to avoid spilling due to the CO₂

Experimental

evolution. The product is dried, and the addition of HF and drying is repeated. The solid, which consists of a mixture of MF_3 , NaF, and NaBr according to X-ray diffraction, is ground up in a mortar, transferred into a glassy carbon boat, and heated to 550 °C in a HF/Ar gas stream for 20 hours. In this step, the reaction towards hexagonal NaMF_4 plus excess NaF takes place. Traces of O and Br are removed by the HF gas stream. The powder is ground up again and heated to 590 °C in an Ar gas stream for another 20 hours. This step improves the crystallinity and optical properties of the material. Finally, the product is washed with water to dissolve the excess NaF and then dried at 100°C. All samples were checked by X-ray powder diffraction. They show the hexagonal NaLaF_4 phase [6, 7] together with a small residue of about 0.5% NaF. NaLaF_4 crystallizes in space group $P\bar{6}$ and has two La^{3+} sites which are randomly occupied by the dopant ions. Both sites have tri-capped trigonal prismatic coordination, one with C_{3h} and the other with C_1 site symmetry, respectively [6]. Since the lanthanides have the same valency and are of comparable size as the lanthanum ions in the NaLaF_4 host compound, a statistical distribution of dopant ions is assumed. They are not expected to cause large lattice distortions and defects. Therefore we expect a minimal number of host related traps which makes it easier to understand the nature of Ln-specific glow peaks.

2.2. Experimental techniques

All photoluminescence spectra were recorded at the Deutsche Elektronen-Synchrotron (DESY) in Hamburg (Germany) using the SUPERLUMI station of HASYLAB. For the excitation spectra the spectral region of excitation was 50–335 nm with a fixed resolution of 0.3 nm. A R6358P Hamamatsu photomultiplier tube (PMT) connected to a triple grating Czerny-Turner monochromator SpectraPro-308i from Acton Research Inc. was used to measure the luminescence from UV to visible wavelengths. All excitation spectra were corrected for the wavelength dependent excitation intensity.

The emission spectra were recorded with a liquid nitrogen cooled CCD detector (Princeton Instruments Inc.), connected to the monochromator described above. The sensitive spectral range was between 200 and 1100 nm with a resolution close to 1 nm. All emission spectra were corrected for the wavelength dependent detection efficiency. All photoluminescence data presented were recorded at 10 K.

The TL measurements were done with a RISØ system (model TL/OSL-DA-15), consisting of an automated TL/OSL reader incorporated into a 386-based PC, a turntable with 48 sample positions and a $^{90}\text{Sr}/^{90}\text{Y}$ beta source with a dose rate of 1mGy s^{-1} . The TL glow curves from the Ln mono-doped samples were recorded using a broad band filter with a transmission range of 320 – 660 nm and a FWHM of 242 nm.

*Chapter 3. Lanthanide 4f Level Location in NaLaF₄:Ln³⁺ and
NaLaF₄:Ce³⁺,Ln³⁺*

For the glow curves from the Ce-Ln co-doped samples a filter with a transmission range of 280 - 380 nm and a FWHM of 70 nm was used. The Ce³⁺ emission is therefore recorded in these latter TL curves. The emitted light of each individually heated sample was detected by a PMT (model 9235QA, Electron Tubes Limited) or rather a CCD camera in case of the λ T-contour plots. In the case of the λ T-contour plots the samples were irradiated with an external ⁶⁰Co source with a dose rate of 4.06 kGy h⁻¹. All TL measurements were done in a nitrogen atmosphere.

3. Results

3.1. Photoluminescence

The excitation spectra of NaLaF₄:Ln³⁺ (Ln = Ce, Pr, Nd, Sm, Eu, Gd) are shown in Figure 1. They were recorded at 10 K. All excitation spectra have a band around 119 nm (accentuated by the dotted line) and a second band at slightly higher energies. NaLaF₄:Eu³⁺ reveals very clearly the fluoride-europium charge transfer (CT) band around 160 nm; the broad bands between 170 and 300 nm are assigned to charge transfer involving oxygen impurities. Both NaLaF₄:Ce³⁺ and NaLaF₄:Gd³⁺ show broad bands around 150 nm which could not be identified. In Figure 1 also the lowest 4f-5d transitions are indicated by vertical lines showing a clear trend to higher energies going from cerium to gadolinium. Figure 2 shows the emission spectra for NaLaF₄:Ln³⁺ (Ln = Ce, Pr, Nd, Sm, Eu, Gd) recorded at 10 K. The emission energies are summarized in Table 1 and attributed to the respective 4f-4f and 5d-4f transitions. The range of the 4f-4f transition energies is given by the Stark components of the corresponding 2J+1 degenerate initial and terminal multiplets. The 5d-4f transitions are relatively high in energy as fluorides tend to have the smallest spectroscopic redshift of all inorganic compounds [9]. NaLaF₄:Ce³⁺ shows under 240 nm excitation the two 5d¹ → 4f¹:²F_J (J = 5/2, 7/2) emissions as two unresolved bands with a peak at 300 nm (33,333 cm⁻¹) and a shoulder at 319 nm (31,348 cm⁻¹). In view of the lowest 4f-5d transition (41,666 cm⁻¹) identified in Figure 1 this gives a Stokes shift of about 8333 cm⁻¹. This relatively large Stokes Shift results from an off-center movement of the Ce³⁺ ion after being excited to the 5d state which in turn causes a strong deformation of the tricapped prism of anions around the cerium ion. According to Andriessen *et al.* it is caused by a reorientation of the occupied states by a pseudo Jahn-Teller coupling to the higher 5d states [10].

Results

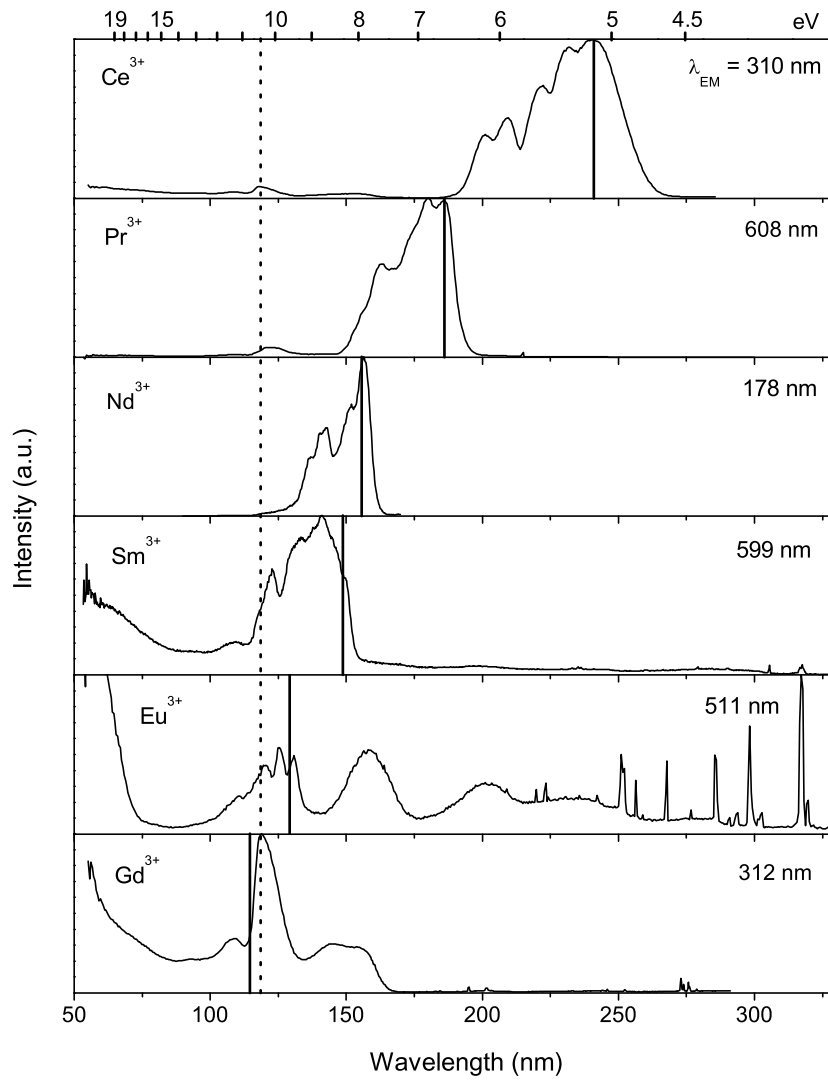


Fig. 1. Excitation spectra of NaLaF₄:Ln³⁺ recorded at 10 K; Ln and emission wavelengths, λ_{EM}, are specified for each spectrum in the Figure.

Chapter 3. Lanthanide 4f Level Location in $\text{NaLaF}_4:\text{Ln}^{3+}$ and $\text{NaLaF}_4:\text{Ce}^{3+},\text{Ln}^{3+}$

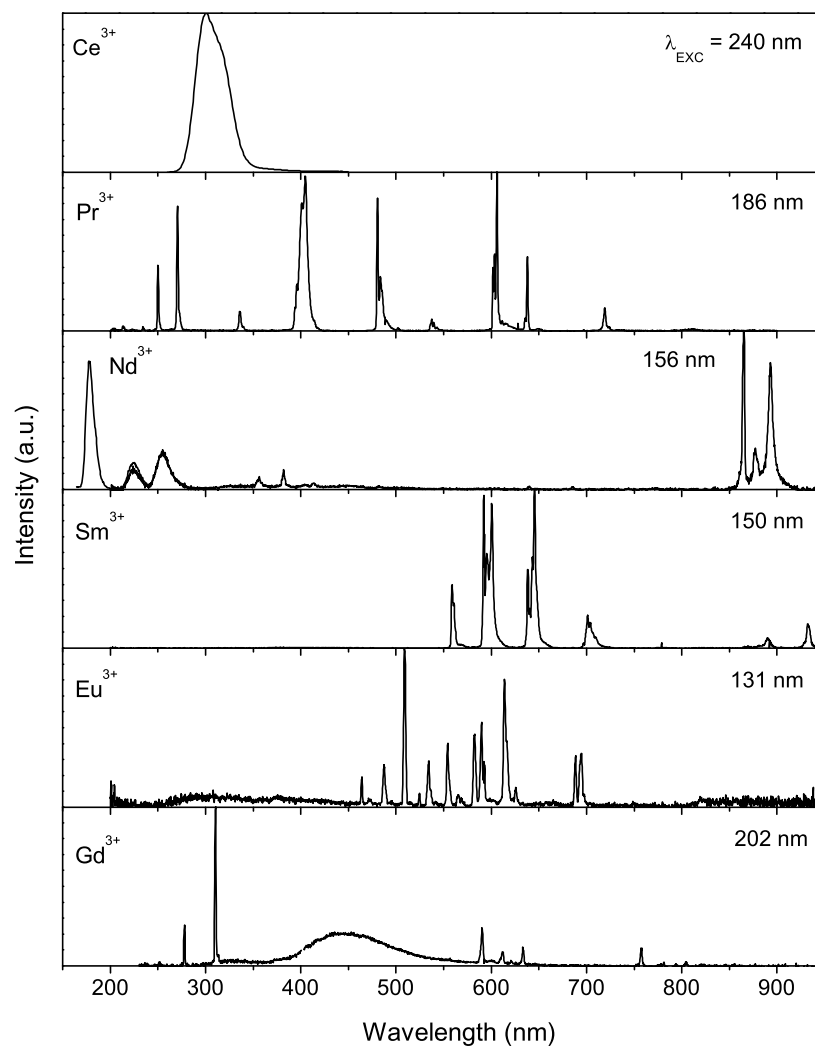


Fig. 2. Emission spectra of $\text{NaLaF}_4:\text{Ln}^{3+}$ recorded at 10 K; Ln and excitation wavelengths, λ_{EXC} , are specified for each spectrum in the Figure.

Results

Table 1. Emission lines and corresponding multiplet transitions for the light Ln dopant ions.

| Ln ³⁺ | Transition | Energy (x 10 ³ cm ⁻¹) |
|--------------------------------|---|---|
| Ce | 5d ¹ → 4f ¹ : ² F _{5/2} | 33.333 |
| | ² F _{7/2} | 31.348 |
| Pr | 4f ² : ¹ S ₀ → ³ F ₄ | 40 |
| | ¹ G ₄ | 37.037 |
| | ¹ D ₂ | 29.411 – 29.850 |
| | ¹ I ₆ | 24.154 – 25.380 |
| | 4f ² : ³ P ₀ → ³ H ₄ | 19.920 – 20.833 |
| | ³ H ₅ | 18.382 – 18.656 |
| | ³ H ₆ | 16.366 – 16.611 |
| | ³ F ₂ | 15.674 – 15.949 |
| | ³ F ₄ | 13.812 – 14.347 |
| Nd | 5d ¹ 4f ² → 4f ³ : ⁴ I _j | 56.179 |
| | ⁴ F _j | 44.643 |
| | ⁴ G _j | 39.370 |
| | 4f ³ : ⁴ D _{3/2} → ⁴ I _{9/2} | 28.090 |
| | ⁴ I _{11/2} | 26.178 |
| | ⁴ I _{13/2} | 24.213 |
| | ⁴ I _{15/2} | 22.321 |
| | 4f ³ : ⁴ F _{3/2} → ⁴ I _{9/2} | 11.198 – 11.560 |
| | Sm | 4f ⁵ : ⁴ G _{5/2} → ⁶ H _{5/2} |
| ⁶ H _{7/2} | | 16.666 – 16.892 |
| ⁶ H _{9/2} | | 15.432 – 15.674 |
| ⁶ H _{11/2} | | 14.084 – 14.347 |
| Eu | ⁶ H _{13/2} | 12.840 |
| | 4f ⁶ : ⁵ D ₂ → ⁷ F ₀ | 21.552 |
| | ⁷ F ₁ | 21.141 – 21.231 |
| | ⁷ F ₂ | 20.408 – 20.576 |
| | ⁷ F ₃ | 19.646 |
| | 4f ⁶ : ⁵ D ₁ → ⁷ F ₀ | 19.083 |
| | ⁷ F ₁ | 18.621 – 18.726 |
| ⁷ F ₂ | 17.605 – 18.050 | |

*Chapter 3. Lanthanide 4f Level Location in NaLaF₄:Ln³⁺ and
NaLaF₄:Ce³⁺,Ln³⁺*

Table 1. (continued)

| Ln ³⁺ | Transition | Energy (x 10 ³ cm ⁻¹) |
|------------------|---|--|
| Eu | 4f ⁶ : ⁵ D ₀ → ⁷ F ₀ | 17.182 |
| | ⁷ F ₁ | 16.863 – 16.949 |
| | ⁷ F ₂ | 15.974 – 16.286 |
| | ⁷ F ₄ | 14.347 – 14.556 |
| Gd | 4f ⁷ : ⁶ I _{7/2} → ⁸ S _{7/2} | 35.971 |
| | 4f ⁷ : ⁶ P _{7/2} → ⁸ S _{7/2} | 31.847 – 32.258 |
| | 4f ⁷ : ⁶ G _{7/2} → ⁶ P _{7/2} | 16.949 |
| | ⁶ P _{5/2} | 16.353 |
| | ⁶ P _{3/2} | 15.797 |
| | ⁶ I _J | 12.804 – 13.227 |

For NaLaF₄:Pr³⁺ an excitation into the 4f¹5d¹ levels of Pr³⁺ results at first in a relaxation to the ¹S₀ level and the ¹S₀ → ³F₄, ¹G₄, ¹D₂, ¹I₆ transitions. A further relaxation from the ¹I₆ state to the ³P_{0,1} levels is followed by emission from ³P₀. The emission lines identified in NaLaF₄:Pr³⁺ were found as well in YF₃:Pr³⁺ [11] at comparable wavelengths. The characteristic 5d-4f emission of NaLaF₄:Nd³⁺ observed in the emission spectrum under 4f²5d¹ excitation was also observed in YPO₄:Nd³⁺, CaF₂:Nd³⁺,Na⁺ and LiYF₄:Nd³⁺ [12]. NaLaF₄:Sm³⁺ shows under excitation in the 4f⁴5d¹ levels of Sm³⁺ only ⁴G_{5/2} → ⁶H_J (J = 5/2, 7/2, 9/2, 11/2, 13/2) transitions. The wavelength region for the different multiplet transitions in NaLaF₄:Eu³⁺ do not differ very much from those found in LiYF₄:Eu³⁺ [13, 14]. After excitation into a 4f⁷:⁶G_J energy level of Gd³⁺ (202 nm), the emission spectrum of NaLaF₄:Gd³⁺ reveals emissions in the long wavelength region due to the ⁶G_{7/2} → ⁶P_J (J = 3/2, 5/2, 7/2) and ⁶G_{7/2} → ⁶I_J transitions as well as in the UV region due to emissions from both the ⁶I_{7/2} and the ⁶P_{7/2} to the ⁸S_{7/2} GS. The excitation spectra reveal the systematic behaviour of the 5d energy states over the Ln series as predicted by the Dorenbos model and will be used to construct the energy level scheme. The emission properties presented here will be used to interpret the TL data that will be presented in the next section

3.2. Thermoluminescence

3.2.1. Ln mono-doped NaLaF₄

Results

In Figure 3 the TL glow curves are plotted wavelength-resolved in a two-dimensional λT -contour plot. It can be seen that the emissions originate from the respective dopant and that the emissions occur mainly, except for $\text{NaLaF}_4:\text{Tb}^{3+}$, in the low-temperature region between 350 and 500 K. In fact, there are only three cases, $\text{NaLaF}_4:\text{Ln}^{3+}$ ($\text{Ln} = \text{Ce}, \text{Pr}, \text{Tb}$), for which an additional band appears around 570 K. We refer to the first band between 350 and 500 K as C1 and to the second band around 570 K as C2 for those three cases (Fig. 4 a). The C1-band is composed of two glow peaks.

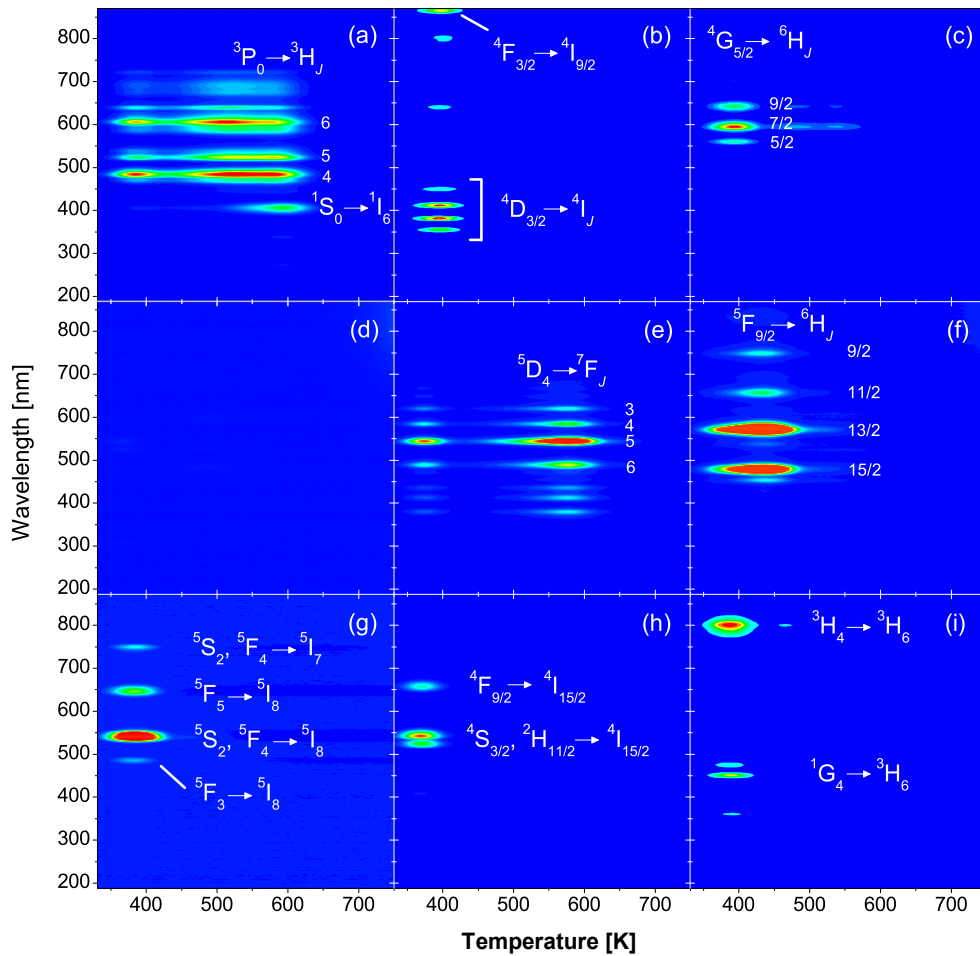


Fig. 3. λT -contour plots of (a) $\text{NaLaF}_4:\text{Pr}^{3+}$, (b) $\text{NaLaF}_4:\text{Nd}^{3+}$, (c) $\text{NaLaF}_4:\text{Sm}^{3+}$, (d) $\text{NaLaF}_4:\text{Gd}^{3+}$, (e) $\text{NaLaF}_4:\text{Tb}^{3+}$, (f) $\text{NaLaF}_4:\text{Dy}^{3+}$, (g) $\text{NaLaF}_4:\text{Ho}^{3+}$, (h) $\text{NaLaF}_4:\text{Er}^{3+}$ and (i) $\text{NaLaF}_4:\text{Tm}^{3+}$ after gamma irradiation of 4 kGy from a ^{60}Co source; heating rate = 5 K/s.

Chapter 3. Lanthanide 4f Level Location in $\text{NaLaF}_4:\text{Ln}^{3+}$ and $\text{NaLaF}_4:\text{Ce}^{3+}, \text{Ln}^{3+}$

Figure 4 b) shows the normalized glow peaks of $\text{NaLaF}_4:\text{Ln}^{3+}$ (Ln = Nd, Dy, Er, Tm) which feature only one TL-band at lower temperatures and no emission at higher temperatures. We call this low temperature TL-band C3. Unlike the C1-band the position of the C3-band depends on the type of Ln dopant. The particular temperature of maximum luminescence intensity increases in the order $\text{Er} < \text{Tm} < \text{Nd} < \text{Dy}$. For $\text{NaLaF}_4:\text{Ln}^{3+}$ (Ln = Sm, Eu, Gd, Yb) either no TL at all (Eu, Yb) or only very weak TL (Sm, Gd) was found.

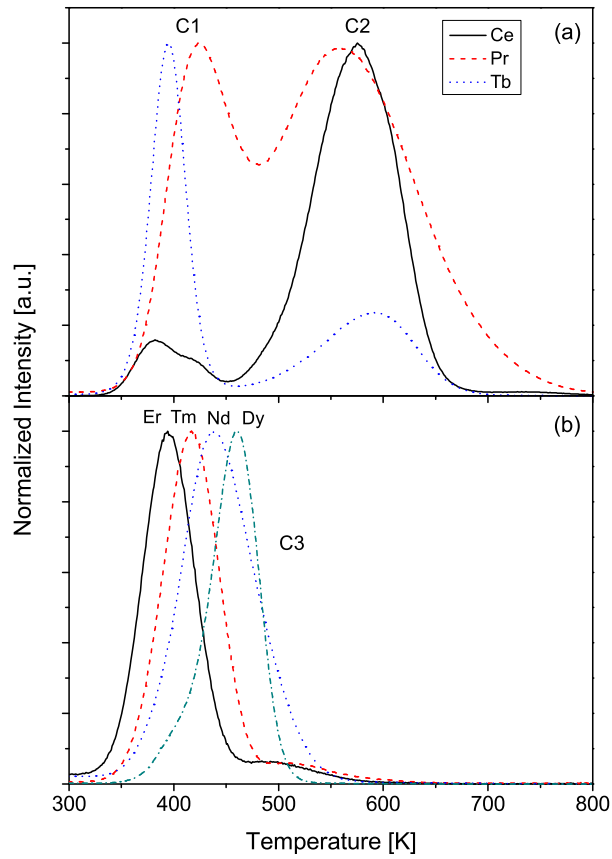


Fig. 4. Normalized glow curves of a) $\text{NaLaF}_4:\text{Ln}^{3+}$ (Ln = Ce, Pr, Tb), and b) $\text{NaLaF}_4:\text{Ln}^{3+}$ (Ln = Nd, Dy, Er, Tm), after beta irradiation of 1280 mGy, recorded with a heating rate of 5 K/s.

Results

We can summarize that the Ln mono-doped NaLaF_4 samples can be divided into three groups, viz. samples with Ln dopants which show (1) two bands C1 and C2, (2) only one band C3, or (3) no TL emission at all.

3.2.2. Ce-Ln co-doped NaLaF_4 and $\text{NaLaF}_4:2\% \text{Ce}^{3+}$

For all Ce-Ln co-doped NaLaF_4 samples mainly the 5d-4f emission of cerium is observed, Figure 5. In Figure 5 (c) no emission can be seen as the upper level of the z -axis is the same for all panels in Figure 5 and the emission of $\text{NaLaF}_4:\text{Ce}^{3+}$, Sm^{3+} is relatively low in intensity; nevertheless a faint spot around 320 nm can be identified when the upper level of the z -axis is lowered [26].

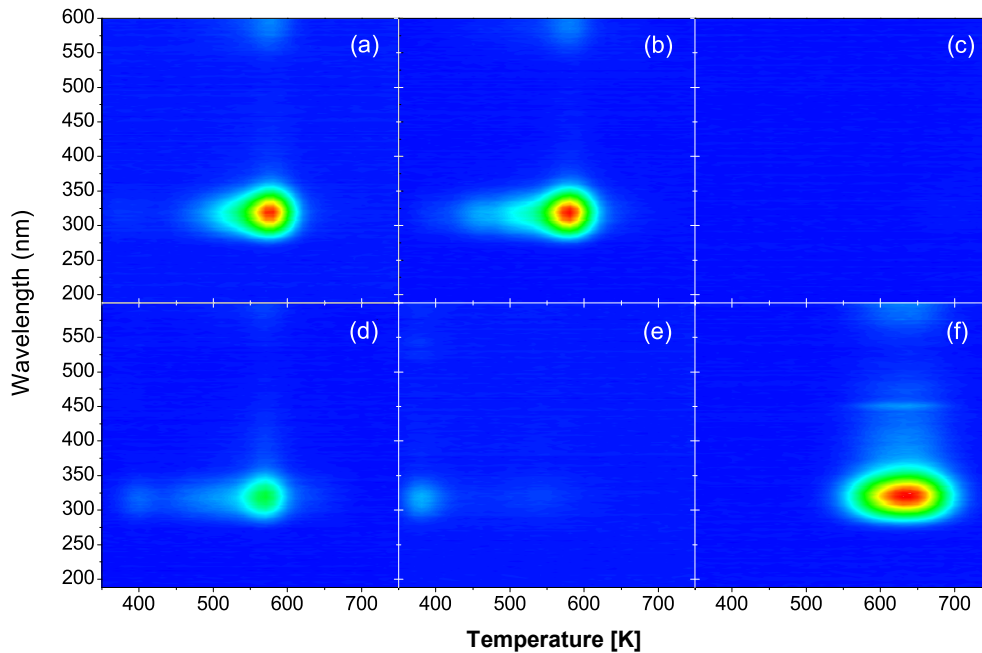


Fig. 5. λT -contour plots of (a) $\text{NaLaF}_4:\text{Ce}^{3+}$, (b) $\text{NaLaF}_4:\text{Ce}^{3+},\text{Nd}^{3+}$, (c) $\text{NaLaF}_4:\text{Ce}^{3+},\text{Sm}^{3+}$, (d) $\text{NaLaF}_4:\text{Ce}^{3+},\text{Ho}^{3+}$, (e) $\text{NaLaF}_4:\text{Ce}^{3+},\text{Er}^{3+}$ and (f) $\text{NaLaF}_4:\text{Ce}^{3+},\text{Tm}^{3+}$ after gamma irradiation of 4 kGy from a ^{60}Co source; heating rate = 5 K/s.

The normalized glow curves for $\text{NaLaF}_4:\text{Ce}^{3+},\text{Ln}^{3+}$ (Ln = Sm, Er, Tm) and $\text{NaLaF}_4:\text{Ce}^{3+}$ are shown in Figure 6. They all show a band between 350 and 450 K

which is composed of two glow peaks and will be referred to also as C1 as in the case of $\text{NaLaF}_4:\text{Ln}^{3+}$ (Ln = Ce, Pr, Tb). Additionally to the C1-band, Figure 6 reveals a second band with its temperature for maximum luminescence intensity varying between 470 and 800 K. This band was not observed before and will be called C4 for all Ce-Ln co-doped NaLaF_4 samples. The temperature for maximum intensity of C4 increases in the order $\text{Ce, Ho} < \text{Ce, Tm} < \text{Ce, Sm}$, see Figure 6. This behavior was also observed in $\text{YPO}_4:\text{Ce}^{3+},\text{Ln}^{2+}$ [15] and $\text{Ca}_2\text{MgSi}_2\text{O}_7:\text{Eu}^{2+},\text{Ln}^{3+}$ [16].

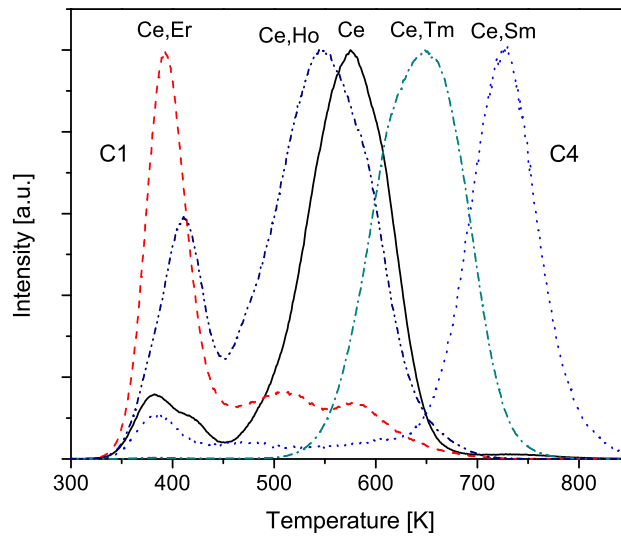


Fig. 6. Normalized glow curves of $\text{NaLaF}_4:\text{Ce}^{3+}$ and $\text{NaLaF}_4:\text{Ce}^{3+},\text{Ln}^{3+}$ (Ln = Sm, Ho, Er, Tm) after beta irradiation of 1280 mGy, recorded with a heat rate of 5 K/s.

4. Discussion

4.1. Photoluminescence and Energy Level Diagram

4.1.1. Ln^{2+} 4f GSE location

The band around 119 nm in the excitation spectra (Figure 1, left hand) is assigned to exciton creation. The second band around 108 nm (11.5 eV) in $\text{NaLaF}_4:\text{Ce}^{3+}$ has been identified by us as the band gap. In the case of $\text{NaLaF}_4:\text{Eu}^{3+}$ the fluoride-europium charge transfer (CT) band, $E^{\text{CT}}(6,3+,A)$, can be clearly seen at about 160 nm, thus

Discussion

setting the ${}^8S_{7/2}$ GS of Eu^{2+} ($4f^7$) approximately 7.7 eV above the top of the VB. The location of the $4f^{n+1}$ ground states of all other divalent lanthanides can now be obtained using [1]

$$E_{\text{Vf}}(n+1, 2+, A) = E^{\text{CT}}(6, 3+, A) + \Delta E_{\text{Vf}}(n+1, 7, 2+), \quad (1)$$

where $E_{\text{Vf}}(n+1, 2+, A)$ is the energy difference between the top of the VB of a compound A and the $4f^{n+1}$ GSE of a divalent Ln dopant ion and $\Delta E_{\text{Vf}}(n+1, 7, 2+)$ denotes the average energy difference between that ion and the $4f^7 \cdot {}^8S_{7/2}$ energy level of Eu^{2+} . The values for $\Delta E_{\text{Vf}}(n+1, 7, 2+)$ are known [17]. The $4f$ ground state energies for the divalent Ln dopant ions obtained in this way are shown, relative to the VB and the CB of NaLaF_4 , in Fig. 7.

4.1.2. Ln^{3+} $4f$ GSE location

The positioning of the $4f$ ground state energies for the trivalent lanthanides is trickier than that for the divalent dopant ions as we do not observe any CT bands to tetravalent Ln ions and we have no experimental indications of $5d$ energy level locations relative to the electronic host states. We have indications, however, that in wide band gap compounds like fluorides the energy difference between the $4f^6$ GSE of Eu^{3+} and the $4f^7$ GSE of Eu^{2+} is between 6.6 and 7.3 eV [17, 18]. We also found that for Ln mono-doped NaLaF_4 four samples, viz. $\text{NaLaF}_4:\text{Ln}^{3+}$ ($\text{Ln} = \text{Sm}, \text{Eu}, \text{Gd}, \text{Yb}$), either do not show glow peaks at all or at least, as for $\text{NaLaF}_4:\text{Sm}^{3+}$ and $\text{NaLaF}_4:\text{Gd}^{3+}$, only very weak emission. It will be explained in the next section that the presence of glow peaks with emission from the Ln dope additive requires the $4f^n$ GSE being sufficiently above the VB. Keeping this in mind we can conclude that for Sm, Eu, Gd and Yb the $4f^n$ ground states must lie either quite close to the VB or even inside of it. We will adopt the 6.7 eV for the $\text{Eu}^{3+}/\text{Eu}^{2+}$ energy difference mentioned above. The ${}^8S_{7/2}$ GS of Gd^{3+} is then energetically placed just below the top of the VB, see Figure 7. Using the average energy difference between the GSE of a trivalent Ln ion and the ${}^8S_{7/2}$ GSE of Gd^{3+} given in [17] we can now place the $4f^n$ ground state energies of all other trivalent Ln ions. In so doing we get a complete energy level diagram for NaLaF_4 which is shown in Figure 7.

4.2. Electron- and hole-traps

Under MeV energy beta or gamma irradiation many electrons will be raised from the VB to the CB. Now, apart from relaxing back to the VB in order to recombine with the holes left behind, the excited electrons may be trapped either by host defects or the lanthanide impurities. Trivalent lanthanides can trap electrons ($\text{Ln}^{3+} + e^- \rightarrow \text{Ln}^{2+}$) when

Chapter 3. Lanthanide 4f Level Location in $\text{NaLaF}_4:\text{Ln}^{3+}$ and
 $\text{NaLaF}_4:\text{Ce}^{3+}, \text{Ln}^{3+}$

their 4f GSE in the divalent form is located below the CB. As it can be seen in Figure 7 this holds for all lanthanides other than La, Ce and Gd. The holes in contrast polarize the lattice and either form self-trapped holes (V_k -centers) or they are trapped by Ln dopants ($\text{Ln}^{3+} + h \rightarrow \text{Ln}^{4+}$). When a V_k -center is formed it can be stabilized in turn by a lattice defect or an Ln impurity [19, 20]. Below, a V_k -center stabilized by a defect will be termed V_{kA} -center. A V_{kA} -center-release means the liberation of the V_k -center from that defect. Only if the 4f GSE of the lanthanide dopant (relative to the VB) is located above the V_{kA} -center energy, E_A , the hole can be trapped in the 4f state of the lanthanide. The energy of V_k -centers is not affected very much by different fluoride host lattices [21] and the difference between the VB and the GSE of the V_k -center is known to be in the order of few eV [22, 23].

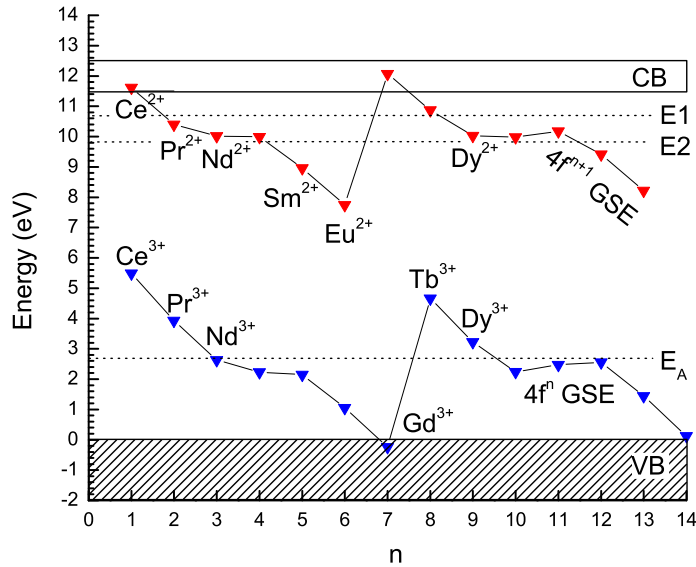


Fig. 7. Energy level scheme for $\text{NaLaF}_4:\text{Ln}^{3+}$ showing the Ln^{2+} ($4f^{n+1}$) and Ln^{3+} ($4f^n$) ground states. The activation energies E_1 , E_2 and the V_{kA} -center energy E_A are indicated by dashed lines.

4.3. Thermoluminescence

Based on the possible electron- and hole-traps described in the last section we can now construct a model which is able to explain the observed TL properties of each sample. This can be done by assuming only two host related electron traps with

Discussion

activation energies E1 and E2. With it, two principal processes are thinkable leading to the observed glow peaks, viz. (1) an electron being released from an E1-, or E2-trap or an Ln^{2+} impurity, recombining with a hole trapped at a trivalent Ln dopant, and (2) a thermal liberation and transfer by hopping of either the V_{kA} -center or of the Ln-trapped hole with subsequent recombination with a divalent Ln ion forming an excited state of Ln^{3+} . The decay of this excited state results in TL with an emission spectrum characteristic for the Ln^{3+} ion. Recombination of a released hole with an electron in E1- or E2 traps is in principle possible. If it occurs it is a non-radiative recombination.

4.3.1. Activation Energy

The activation energy for both the electron- and hole-traps was obtained assuming first order kinetics, i.e. neglecting re-trapping during heating. In this case the condition for the maximum thermoluminescence intensity can be written as an Arrhenius equation [24],

$$\ln\left(T_m^2/\beta\right) = E/k_B T_m + \ln(E/k_B s), \quad (4)$$

where β is the heating rate (in K/s), E the activation energy or trap depth, k_B the Boltzmann constant, s the frequency factor (in s^{-1}) and T_m the temperature for which the luminescence intensity is maximal. Plotting equation (4) against $1/k_B T_m$ (heating rate plots) results in a straight line with slope E and an intercept of $\ln(E/s \cdot k_B)$.

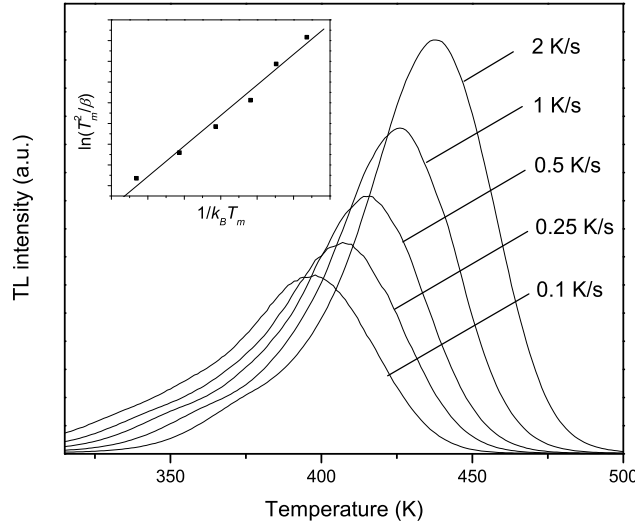


Fig. 8. Glow curves for $\text{NaLaF}_4:\text{Dy}^{3+}$ for different heating rates after a dose of 1280 mGy; the inset shows corresponding heating rate plot.

Chapter 3. Lanthanide 4f Level Location in $\text{NaLaF}_4:\text{Ln}^{3+}$ and $\text{NaLaF}_4:\text{Ce}^{3+},\text{Ln}^{3+}$

In Figure 8 both the glow curves for different heating rates and the heating rate plot are shown for $\text{NaLaF}_4:\text{Dy}^{3+}$. It can be seen that the luminescence intensity decreases with decreasing β . This behavior was also observed in all other samples except for $\text{NaLaF}_4:\text{Nd}^{3+}$. We have observed this behavior earlier in $\text{YPO}_4:\text{Ce}^{3+},\text{Sm}^{3+}$ and explained it by fading before and during read-out due to center-to-center recombination of electrons trapped by Sm^{3+} with holes on the Ce^{3+} site [15]. The fact that the points in the heating rate plot indicate a slightly parabolic behavior rather than a straight line may be caused by a temperature gradient between the heating element and the sample surface [25].

4.3.2. Ce-Ln co-doped NaLaF_4

In the case of Ce-Ln co-doped NaLaF_4 it was noticed earlier that all TL was mainly due to 5d-4f cerium emission, see Figure 5. The energy level diagram (Figure 7) shows that the GSE of divalent cerium is above the CB whereas the GS of trivalent cerium is located inside the band gap, well above the VB. Ce^{3+} is therefore a very stable hole-trap ($\text{Ce}^{3+} + h \rightarrow \text{Ce}^{4+}$). It suggests that the only possibility for charge carrier recombination is an electron recombining with tetravalent cerium leaving an excited state of cerium in the trivalent form: $\text{Ce}^{4+} + e^- \rightarrow (\text{Ce}^{3+})^*$. It now comes to finding the origin of the electron. The TL curves of all Ce-Ln co-doped samples show two bands, viz. C1 and C4. The C1-band is composed of two glow peaks and is situated at the same temperature for all types of Ln^{3+} co-dopants. This indicates that it is due to an electron-release from a host related E1-trap. The C4-band in contrast varies with the Ln^{3+} co-dopant (see Fig. 6). As the $4f^{n+1}$ ground state energies of all divalent Ln ions in question are located below the CB, it is obvious to explain the Ln-specific C4-band by an electron-release from those dopants: $\text{Ln}^{2+} \rightarrow \text{Ln}^{3+} + e^-$. Thus, the order of the different C4-bands shown in Figure 6 reflects a trend in the energy difference between the $4f^{n+1}$ GSE and the CB as expected from the Dorenbos model and shown in Figure 7. Now, aside from $\text{NaLaF}_4:\text{Ce}^{3+},\text{Sm}^{3+}$ and $\text{NaLaF}_4:\text{Ce}^{3+},\text{Tm}^{3+}$, the C4-band is located between 470 and 650 K in all Ce-Ln co-doped NaLaF_4 cases, overlapping strongly with the corresponding band (C2) in $\text{NaLaF}_4:\text{Ce}^{3+}$. Looking at Fig. 7 we see that the 4f GS of Ce^{2+} is located inside the CB. Since the C2-band in $\text{NaLaF}_4:\text{Ce}^{3+}$ must therefore be due to an electron-release from a host related E2-trap, we have to assume a contribution of the E2-trap also in $\text{NaLaF}_4:\text{Ce}^{3+},\text{Ln}^{3+}$. In most cases the C4-band is composed of an undefined number of glow peaks. Peak separation was only possible for $\text{NaLaF}_4:\text{Sm}^{3+}$ and $\text{NaLaF}_4:\text{Tm}^{3+}$. Additionally, their C4-bands are at perspicuously higher temperatures compared to all other Ce-Ln co-doped NaLaF_4 samples and therefore, in these two cases we attribute the C4-band to an electron-release from the

Discussion

respective divalent $4f^{n+1}$ ground states. Table 2 contains the activation energies derived from C4 for those two samples and information about the relative luminescence intensity, I_{rel} , and T_m of all investigated co-doped samples.

Table 2. Relative luminescence intensity, I_{rel} , activation energy, E [eV], natural logarithm of the frequency factor s , and glow peak maximum, T_m [K] in K for the C4-band in Ce-Ln co-doped NaLaF₄.

| Dopants | $I_{rel}(C4)$ | $T_m(C4)$ | $E(C4)$ | $\ln(s)$ |
|---------|---------------|-----------|---------|----------|
| Ce, Nd | 0.99 | 601 | --- | --- |
| Ce, Sm | 0.05 | 726 | 1.48 | 19.49 |
| Ce, Dy | 0.48 | 590 | --- | --- |
| Ce, Ho | 0.29 | 543 | --- | --- |
| Ce, Er | 0.21 | --- | --- | --- |
| Ce, Tm | 1 | 646 | 1.42 | 22.21 |
| Ce, Yb | 0 | --- | --- | --- |

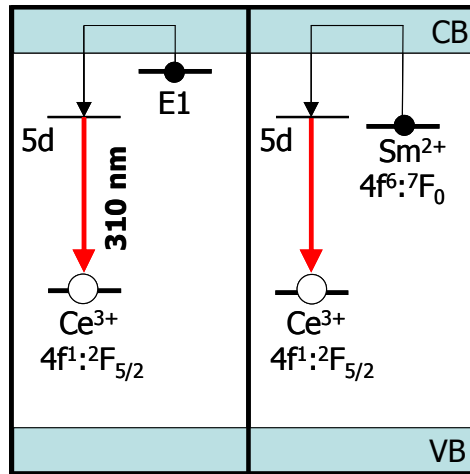


Fig. 9. Model explaining the origin of the glow curves for NaLaF₄:Ce³⁺, Sm³⁺.

The $4f^{n+1}$ ground state energies of Sm²⁺ and Tm²⁺ found via glow peak analysis (see Table 2) are about 0.96 and 0.56 eV respectively closer to the CB than the ones obtained from the fluoride-europium CT band and the Dorenbos model (Figure 7). One reason for this difference might be that the C4-bands for NaLaF₄:Ce³⁺,Sm³⁺ and NaLaF₄:Ce³⁺,Tm³⁺ could still be composed of more than one peak making it difficult to

*Chapter 3. Lanthanide 4f Level Location in NaLaF₄:Ln³⁺ and
NaLaF₄:Ce³⁺,Ln³⁺*

establish the right T_m value. Another reason could be a wrong assignment of the band gap in the excitation spectra of NaLaF₄:Ln³⁺ (see Results Section, Fig. 1). The notable differences in luminescence intensities are not understood yet. In general, the luminescence intensities of the co-doped samples are about half as intensive as the ones of the mono-doped samples.

In Figure 9 the main recombination process for the co-doped samples is depicted exemplary for NaLaF₄:Sm³⁺. The C1-band is due to an electron-release from the E1-trap (Fig. 9, left part), whereas the C4-band originates from an electron-release from the rather deep lying 4f GSE of divalent samarium (Fig. 9, right). The contribution from the E2-trap is missing. This might indicate that Sm ions trap electrons more efficiently than host related electron traps or that the electrons from E2-traps relax to the ⁷F₀ GS of Sm²⁺.

4.3.3. Ln mono-doped NaLaF₄

For NaLaF₄:Ln³⁺ we found that the TL was due to 4f-4f emission of the Ln³⁺ dope additive (see Fig. 3). So, in principle we can think of two different charge carrier recombination processes: (1) an electron recombines with an Ln-trapped hole giving an excited 4f state of Ln³⁺: Ln⁴⁺ + e⁻ → (Ln³⁺)*. (2) A hole recombines with an Ln-trapped electron resulting in an excited 4f state of Ln³⁺: Ln²⁺ + h → (Ln³⁺)*. Now it comes to asking about the origin of either an electron or a hole. We know that only NaLaF₄:Ln³⁺ (Ln = Ce, Pr, Tb), whose Ln dopants 4f^{*n*} ground states are deep hole traps, show two glow bands, C1 and C2 (Fig. 4 a). All other mono-doped samples feature solely the C3-bands (Fig. 4 b). For explaining the two TL bands in NaLaF₄:Ln³⁺ (Ln = Ce, Pr, Tb) we can use the same argument as in the last section, that is the assumption of (1) an electron-release from an E1-trap for explaining the C1-band and (2) an electron-release exclusively from an E2-trap (Ce) or together with an electron-release from a divalent Ln ion (Pr, Tb) in order to explain the C2-band. The other Ln mono-doped NaLaF₄ cases show only the C3-band, as already mentioned. In Table 3 the activation energies, $E(C3)$, for the C3-band are shown. Apart from Dy³⁺ they are almost the same for all dopants with an average of 0.73 eV. As dysprosium has a higher activation energy than all the other Ln dopants, the C3-band can not be due to an electron-release neither from a host related E1-trap nor from the divalent Ln dopant ions. The 4f^{*n+1*} ground state energies of the latter are not so different from the one of dysprosium so that in case of an electron release from the Ln²⁺ ions we would expect similar activation energies for all of these dopants (see Fig. 7). Thus, we deal with a hole-release as the only remaining possibility. The 0.73 eV activation energy of the C3-band is assumed to be the total energy needed to thermally free a V_{kA}-centre and to transfer the hole via a hopping mechanism to the GS of a divalent Ln dopant.

Discussion

Dy^{3+} in contrast not only features its glow peak at the relative highest temperature (460 K) but shows also the most intense TL luminescence of all dopants. We assume the corresponding activation energy of 1.06 ± 0.04 eV in this case not to indicate a V_{kA} -centre-release but a hole-release from dysprosium together with hole transfer by hopping. The reason for this assumption is the relative large energy difference between the top of the VB and the ${}^6\text{H}_{15/2}$ Dy^{3+} state compared to all other Ln ions except for Ce, Pr and Tb. The 4f ground state energies of those three latter ions are located so high above the VB that the energy needed to free the hole exceeds the activation energies E1 and E2 so that in this case recombination with ensuing luminescence will be achieved by electron-release via the CB. The GSE of the V_{kA} -center, E_{A} , must be located between the Dy^{3+} and the Ho^{3+} , Er^{3+} and Tm^{3+} 4f ground states at about 2.7 eV above the top of the VB; it is indicated in Figure 7 as a dotted line. This value is very realistic for V_{kA} -centers in fluorides.

Table 3. Relative luminescence Intensity, I_{rel} , temperature for maximum luminescence intensity, T_m [K], activation energy, E [eV], natural logarithm of the frequency factor s and the frequency factor relative to Dy, s_{rel} , for the C3-band in Ln mono-doped NaLaF_4 .

| Dopant | $I_{\text{rel}}(\text{C3})$ | $T_m(\text{C3})$ | $E(\text{C3})$ | $\ln(s)$ | s_{rel} |
|--------|-----------------------------|------------------|----------------|----------|------------------|
| Ce | --- | 378 | 0.74 | --- | --- |
| Pr | 0.05 | 419 | 0.71 | 19.36 | 0.001 |
| Nd | 0.07 | 438 | 0.75 | 19.10 | 0.001 |
| Sm | 0.0001 | 464 | 0.71 | 18.88 | 0.0007 |
| Gd | 0.001 | 401 | 0.68 | 19.08 | 0.001 |
| Tb | 0.1 | 392 | 0.76 | 22.37 | 0.02 |
| Dy | 1 | 460 | 1.06 | 26.20 | 1 |
| Ho | 0.01 | 403 | 0.76 | 21.73 | 0.01 |
| Er | 0.01 | 394 | 0.73 | 20.95 | 0.01 |
| Tm | 0.02 | 416 | 0.72 | 19.33 | 0.001 |

In order to explain the origin of the Ln specific glow peaks Raymond et al. [17] and Yang et al. [18] analyzed the relation between T_m and the ionic radii of the lanthanides. Here we want to turn the attention to the relation between the relative luminescence Intensity, I_{rel} , and the average energy difference between the ${}^6\text{H}_{15/2}$ GSE of dysprosium and the 4f ground state energies of the other trivalent Ln ions, $\Delta E_{\text{VF}}(n,9,3+)$ (depicted in Fig. 10).

It can be clearly seen that the luminescence intensity does not only depend on the location of the 4fⁿ ground states relative to the top of the VB but also relative to the presumable location of the V_{kA} -center GSE. The high luminescence intensity in

Chapter 3. Lanthanide 4f Level Location in NaLaF₄:Ln³⁺ and NaLaF₄:Ce³⁺,Ln³⁺

NaLaF₄:Dy³⁺ might indicate a higher hole trapping efficiency of lanthanides than of V_K-centers once the Ln³⁺ 4fⁿ GSE is located above the V_{kA}-center energy. By comparing column 2 with column 6 of Table 3 a correlation of the luminescence intensity with the frequency factor can be seen. The Ln-specific frequency factor correlates also roughly with the temperature for the highest TL intensity of the C3-band (see Fig. 4 b). In Figure 11 our model is further illustrated, explaining the conjectured internal processes leading to the glow curves of NaLaF₄:Ln³⁺ (Ln = Ce, Tb, Sm, Dy). Both for NaLaF₄:Ce³⁺ and NaLaF₄:Tb³⁺ the two glow bands labeled above C1 and C2 can be seen in Figure 4 a). Within the model those two bands are due to the two different electron E1- and E2-traps respectively. Being thermally released from the traps the electrons excite in NaLaF₄:Ce³⁺ via the CB the Ce³⁺ ions resulting in the characteristic 5d-4f emission (see Figure 11 a).

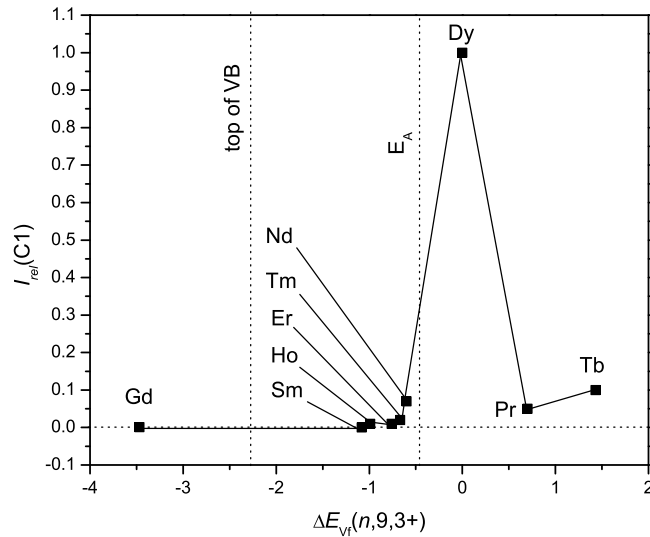


Fig. 10. Relative luminescence intensity, $I_{rel}(C1)$ versus $\Delta E_{Vf}(n,9,3+)$ in NaLaF₄:Ln³⁺. Ln is specified inside the Figure. Top of VB and lattice defect energy, E_A , relative to the VB are indicated by dotted vertical lines.

In NaLaF₄:Tb³⁺ the Tb²⁺ 4f⁹:⁶H_{15/2} GS may additionally act as an electron-trap as it lies below the CB, though closer to it than E1 and E2 (see Figure 11 b, left part). Now, besides Ce, Pr and Tb, all other Ln mono-doped samples feature (if at all) only the C3-band while having no band at higher temperatures. In Figure 12 c) and d) this is exemplified for NaLaF₄:Sm³⁺ and NaLaF₄:Dy³⁺. Their 4fⁿ⁺¹ ground states, 4f⁶:⁷F₀ (Sm²⁺) and 4f¹⁰:⁵I₈ (Dy²⁺) respectively, both lie energetically below the CB, thus being

Discussion

able to trap electrons. In addition their $4f^n$ ground state energies are located closer to the VB than the ones of Ce, Pr and Tb so that in these cases a hole-release must also be considered; either via the liberation of the V_{kA} -centre as in the case of Sm^{3+} (Figure 11 c) or from the Ln dopant itself as in the case of Dy^{3+} (Figure 11 d).

After being released from Dy^{3+} , the hole will be trapped in form of a V_k -center which then is transferred by hopping to a Dy^{2+} ion. The type of release depends on the locations of the $4f$ ground states relative to the V_{kA} -center GSE. The same holds for all other Ln ions except Eu, Gd and Yb as their $4f$ ground states are located too close to or even inside the VB. The reason why no TL was found in $NaLaF_4:Eu^{3+}$ could be due to fading between the V_{kA} -center GSE, E_A , and the GSE of Eu^{2+} . The activation energies E_1 and E_A appear to be of similar magnitude so that both corresponding traps contribute to the glow band called C3. Therefore it is not always possible to separate them.

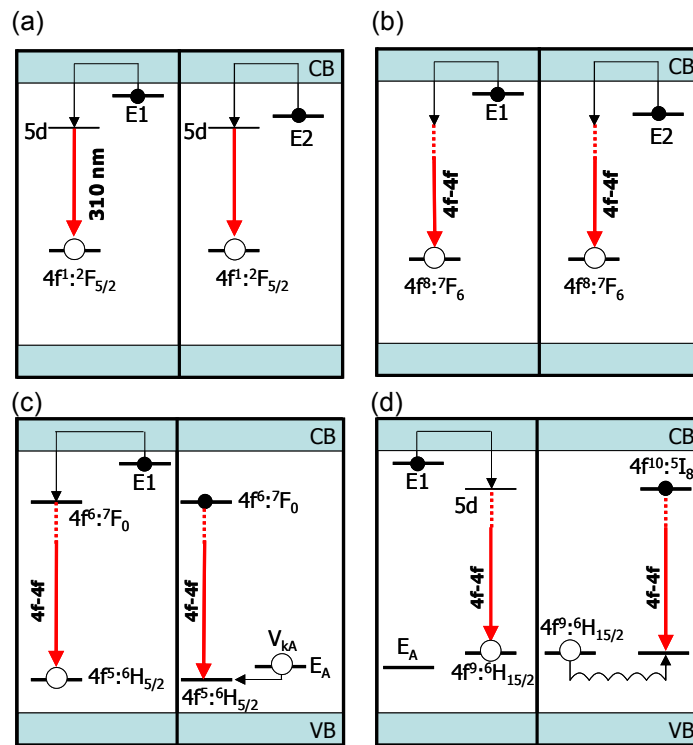


Fig. 11. Model explaining the origin of the glow curves for a) $NaLaF_4:Ce^{3+}$; b) $NaLaF_4:Tb^{3+}$; c) $NaLaF_4:Sm^{3+}$ and d) $NaLaF_4:Dy^{3+}$.

5. Conclusion

Based on PL-, TL-spectra and information from literature about the energy difference between the 4f⁶ GSE of Eu³⁺ and the 4f⁷ GSE of Eu²⁺ in wide band gap compounds a complete energy level diagram for NaLaF₄:Ln³⁺ was constructed. This diagram motivated TL measurements on Ln mono- and Ce-Ln co-doped NaLaF₄. In the Ln mono-doped NaLaF₄ case we found that the TL was due to 4f-4f emission from the Ln³⁺ dopant ion. NaLaF₄:Ln³⁺ (Ln = Ce, Pr, Tb) show 2 TL-bands, whereas NaLaF₄:Ln³⁺ (Ln = Nd, Dy, Ho, Er) feature only one TL-band. NaLaF₄:Ln³⁺ (Eu, Gd, Yb) show either no or very weak TL. In Ce-Ln co-doped NaLaF₄ the TL emission was mainly due to 5d-4f emission from Ce³⁺. It was shown that in addition to the energy level diagram only two assumptions, viz. the presence of two host related electron traps and the presence of V_k-centers, are necessary for explaining the Ln-specific glow peaks. Thus, we can conclude that (1) an Ln ion can serve as an electron trap only when its Ln²⁺ 4fⁿ⁺¹ GSE is located below or close to the activation energies of the host related E1- and E2-electron-traps relative to the CB; (2) an Ln ion can serve as a hole trap only when its Ln³⁺ 4fⁿ GSE is located above the V_{kA}-center GSE, E_A, relative to the VB.

Acknowledgements

This work was supported by the Dutch Technology Foundation (STW) and by the IHP-Contract HPRI-CT-1999-00040 of the European Commission. We thank D. Biner for the preparation of the NaLaF₄ samples.

References

References

- [1] Dorenbos P., *J. Lumin.*, 108, 301 (2004)
- [2] van der Kolk E., *Chem Mater.*, 18, 3458 (2006)
- [3] Gubanov V.A., Ryzhkov, *J. Struct. Chem.*, 27, 781 (1987)
- [4] Meijerink A., Schipper W.J., Blasse G., *J. Phys. D: Appl. Phys.*, 24, 997 (1991)
- [5] Meiss D., Wischert W., Kemmler-Sack S., *Mater. Chem. Phys.*, 38, 191 (1994)
- [6] Aebischer, A., Hostettler M., Hauser J., Krämer K. W., Weber T., Güdel H.U., Bürgi H.B., *Angew. Chem. Int. Ed.*, 45, 2802 (2006)
- [7] Krämer K.W., Biner D., Frei G., Güdel H.U., Hehlen M.P., Lüthi S. R., *Chem. Mater.*, 16, 1244 (2004)
- [8] Zachariasen W. H., *Acta Crystallogr.*, 1, 265 (1948)
- [9] Dorenbos P., *Phys. Rev. B*, 62, 15640 (2000)
- [10] Andriessen J., van der Kolk E., Dorenbos P., *Phys. Rev. B*, 76, 075124 (2007)
- [11] Kück S., Sokólska I., Henke M., Osiac E., *Chem. Phys.*, 310, 139 (2005)
- [12] Pieterse L. van, *Proefschrift Universiteit Utrecht*, ISBN 90-393-2779-3 (2001)
- [13] Görrler-Walrand C., Behets M., *Inorg. Chim. Acta*, 109, 83 (1985)
- [14] Bihari B., Sharma K.K., Erickson L.E., *J. Phys. Condens. Matter*, 2, 5703 (1990)
- [15] Dorenbos P., Bos A.J.J., *Rad. Meas.*, Article in Press, doi:10.1016/j.radmeas.2007.10.007
- [16] Aitasalo T., Hölsä J., Kirm M., Laamanen T., Lastusaari M., Niittykoski J., Raud J., Valtonen R., *Rad. Meas.*, 42, 644 (2007)
- [17] Dorenbos P., *J. Phys.: Condens. Matter*, 15, 8417 (2003)
- [18] Dorenbos P., van der Kolk E., *Appl. Phys. Lett.*, 89, 061122 (2006)
- [19] Raymond S.G., Luff B.J., Townsend P.D., Xiqi Feng, Guanqing Hu, *Rad. Meas.*, 23, 195 (1994)
- [20] Yang B., Townsend P.D., Rowlands A.P., *Phys. Rev. B*, 57, 178 (1998)
- [21] Patton F.W., Marrone M.J., *Phys. Rev.*, 142, 513 (1966)
- [22] Norman Jette A., Gilbert T.L., Das T.P., *Phys. Rev.*, 184, 844 (1969)
- [23] Stoneham A.M., *Theory of Defects in Solids: Electronic Structure of Defects in Insulators*

*Chapter 3. Lanthanide 4f Level Location in NaLaF₄:Ln³⁺ and
NaLaF₄:Ce³⁺,Ln³⁺*

and Semiconductors, Oxford University Press, ISBN-10: 0198507801 (2001)

- [24] Chen R., McKeever S.W.S., *Theory of Thermoluminescence and Related Phenomena*, World Scientific, ISBN: 9-810222-95-5 (1997)
- [25] Pijters T.M., Bos A.J.J., *J. Phys. D: Appl. Phys.*, **27**, 1747 (1994)
- [26] Krumpel A.H., van der Kolk E., Zeelenberg D., Bos A.J.J., Krämer K.W., Dorenbos P., *J. Appl. Phys.*, **104** (2008) 073505

Chapter 4

Controlled Electron and Hole Trapping in YPO₄:Ce³⁺,Ln³⁺ and LuPO₄:Ce³⁺,Ln³⁺ (Ln = Sm, Dy, Ho, Er, Tm)

Abstract

A detailed and systematic electron trapping study was conducted in the scientifically important wide band-gap materials LuPO₄ and YPO₄ doubly doped with Ce³⁺ and Ln³⁺ (Ln = Sm, Dy, Ho, Er, Tm). By using vacuum ultraviolet luminescence spectroscopy and detailed thermo-luminescence spectroscopy it was possible to establish by two independent methods that the observed electron traps can be assigned to the Ln³⁺ co-doping ions. It is shown that the associated electron trap depths are determined by the energy separation between the Ln²⁺ ground states and the bottom of the conduction band. Both methods reveal a systematic behavior of electron trap depths as a function of the type of Ln³⁺ co-doping ion that can be explained by recently developed empirical models. Small differences in trap depths obtained by the two methods are discussed in the context of charge transfer induced relaxation processes and uncertainties in glow peak analysis. Our experiments provide valuable information on $4f^n \leftrightarrow 4f^n$, $4f^n \rightarrow 4f^{n-1}5d$, $O^{2-} \rightarrow Ln^{3+}$ charge transfer and the lowest energy PO₄³⁻ group transitions as well as electron trap depths. These transition energies allowed us to construct a complete energy level diagram for LuPO₄:Ln^{3+/2+} and YPO₄:Ln^{3+/2+}.

1. Introduction

Doubly lanthanide doped insulators like SrAl₂O₄:Eu,Dy [1, 2], CaGa₂S₄:Eu²⁺,Ho³⁺ [3], BaAl₂O₄:Ce³⁺,Dy³⁺ [4], or CaS:Eu²⁺,Tm³⁺ [5] play an important role as luminescent afterglow phosphors in applications such as traffic signs, emergency signs, safety clothes, glow-in-the-dark toys, emergency afterglow lighting, advertising, etc. The exceptionally high afterglow efficiency and the related commercial success of these

materials is to a large extent determined by the detailed charge (electrons and holes) trapping mechanism that has been the subject of many investigations the past years. Charge carrier trapping by (pairs of) lanthanide ions is determined by the location of the lanthanide (Ln) ground state (GS) and excited states relative to the valence bands (VB) and conduction bands (CB) of host materials. Empirical models have recently been developed that describe the systematic behavior of the energy of Ln^{2+} and Ln^{3+} ground states relative to the valence and conduction band [6, 7] and have provided new insight in how Ln ions as pairs can work together to efficiently store and release charges resulting in efficiently luminescence afterglow [8]. These models predict for example that Ce^{3+} is a stable hole-trap while certain other trivalent lanthanide act as stable electron traps. Ce^{3+} ions together with other Ln^{3+} co-doping ions can therefore act as efficient charge trapping couples. Optically excited Ce^{3+} ions can transfer an electron to the Ln^{3+} co-doping ions that can act as a stable electron traps. During heating or at room temperature the trapped electrons are transferred back to Ce generating Ce^{3+} luminescence. Detailed experimental data that are able to verify these charge trapping models are still scarce and scattered over different investigations of different doping ions in different host lattices [9, 10, 11, 12].

Here we present a detailed and systematic experimental investigation into the nature of electron traps and into the relation between trap depth and the type of Ln ion in two closely related host lattices YPO_4 and $LuPO_4$. Firstly, in section 3.1., the X-Ray excited emission properties of $LuPO_4$ and YPO_4 doubly doped with Ce^{3+} and Ln^{3+} ($Ln = Sm, Dy, Ho, Er, Tm$) are presented. Then in section 3.2., from the excitation spectra, the charge transfer energies E^{CT} (Ln^{3+}) are established that give the location of the Ln^{2+} ground state 4f energy levels with respect to the valence band. The same energy levels with respect to the conduction band are established in section 3.3. using thermoluminescence analysis techniques. Finally, in section 4. the results of the two methods are compared and interpreted with the help of the Dorenbos model.

2. Experimental

2.1. Sample Preparation

The $A_{0.994}Ce_{0.003}Ln_{0.003}PO_4$ ($A = Y, Lu$) powders were produced using $NH_4H_2PO_4$, A_2O_3 , CeF_3 and Ln_2O_3 as starting materials. The molar ratio of the starting mixture was: $NH_4H_2PO_4: A_2O_3: CeF_3: Ln_2O_3 = 1: 0.497: 0.003: 0.0015$. After crushing and mixing the reactants carefully the powder was pressed to a pellet, put in a Pt crucible and heated at first with a rate of $1^\circ C/min$ to $410^\circ C$ in a programmable furnace. It was kept at this temperature for 10 h and then cooled down to room temperature. After crushing and re-mixing the powder it was pressed again to a pellet, and heated for a second treatment with a heating rate of $5^\circ C/min$ up to $1450^\circ C$ for 10 h. The samples

Experimental

purity was checked by X-ray diffraction. YPO_4 and LuPO_4 have the tetragonal zircon structure with space group $I4_1/amd$ (No. 141). The metal atom is coordinated by 8 oxygen atoms forming a polyhedron with site symmetry D_{2d} . The phosphate group in each compound forms a distorted tetrahedron [13]. The differences between the two compounds in ionic radii, inter-atomic distances and lattice parameters are listed in Table 1.

Table 1. Characteristic parameters of YPO_4 and LuPO_4 ; r = effective ionic radius [14]; $d(R-O)$ ($R = A, P$) = average inter-atomic distance in polyhedra of the $A\text{PO}_4$ structures [13]; a, c = lattice parameters [13].

| $A\text{PO}_4$ | $r(A)$ [pm] | $\langle d(A-O) \rangle$ [pm] | $\langle d(P-O) \rangle$ [pm] | a [pm] | c [pm] |
|-----------------|----------------|----------------------------------|----------------------------------|-------------|-------------|
| YPO_4 | 101.9 | 233.7 | 154.3 | 688.2 | 601.8 |
| LuPO_4 | 97.7 | 230.3 | 153.4 | 679.2 | 595.4 |

2.2. Measurement Techniques

For VUV excitation measurements a water-cooled 150W deuterium lamp (model L1835, Hamamatsu) was used in combination with a vacuum monochromator (model VM 502, ARC) as an excitation source. The light emitted from the powders was detected by a PMT (model B2FV45/RFI, Electron Tubes Limited) combined with an appropriate filter. Excitation spectra were corrected for background and lamp spectrum (obtained with a calibrated SXUV-type Si-ultraviolet photodiode from IRD).

In the case of the X-ray excited emission studies the X-ray tube with a Cu-anode was operated at 35 kV accelerating voltage and 25 mA electrical current. The emission spectrum was recorded by the help of a vacuum monochromator (model VM 504, ARC) coupled with a PMT (EMI 9426).

The TL measurements were done with a RISØ system (model TL/OSL-DA-15), consisting of an automated TL/OSL reader incorporated into a 386-based PC, a turntable with 48 sample positions and a $^{90}\text{Sr}/^{90}\text{Y}$ beta source with a dose rate of 1mGy s^{-1} . Heating rates varied from 0.1 to 5 K/s. The emitted light of each individually heated sample was detected by a PMT (model 9235QA, Electron Tubes Limited) with a Hoya U340 filter in front of it, or a high-sensitivity fiber optic spectrometer (model QE65000, Ocean Optics) in case of the λT -contour plots. In the case of the λT -contour plots the samples were irradiated with an external ^{60}Co source with a dose rate of 4.06 kGy h^{-1} . All TL measurements were done in a nitrogen atmosphere.

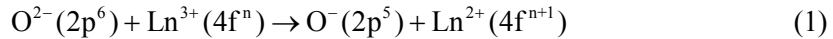
3. Results

3.1. X-Ray Excited Emission Spectra

In Figures 1 and 2 the X-ray excited emission spectra of YPO_4 , $\text{YPO}_4:\text{Ce}^{3+},\text{Ln}^{3+}$ and $\text{LuPO}_4:\text{Ce}^{3+},\text{Ln}^{3+}$ ($\text{Ln} = \text{Sm}, \text{Dy}, \text{Ho}, \text{Er}, \text{Tm}$) are shown with a resolution of 2 nm. All spectra of the double-doped compounds feature the known [15] $5d^1 \rightarrow 4f^1: {}^2F_{5/2}, {}^2F_{7/2}$ emission of Ce^{3+} at 336 nm and 360 nm for LuPO_4 , and at 333 nm and 356 nm for YPO_4 , respectively together with the second order bands due to the diffraction grating of the monochromator. Both the Ce^{3+} emission and the second order bands are indicated inside Figures 1 and 2 by dotted, vertical lines. The specific Ln^{3+} emission lines identified in each spectrum are specified in Table 2. It was reported earlier that Ho^{3+} does not show luminescence in YPO_4 [16]. In our measurements we still see very weak emission lines at 475 nm, 484 nm and 575 nm. The two former ones were assigned to the ${}^5F_3 \rightarrow {}^5I_8$ transition, whereas the 575 nm line is attributed to the ${}^5F_4 \rightarrow {}^5I_8$ transition despite its unusual low energy [17, 18]. No Ho^{3+} emission can be observed in LuPO_4 . The emission of Er^{3+} is very weak both in the YPO_4 and the LuPO_4 compounds.

3.2. VUV / UV Excitation Spectra

The VUV excitation spectra of YPO_4 , $\text{YPO}_4:\text{Ce}^{3+},\text{Ln}^{3+}$ and $\text{LuPO}_4:\text{Ce}^{3+},\text{Ln}^{3+}$ are presented in Figures 3 and 4. For each double doped sample two excitation spectra were recorded: One monitoring Ce^{3+} emission and one monitoring the emission of the Ln^{3+} co-dopant. The identified excitation bands are summarized in Table 3. The four Ce^{3+} 4f-5d transitions can be identified easiest and from there the 4f-5d transitions of all other Ln^{3+} dopants can be predicted [19]. These predictions were used in order to assign the 4f-5d excitation bands of the other Ln^{3+} dopant ions. Beside the 4f-5d excitation bands we observe broad bands that can be assigned to CT bands according to the following relation.



The energy of this transition, $E^{\text{CT}} (\text{Ln}^{3+})$, is an important parameter in the location of the Ln^{2+} 4f energy levels as it can be interpreted as the energy difference between the $\text{Ln}^{2+} (4f^{n+1})$ GS and the top of the VB [6]. Van Pieterse [16, 20, 21] and Nakazawa [22] have studied independently of each other $\text{YPO}_4:\text{Ln}^{3+}$ and have assigned the Ln^{3+} 4f-5d and Ln^{3+} CT transitions. Their assignments are in agreement with ours (see Table 3).

Results

The excitation spectra contain as well a broad-band feature at around 150 nm (open black circles). In addition, the excitation spectrum of pure YPO_4 (top panel of Figure 3) shows a strong drop in excitation intensity at about the same wavelength. In line with the observations of Nakazawa *et al.* [22] we assign this transition to excitation of individual PO_4^{3-} groups.

When looking carefully at the excitation spectra monitoring Ln^{3+} emission it can be seen that the top of the band which was identified as the lowest PO_4^{3-} group transition energy, $E(\text{PO}_4^{3-}, \text{Ln}^{3+})$, depends on the Ln^{3+} size. From Figure 5 two observations can be made: (i) $E(\text{PO}_4^{3-}, \text{Ln}^{3+})$ is larger in $\text{LuPO}_4:\text{Ce}^{3+}, \text{Ln}^{3+}$ than in $\text{YPO}_4:\text{Ce}^{3+}, \text{Ln}^{3+}$, and (ii) $E(\text{PO}_4^{3-}, \text{Ln}^{3+})$ increases linearly with increasing Ln^{3+} ionic radius. That the host excitation energy can, in principle, be affected by the activator is understandable when we bring to mind that we look at the emission of the activator, i.e., we single out in the excitation spectra these PO_4^{3-} ions which are close enough to the activators in order to transfer the excitation energy ($\text{PO}_4^{3-} \rightarrow \text{Ln}^{3+}$). Let us discuss the two problems one by one. (i) We start with the observation that $E(\text{PO}_4^{3-}, \text{RE}^{3+})$ is larger for LuPO_4 than for YPO_4 . In the xenotime structure of REPO_4 ($\text{RE} = \text{Y}, \text{Lu}$), oxygen atoms coordinate to two RE and one P atom [23]. This means that not only the P^{5+} ions but also the RE^{3+} ions have, due to their size and their Coulomb potential, an effect on the stabilization of the valence electrons of the oxygen ions which are involved in the PO_4^{3-} group transition: The smaller the RE^{3+} ions and the higher their charge, the higher the binding energy of the $\text{RE}^{3+} - \text{O}^{2-}$ system will be and the more energy will be needed in order to remove an electron from these oxygen ions. This explains why $E(\text{PO}_4^{3-}, \text{RE}^{3+})$ is in general larger in $\text{LuPO}_4:\text{Ln}^{3+}$ than in $\text{YPO}_4:\text{Ln}^{3+}$. (ii) The other observation might look puzzling in the light of the previous explanation: The larger the co-dopant ion and the lesser its charge, the larger $E(\text{PO}_4^{3-}, \text{RE}^{3+})$ when monitoring the emission of the co-dopant. If the activator ion is larger than the host-lattice cation which it replaces (Y or Lu), the environment of the activator will expand and affect neighboring PO_4^{3-} ions. In fact, here only the activators environment changes while the specific inter-atomic arrangement of the compound remains the same at large. The increased distance between the tetrahedral PO_4 groups and the activator apparently affects the energy levels of the PO_4^{3-} ions otherwise and results in larger stabilization of the oxygen ions.

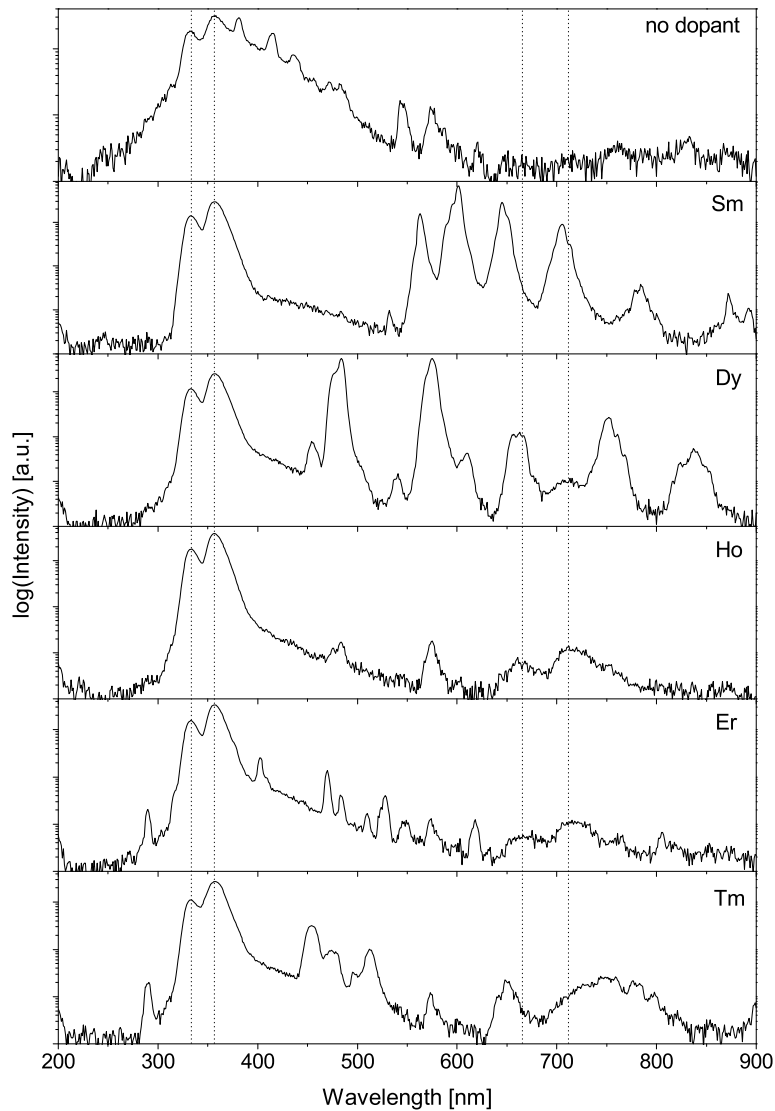


Fig. 1. Room temperature X-ray excited emission spectra of YPO_4 and $\text{YPO}_4:\text{Ce}^{3+},\text{Ln}^{3+}$; type of Ln is specified inside each panel; the dotted vertical lines indicate both the Ce^{3+} emission (left hand) and the second order bands of this emission (right hand); note that the spectra are displayed on a logarithmic scale.

Results

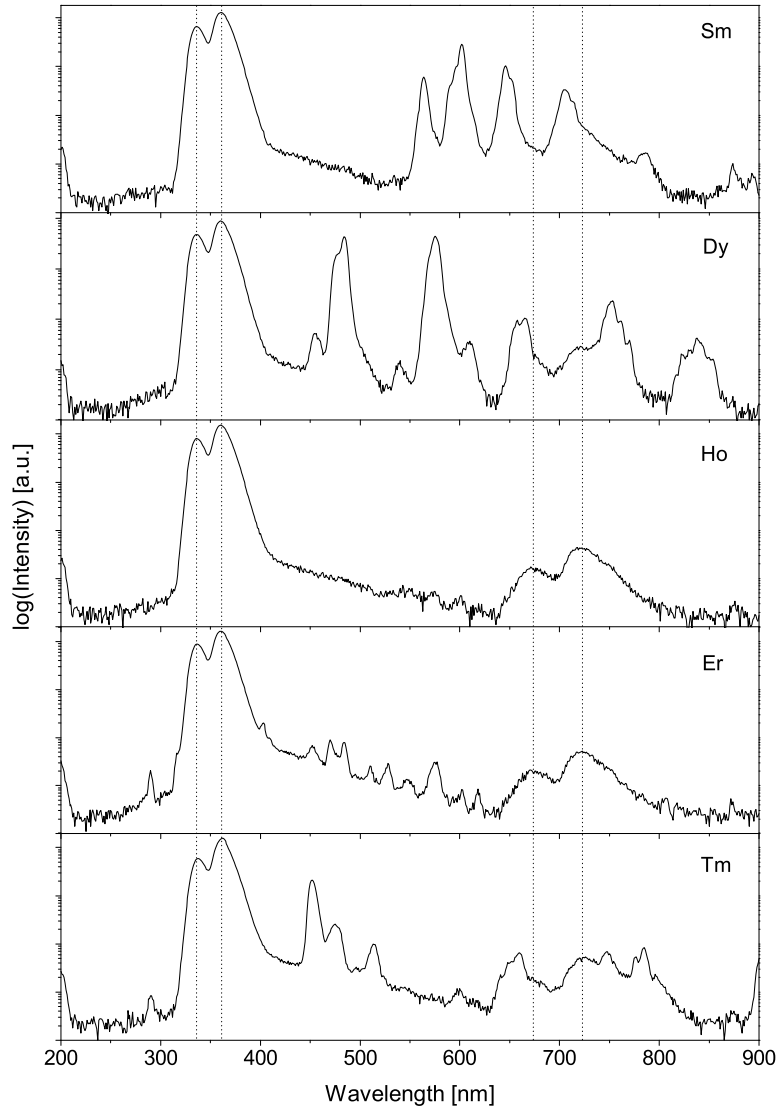


Fig. 2. Room temperature X-ray excited emission spectra of $\text{LuPO}_4:\text{Ce}^{3+},\text{Ln}^{3+}$; type of Ln is specified inside each panel; the dotted vertical lines indicate both the Ce^{3+} emission (left hand) and the second order bands of this emission (right hand); note that the spectra are displayed on a logarithmic scale.

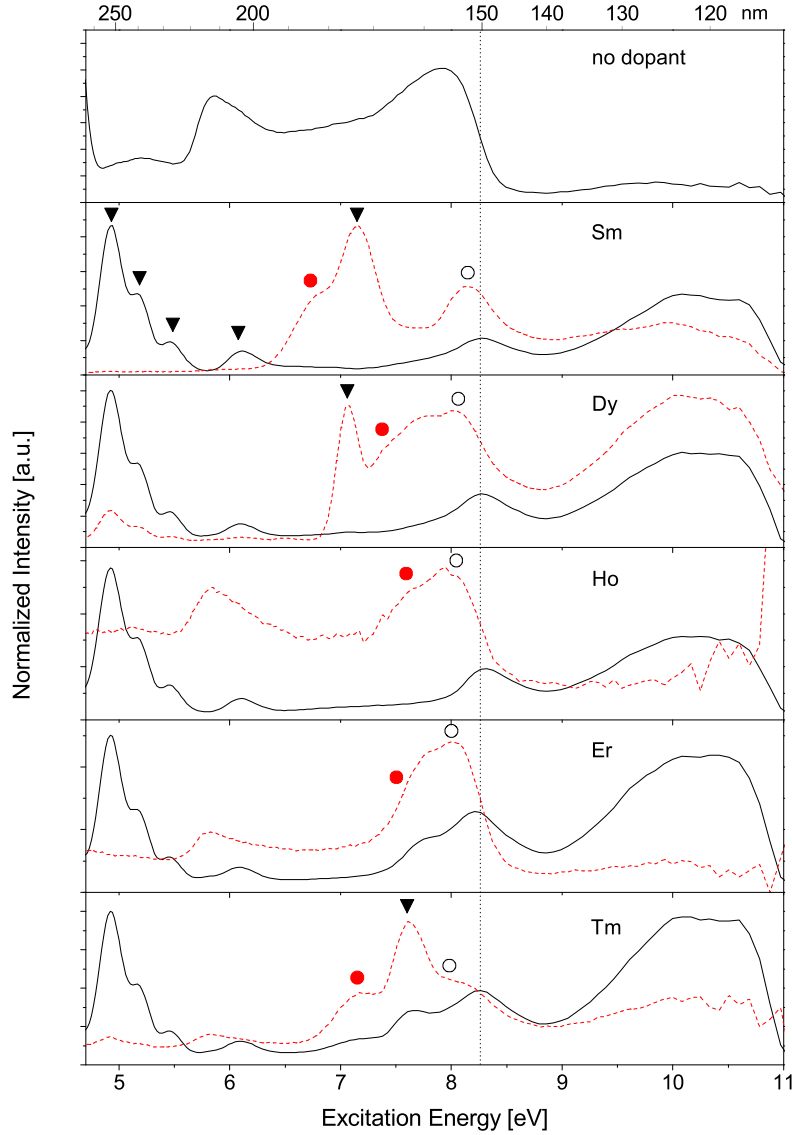


Fig. 3. Room temperature VUV excitation spectra of YPO_4 and $\text{YPO}_4:\text{Ce}^{3+},\text{Ln}^{3+}$ monitoring Ce^{3+} emission (solid line) and Ln^{3+} emission (dashed line); in the case of pure YPO_4 the broad band emission around 350 nm has been monitored; type of Ln is specified inside each panel; inside the panels also the band positions of 4f-5d (black triangle) transitions, $\text{O}^{2-} \rightarrow \text{Ln}^{3+}$ CT transitions (filled circles) and the lowest PO_4^{3-} group transition (open circles) are shown. The vertical dotted line at about 8.27 eV indicates the lowest PO_4^{3-} group transition monitoring Ce^{3+} emission.

Results

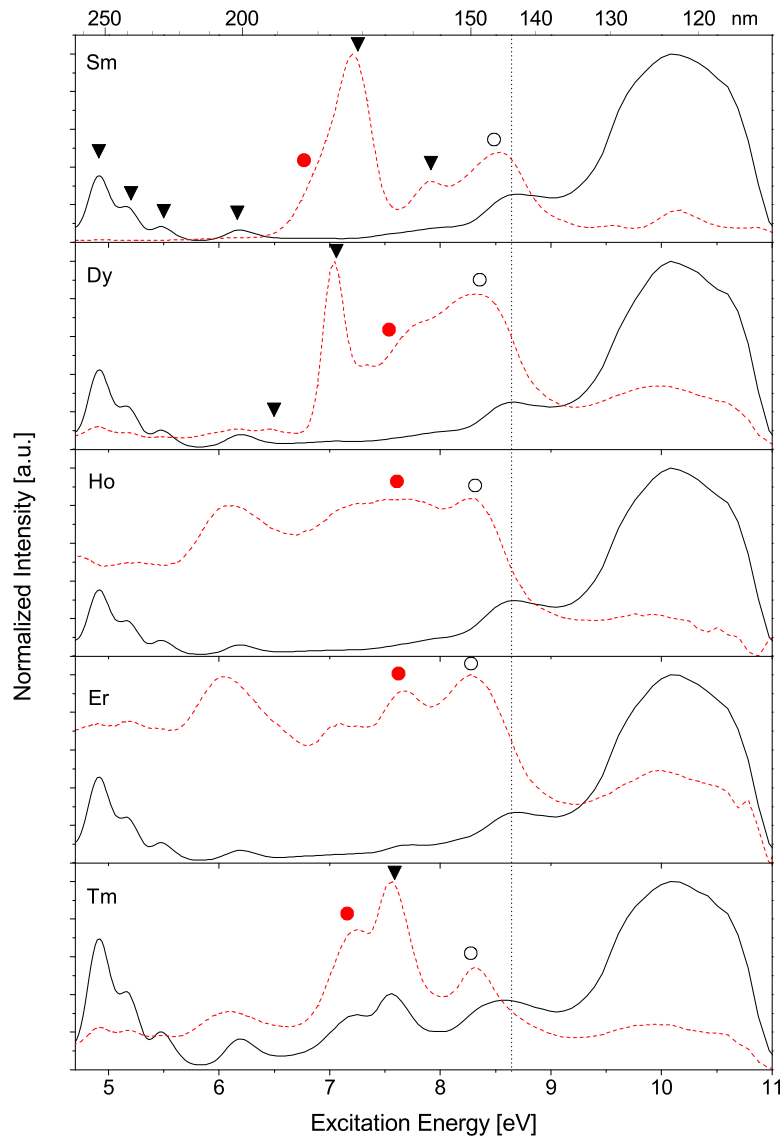


Fig. 4. Room temperature VUV excitation spectra of $\text{LuPO}_4:\text{Ce}^{3+}, \text{Ln}^{3+}$ monitoring Ce^{3+} emission (solid line) and Ln^{3+} emission (dashed line); type of Ln is specified inside each panel; inside the panels also the band positions of 4f-5d (black triangle) transitions, $\text{O}^{2-} \rightarrow \text{Ln}^{3+}$ CT transitions (filled circles) and the lowest PO_4^{3-} group transition (open circles) are shown. The vertical dotted line at about 8.6 eV indicates the lowest PO_4^{3-} group transition monitoring Ce^{3+} emission.

Chapter 4. Controlled Electron and Hole Trapping in $\text{YPO}_4:\text{Ce}^{3+}, \text{Ln}^{3+}$ and $\text{LuPO}_4:\text{Ce}^{3+}, \text{Ln}^{3+}$

Table 2. 5d-4f and 4f-4f transitions identified in the X-ray excited emission spectra shown in Figures 1 and 2.

| Ln | Transition | Wavelength [nm] | |
|----|--|---|--|
| | | $\text{YPO}_4:\text{Ce}^{3+}, \text{Ln}^{3+}$ | $\text{LuPO}_4:\text{Ce}^{3+}, \text{Ln}^{3+}$ |
| Ce | $5d^1 \rightarrow 4f^1: {}^2F_{5/2}$ | 333 | 336 |
| | $5d^1 \rightarrow 4f^1: {}^2F_{7/2}$ | 356 | 360 |
| Sm | $4f^5: {}^4G_{5/2} \rightarrow {}^6H_{5/2}$ | 563 | 564 |
| | ${}^4G_{5/2} \rightarrow {}^6H_{7/2}$ | 586 – 611 | 586 – 611 |
| | ${}^4G_{5/2} \rightarrow {}^6H_{9/2}$ | 639 – 655 | 639 – 663 |
| | ${}^4G_{5/2} \rightarrow {}^6H_{11/2}$ | 694 – 722 | 694 – 722 |
| | ${}^4G_{5/2} \rightarrow {}^6H_{13/2}$ | 775 – 792 | 780 – 791 |
| | ${}^4G_{5/2} \rightarrow {}^6H_{15/2} + {}^6F_{1/2, 3/2}$ | 871 – 893 | 873 – 893 |
| Dy | $4f^9: {}^4F_{9/2} \rightarrow {}^6H_{15/2}$ | 454, 476, 484 | 454, 476, 484 |
| | ${}^4F_{9/2} \rightarrow {}^6H_{13/2}$ | 541, 575, 610 | 540, 575, 610 |
| | ${}^4F_{9/2} \rightarrow {}^6H_{11/2}$ | 646 – 676 | 646 – 676 |
| | ${}^4F_{9/2} \rightarrow {}^6H_{9/2} + {}^6F_{11/2}$ | 735 – 769 | 738 – 769 |
| | ${}^4F_{9/2} \rightarrow {}^6H_{7/2} + {}^6F_{9/2}$ | 818 – 855 | 818 – 858 |
| Ho | $4f^{10}: {}^5F_3 \rightarrow {}^5I_8$ | 475, 484 | no emission observed |
| | ${}^5F_4 \rightarrow {}^5I_8$ | 575 | |
| Er | $4f^{11}: {}^2D_{5/2}, {}^2D_{7/2} \rightarrow {}^4I_{15/2}$ | 290 | 290 |
| | ${}^2K_{3/2} \rightarrow {}^4I_{15/2}$ | 316 | 316 |
| | ${}^2H_{9/2} \rightarrow {}^4I_{15/2}$ | 402, 409 | 403, 409 |
| | ${}^4F_{5/2} \rightarrow {}^4I_{15/2}$ | no emission observed | 448 – 456 |
| | ${}^4F_{7/2} \rightarrow {}^4I_{15/2}$ | 470, 483 | 470, 484 |
| | ${}^4G_{11/2} \rightarrow {}^4I_{13/2}$ | 510, 512 | 510 – 513 |
| | ${}^2H(2)_{11/2} \rightarrow {}^4I_{15/2}$ | 521 – 528 | 524 – 531 |
| | ${}^4S_{3/2} \rightarrow {}^4I_{15/2}$ | 543 – 553 | 544 – 553 |
| | ${}^2H_{9/2} \rightarrow {}^4I_{13/2}$ | 569 – 580 | 569 – 575 |
| Tm | $4f^{12}: {}^1I_6 \rightarrow {}^3H_6$ | 291 | 291 |
| | ${}^1D_2 \rightarrow {}^3F_4$ | 454 | 452 |
| | ${}^1G_4 \rightarrow {}^3H_6$ | 474 | 475 |
| | ${}^1D_2 \rightarrow {}^3H_5$ | 495, 512 | 496, 513 |
| | ${}^1G_4 \rightarrow {}^3F_4 + {}^1D_2 \rightarrow {}^3H_4$ | 641, 648, 659 | 641, 648, 660 |
| | ${}^1G_4 \rightarrow {}^3H_5 + {}^1D_2 \rightarrow {}^3F_3$ | 759 – 798 | 748 – 796 |

Results

Table 3. 4f-5d and O²⁻ → Ln³⁺ CT energies identified in the VUV excitation spectra shown in Figures 3 and 4.

| Ln | Transition | Energy (eV) | |
|----|---------------------------------------|--|---|
| | | YPO ₄ :Ce ³⁺ ,Ln ³⁺ | LuPO ₄ :Ce ³⁺ ,Ln ³⁺ |
| Ce | 4f → 5d ¹ | 3.9, 4.93, 5.19, 5.46, 6.1 | 3.9, 4.92, 5.19, 5.48, 6.2 |
| Sm | 4f → 5d ¹ | 7.15 | 7.24, 7.9 |
| | O ²⁻ → Sm ³⁺ CT | 6.75 | 7.0 |
| Dy | 4f → 5d ¹ | 6.49 (s.f.), 7.06 (s.a.) | 6.45 (s.f.), 7.05 (s.a.) |
| | O ²⁻ → Dy ³⁺ CT | 7.34 – 7.74 | 7.57 – 7.84 |
| Ho | O ²⁻ → Ho ³⁺ CT | 7.6 | 7.2 – 7.78 |
| Er | O ²⁻ → Er ³⁺ CT | 7.32 – 7.76 | 7.1 – 7.65 |
| Tm | 4f → 5d ¹ | 7.6 | 7.56 |
| | O ²⁻ → Tm ³⁺ CT | 7.05 – 7.24 | 7.07 – 7.24 |

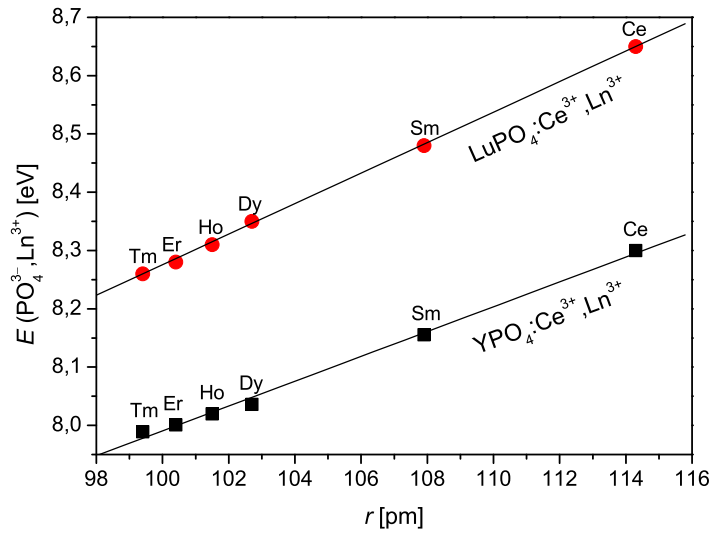


Fig. 5. Lowest PO₄³⁻ group transition energy, $E(\text{PO}_4^{3-}, \text{Ln}^{3+})$, in YPO₄:Ce³⁺,Ln³⁺ and LuPO₄:Ce³⁺,Ln³⁺ as a function of the effective atomic radius, r , of the Ln³⁺ co-dopant and Ce³⁺; $E(\text{PO}_4^{3-}, \text{Ln}^{3+})$ is taken from the VUV excitation spectra presented in Figures 3 and 4 monitoring Ce, Sm, Dy, Ho, Er, or Tm emission; type of Ln³⁺ emission is specified inside the Figure.

3.3. Thermoluminescence Studies

Figure 6 displays the wavelength-resolved TL glow curves of $\text{LuPO}_4:\text{Ce}^{3+},\text{Ln}^{3+}$ in a two-dimensional λT -contour plot. Such a type of measurement is able to identify the nature of the emission during the TL process and can be used to select proper optical filters to selectively monitor emission from specific ions like Ce^{3+} . All contour plots, except the ones for $\text{LuPO}_4:\text{Ce}^{3+},\text{Ho}^{3+}$ and maybe $\text{LuPO}_4:\text{Ce}^{3+},\text{Er}^{3+}$, show the typical 5d-4f emission of Ce^{3+} at a specific temperature that is characteristic for each Ln dopant, even though it is not very intense. For $\text{LuPO}_4:\text{Ce}^{3+},\text{Sm}^{3+}$ and $\text{LuPO}_4:\text{Ce}^{3+},\text{Dy}^{3+}$ also emission from the Ln ion can be observed. These results are similar to the ones found in $\text{YPO}_4:\text{Ce}^{3+},\text{Ln}^{3+}$ [8]. In contrast to $\text{YPO}_4:\text{Ce}^{3+},\text{Ln}^{3+}$, however, $\text{LuPO}_4:\text{Ce}^{3+},\text{Ln}^{3+}$ (Ln = Sm, Ho, Er) show also broad band emission around 450 nm which is probably host-related.

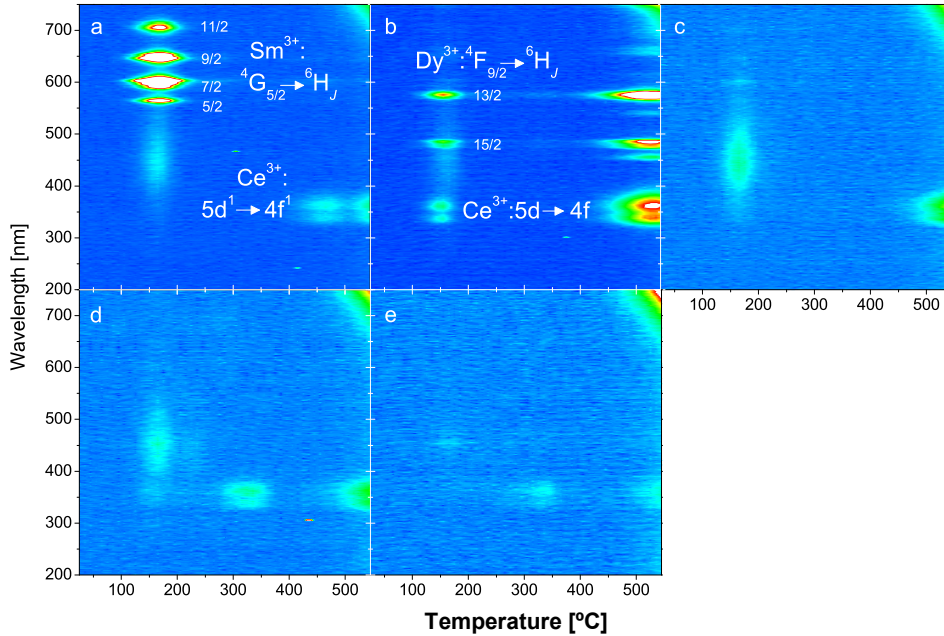


Fig. 6. λT -contour plots of $\text{LuPO}_4:\text{Ce}^{3+},\text{Sm}^{3+}$ (a), $\text{LuPO}_4:\text{Ce}^{3+},\text{Dy}^{3+}$ (b), $\text{LuPO}_4:\text{Ce}^{3+},\text{Ho}^{3+}$ (c), $\text{LuPO}_4:\text{Ce}^{3+},\text{Er}^{3+}$ (d), $\text{LuPO}_4:\text{Ce}^{3+},\text{Tm}^{3+}$ (e), after gamma irradiation with a dose of 4.3 kGy from a ^{60}Co source; heating rate = 5 K/s.

Results

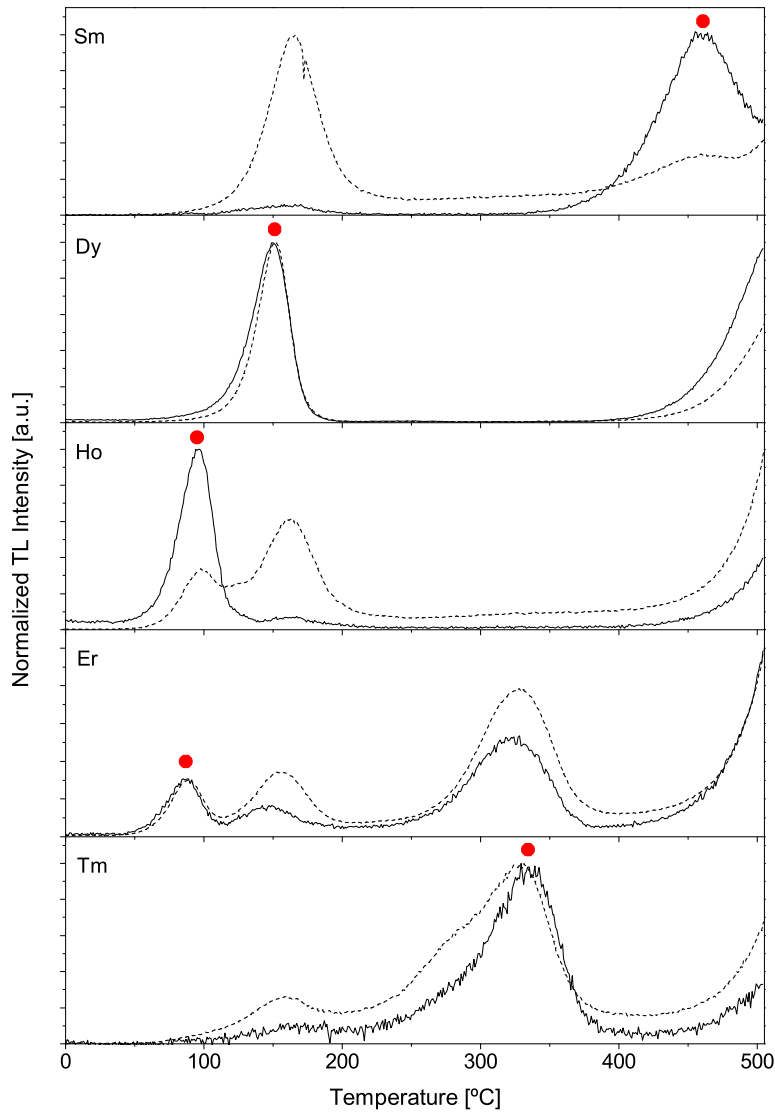


Fig. 7. Normalized TL glow curves of $\text{LuPO}_4:\text{Ce}^{3+},\text{Ln}^{3+}$ monitoring Ce^{3+} emission after 600 mGy beta irradiation (solid line) and 30 min irradiation with deuterium lamp in ambient gas atmosphere (dashed line); type of Ln is specified inside each panel; the filled circle shown in each panel indicates the glow peak due to thermally assisted $\text{Ln}^{2+} \rightarrow \text{Ce}^{4+}$ CT.

The TL glow curves of $LuPO_4:Ce^{3+},Ln^{3+}$ both after beta irradiation and after illumination with light are shown in Figure 7. They are similar to the glow curves of $YPO_4:Ce^{3+},Ln^{3+}$ presented in [8]. The Ln^{3+} -related glow peaks which were observed in $YPO_4:Ce^{3+},Ln^{3+}$ [8] show up as well in $LuPO_4:Ce^{3+},Ln^{3+}$ at about the same temperatures. Beside these peaks additional peaks can be noticed in all glow curves with one common peak with maximum TL intensity at about 161 °C which is assumed to be host-related. In the case of $LuPO_4:Ce^{3+},Tm^{3+}$ the Tm^{3+} -related TL peak appears at similar temperatures as other host-related peaks which are also present in $LuPO_4:Ce^{3+},Er^{3+}$. In view of the detailed glow curve analysis reported for $YPO_4:Ce^{3+},Tm^{3+}$ [8] we tentatively assigned the maximum of the broad band at 340 C to a Tm^{3+} -related glow peak. Figure 6 shows that the Dy-related glow peak in $LuPO_4:Ce^{3+},Dy^{3+}$ shows the highest TL intensity among all Ln-related glow peaks. This fact has also been observed in $YPO_4:Ce^{3+},Ln^{3+}$ [8] and $NaLaF_4:Ce^{3+},Ln^{3+}$ [24]. Following Bos *et al.* [8] we have determined the activation energy, E_A , from each Ln-related glow peak shown in Figure 7 with three different methods assuming in all cases first-order kinetics, i.e., neglecting re-trapping during heating.

(i) First we have used a simple formula of the form [25]

$$E_A = 2.52 \cdot k_B T_m^2 / \text{FWHM} - 2k_B T_m, \quad (2)$$

where k_B (eV/K) is the Boltzmann constant, T_m (K) the temperature at which the glow peak has maximum intensity, and FWHM means the full width at half maximum of the glow peak.

(ii) The second method made use of the dependence of T_m on the heating rate, β (K/s). In first-order kinetics the condition for maximum TL intensity can be written as an Arrhenius equation [25],

$$\ln(T_m^2 / \beta) = E_A / k_B T_m + \ln(E_A / k_B s), \quad (3)$$

in which s (s^{-1}) indicates the frequency factor. Plotting equation (3) against $1/k_B T_m$ (heating rate plots) results in a straight line with slope E_A and intercept $\ln(E_A / k_B s)$. The heating rate plots for all $LuPO_4:Ce^{3+},Ln^{3+}$ samples are shown in Figure 8.

(iii) Finally, as third method, we have analyzed each glow peak by the help of a program called GlowFit [26]. An example of such a fit is given in Figure 9. The activation energies determined with these three methods are displayed together with the predicted values given by the Dorenbos model in Table 4.

Results

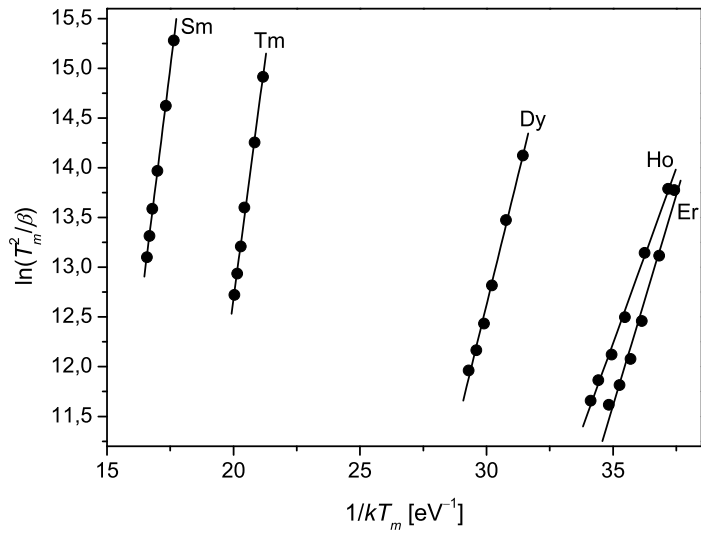


Fig. 8. Heating rate plots of the $\text{LuPO}_4:\text{Ce}^{3+}, \text{Ln}^{3+}$ glow curves after beta irradiation; type of Ln is specified inside the figure.

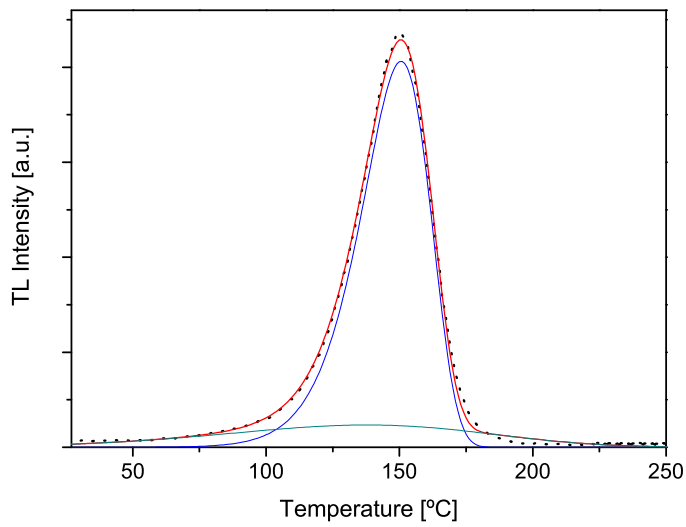


Fig. 9. Glow curve analysis by fitting with two first-order glow peaks using the glow curve of $\text{LuPO}_4:\text{Ce}^{3+}, \text{Dy}^{3+}$ after beta irradiation that is shown in Figure 6.

Table 4. Mean values of the activation energies in $LuPO_4:Ce^{3+},Ln^{3+}$ derived by three different methods from the TL glow curves and activation energies derived via $E_{VC} - E^{CT}(Ln^{3+})$.

| Co-dopant | Simple formula | Heating rate method | Glow curve analysis | $E_{VC} - E^{CT}(Ln^{3+})$ |
|-----------|-----------------|---------------------|---------------------|----------------------------|
| Sm | 1.37 ± 0.05 | 2.04 ± 0.02 | 1.72 ± 0.06 | 1.6 |
| Dy | 0.93 ± 0.05 | 1.05 ± 0.06 | 1.02 ± 0.09 | 1.03 |
| Ho | 0.77 ± 0.04 | 0.70 ± 0.06 | 0.81 ± 0.1 | 0,82 |
| Er | 0.74 ± 0.03 | 0.85 ± 0.1 | 0.81 ± 0.07 | 0,95 |
| Tm | 1.20 ± 0.13 | 1.93 ± 0.06 | 1.32 ± 0.17 | 1,53 |

The values given in columns 2 and 4 of Table 4 are the arithmetic mean of all measured glow curves with different heating rates together with the standard deviation. The values in column 3 of Table 4 represent the slope and the standard deviation of the least-squares fit of the straight line to the single data points. Each data point was taken from one glow curve with a specific heating rate.

4. Discussion

One main objective of this section is to derive energy level diagrams of both $YPO_4:Ln^{3+}$ and $LuPO_4:Ln^{3+}$ in which we place the Ln^{2+} ground states of all the Ln doping ions with respect to the conduction and valence bands of the YPO_4 and $LuPO_4$ hosts. Firstly, we will derive the band-gap energy from the luminescence excitation spectra (section 4.1.). Secondly, we place the Ln^{2+} ground state levels with respect to the top of the valence band using the observed CT transitions (section 4.2.). Thirdly, we place the Ln^{2+} ground state levels relative to the conduction band edge on the bases of the TL data (section 4.3.). Finally, we present and discuss the resulting energy level diagram as presented in Figure 10 (section 4.4.).

4.1. Estimation of Exciton Creation And Band Gap Energy

The first allowed PO_4^{3-} group transition energy, $E(PO_4^{3-}, RE^{3+})$, can be considered as the minimum energy needed to create a bound exciton. The abbreviation RE (rare earth = lanthanides + Y and Sc) has been included in the definition of this energy as the rare earth ion of the host as well as the Ln dopant has an effect on it (see Figure 5). The exciton creation energy is somewhat smaller than the band gap energy, E_{VC} , i.e., the minimum energy needed to make a free electron and a free hole. Furthermore we consider E_{VC} the energy between the top of the valence band and the bottom of the conduction band (band gap). We have chosen to use the following simple relation between exciton energy and band gap energy:

Discussion

$$E_{\text{VC}} \cong 1.05 \cdot E(\text{PO}_4^{3-}, \text{RE}^{3+}) \quad (4)$$

With equation (4) we therefore assume the difference between $E(\text{PO}_4^{3-}, \text{RE}^{3+})$ and E_{VC} to be about 2% smaller than stated by Dorenbos for oxide compounds [7]. This smaller distance has been chosen in order to bring the energetic locations of the $\text{Ln}^{2+} : 4f^{n+1}$ ground states set by the activation energies of the Ln-related TL glow peaks and the Ln^{3+} CT energies into an optimal agreement.

From the excitation spectrum of pure YPO_4 (see Figure 3), $E(\text{PO}_4^{3-}, \text{Y}^{3+})$ was identified to be 8 eV (155 nm). This is in agreement with the value that would have been expected based on the linear relation between $E(\text{PO}_4^{3-}, \text{RE}^{3+})$ and $r(\text{RE}^{3+})$ which is displayed in Figure 5, taking $r(\text{Y}^{3+}) = 101.9$ pm [14]. In view of this linear relation the corresponding transition energy in LuPO_4 , $E(\text{PO}_4^{3-}, \text{Lu}^{3+})$, was estimated to be about 8.22 eV (151 nm), for $r(\text{Lu}^{3+}) = 97.7$ pm [14]. Nakazawa specifies this energy with 8.55 eV (145 nm) [22]. Using formula (4) it is now possible to estimate the band gap energies of YPO_4 and LuPO_4 at 8.4 and 8.63 eV respectively. These values were used in Figure 10.

4.2. Charge Transfer Transitions

Figure 10 shows the two energy level diagrams of $\text{YPO}_4:\text{Ce}^{3+}, \text{Ln}^{3+}$ and $\text{LuPO}_4:\text{Ce}^{3+}, \text{Ln}^{3+}$. It will be discussed in the following step-by-step how they have been constructed.

$\text{O}^{2-} \rightarrow \text{Ln}^{3+}$ charge transfer transitions (see equation 1) give direct information about the energy of the Ln^{2+} ground states relative to the top of the VB [6]. Provided the energy difference between the VB and CB band is known (see section 4.1.) it is possible to position the Ln^{2+} GS energies relative to the CB as well. The filled circles in Figures 3, 4 and 10 indicate the $\text{O}^{2-} \rightarrow \text{Ln}^{3+}$ CT transitions which are summarized in Table 3. These CT transitions give approximately the $\text{Ln}^{2+} : 4f^{n+1}$ ground states relative to the top of the VB [6]. The open circles in Figure 10 are predictions by the Dorenbos model which claims a constant, i.e. host-independent energy difference between two neighboring 4f ground states inside the energy level diagram both for the divalent and the trivalent Ln dopant ions. The experimentally determined CT energies combined with the Dorenbos model allow one to predict immediately that Sm^{3+} , Dy^{3+} , Ho^{3+} , Er^{3+} and Tm^{3+} are stable electron traps in these phosphate hosts as their $\text{Ln}^{2+} 4f$ GS is located below the bottom of the CB. In addition the expected trap depths can be derived. In section 4.4. we will compare and discuss the electron trap depth with those obtained from TL measurements. For Ce^{3+} the situation is not as clear as it might appear. Although the $\text{Ce}^{2+} : 4f^2$ GS is energetically located inside the CB and, hence, can not trap an electron, the 5d levels of Ce^{2+} could be located below the bottom of the CB. In that case Ce^{3+} could still trap an electron. We can demonstrate with few

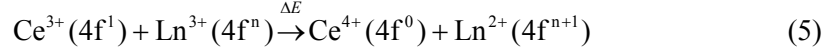
thoughts that this is not the case: Both in $\text{YPO}_4:\text{Ce}^{3+}$ and in $\text{LuPO}_4:\text{Ce}^{3+}$ the lowest Ce^{3+} 4f-5d transition occurs at about $30,800\text{ cm}^{-1}$ (325 nm) [15, 20]. For the free Ce^{3+} ion against it the lowest 4f-5d transition was found to be at about 201 nm [28]. That means that the crystal field depression or redshift for the trivalent lanthanides, $D(A, \text{Ln}^{3+})$, i.e. the energy difference between the Ce^{3+} 4f-5d transition energy of the free ion and the one of Ce^{3+} doped in a compound A , is approximately 2.35 eV in YPO_4 , LuPO_4 . From this value we can calculate the redshift for the divalent Ln ions, $D(A, \text{Ln}^{2+})$, in these two compounds to be about 1.271 eV [29]. Considering that the lowest 4f-5d transition in free Ce^{2+} is at about 2830 cm^{-1} (0.351 eV) [30] we can say that the lowest 5d level of Ce^{2+} is located approximately 0.92 eV below the 4f GS of Ce^{2+} . Based on the energy level diagrams shown in Figure 10 and the estimation of the CB bottom given by equation (4) this would place the lowest 5d level of Ce^{2+} inside the CB. In that case Ce^{3+} could not be an electron-trap.

It is possible to estimate the location of the Ln^{3+} ground states from the position of the Ln^{2+} ground states. It has been shown that in wide band gap compounds the energy difference between the $4f^6$ GS energy of Eu^{3+} and the $4f^7$ GS energy of Eu^{2+} is always between 6.6 and 7.3 eV [6, 30]. In Figure 10 we have used a value of 6.6 eV for the $\text{Eu}^{3+}/\text{Eu}^{2+}$ energy difference to place the Ln^{3+} GS curve with respect to the Ln^{2+} GS curve. This clearly shows that the Ce^{3+} GS is energetically located inside the band gap and hence Ce^{3+} can act as a hole-trap. The positions of the $\text{Ln}^{3+}:4f$ ground states are used in the next section to explain the observed charge trapping phenomena.

4.3. Thermoluminescence Activation Energies

Our choice to study LuPO_4 doubly doped with Ce^{3+} and a second Ln^{3+} co-dopant ion was motivated by a previous study on YPO_4 also doubly doped with Ce^{3+} and a second Ln^{3+} ion [8]. From that study it was concluded that after high energy irradiation, the Ce^{3+} dopant ion gives off an electron. Conduction band electrons on the other hand can be trapped by the Ln^{3+} co-dopant that are stable electron-traps. We have shown in Section 3.3. that each glow curve (see Figure 7) has Ln-related glow peaks. This means that the Ln co-dopants must act as charge-traps. We have also shown in section 4.2. that the Ln-co-doping ions are stable electron-traps. In addition to that, it was shown in Figure 6 that the Ln-related glow peaks are mainly causing emission from Ce^{3+} that in addition can only act as a hole-trap as demonstrated in the previous section. We have therefore strong indications that the charge trapping mechanism in LuPO_4 is the same as in YPO_4 . During heating (from room temperature up to 500 °C) the trapped electron is released from the $\text{Ln}^{2+}:4f^{n+1}$ GS and recombines via the CB with Ce^{4+} . As a result of this recombination Ce^{3+} emission can be observed. Thus, in these cases where the Ln-related glow peak consists mainly (or partly in $\text{LuPO}_4:\text{Ce}^{3+},\text{Dy}^{3+}$) of Ce^{3+} emission, the charge storing mechanism can be expressed as follows.

Discussion



ΔE symbolizes the energy introduced into the compound in form of high energy radiation. The charge trapping mechanism expressed in equation (5) predicts that identical TL-glow curves are expected when electrons from Ce^{3+} are directly excited into the CB and are successively trapped by the Ln^{3+} co-dopant ions. This is indeed confirmed by the TL glow curves obtained after illumination with UV light (see Figure 7). The energy which is needed to ionize Ce^{3+} in LuPO_4 is lower than the band gap energy, $E(\text{PO}_4^{3-}, \text{Ln}^{3+})$, and can be reached by UV light. As a light source a deuterium lamp was used and the experiment was carried out in ambient air in order to ensure that the high energy radiation able to excite across the band gap (about 150 nm) was filtered out. Since the TL emission after UV illumination is again from Ce^{3+} and the TL glow curves look very similar to the ones obtained after beta irradiation, the mechanism expressed by equation (5) is confirmed. The activation energy that is needed in order to release the electron from the Ln^{2+} ground state was derived from each of the Ln-related glow peaks presented in the experimental section (see Table 4). The activation energies provide a second means to locate the Ln^{2+} ground states relative to the CB and by using the band gap energy also relative to the VB. In Figure 10 we have plotted the $\text{Ln}^{2+} : 4f^{n+1}$ ground states relative to the top of the VB and the bottom of the CB as horizontal bars.

Finally, we discuss the origin of the TL from Dy^{3+} and Sm^{3+} in $\text{LuPO}_4:\text{Ce}^{3+}, \text{Dy}^{3+}$ and $\text{LuPO}_4:\text{Ce}^{3+}, \text{Sm}^{3+}$. In $\text{LuPO}_4:\text{Ce}^{3+}, \text{Dy}^{3+}$ the Ln-related glow peak not only consists of emission from Ce^{3+} but also from Dy^{3+} , and $\text{LuPO}_4:\text{Ce}^{3+}, \text{Sm}^{3+}$ shows Sm^{3+} emission at lower temperatures than the Sm-related glow peak. The fact that we observe Dy^{3+} and Sm^{3+} emission implies that besides Ce^{3+} also these two ions can act as recombination centers. In $\text{LuPO}_4:\text{Ce}^{3+}, \text{Dy}^{3+}$ the Dy^{3+} ion can act both as hole- and electron-trap as its $\text{Dy}^{3+} : ^6\text{H}_{15/2}$ as well as the $\text{Dy}^{2+} : ^6\text{I}_8$ ground states are inside the forbidden band gap (see Figure 10). Thus, the recombination may occur in principle either via an electron release or via a release of a hole. We have discussed in another study on $\text{NaLaF}_4:\text{Ln}^{3+}$ [24] the possibility of the formation of a V_{kA} -centre that might be stabilized by a host or a Ln impurity. Such a V_{kA} -centre can be freed thermally and can transfer the hole via a hopping mechanism to the Ln^{2+} ion producing Ln^{3+} emission. This mechanism could explain the situation in $\text{LuPO}_4:\text{Ce}^{3+}, \text{Ln}^{3+}$ (Ln = Sm, Dy). But as the Dy^{3+} and Ce^{3+} emission is found at the same temperature in the case of $\text{LuPO}_4:\text{Ce}^{3+}, \text{Dy}^{3+}$, both processes could take place at the same time only when the Dy-trapped electron and the Dy-trapped hole are characterized by approximately the same activation energies.

4.4. Dependence of Ln^{2+} Level Location on Experimental Method

From Figure 10 it can be concluded that the location of the Ln^{2+} ground states relative to the CB depends on the experimental method used, that is TL activation or CT energies. Three possible explanations for this behavior are given and discussed below.

First of all, it can be seen that the activation energies which are derived by the three different TL-methods explained in Section 3.3. for one glow peak are not the same. In the case of Sm for instance, the activation energy derived with the simple formula is 0.67 eV lower in energy than the one derived with the heating rate method. For Dy, Ho and Er, however, the differences are relatively small. In general it is assumed that the activation energies derived from the heating rate plots give the most reliable values.

Secondly, it is important to note that the Ln^{2+} GS energy as determined from TL measurements relative to the VB depends on the band gap energy, provided that equation (5) holds and that the charge carrier recombination happens via the CB. If, for example, the band gap derived by us in section 4.1., would be 0.1 eV larger, than this would increase the Ln^{2+} GS energies relative to the VB as well by 0.1 eV.

Thirdly, we note that the energy locations of the Ln^{2+} ground states relative to the top of the VB as derived from CT measurements do have to be handled with care. A CT transition as looked at within a configurational coordinate diagram starts from the lowest vibrational level of the GS parabola and ends on an edge of the excited state parabola where the vibrational levels have their highest amplitude. This is the transition energy $E^{CT}(Ln^{3+})$ which was used by us for the GS level location of the divalent Ln ions. With this we ignore, though, the energy difference ΔE between the edge of the excited state parabola and its lowest vibrational level, i.e., the actual Ln^{2+} GS. This equilibrium Ln^{2+} GS is the starting point of the thermally stimulated electron release mechanism.

In summary it can be stated that, level location by means of Ln^{3+} CT energies is independent from an accurate location of the CB but it ignores relaxation processes and hence gives not the energetic location of the GS in equilibrium position. Level location by dint of TL activation energies against it does depend on the assignment of the CB bottom energy which may be subjected to experimental error as it is often poorly defined.

In the energy level diagrams presented in Figure 10 the energetic locations of the $Ln^{2+}:4f^{n+1}$ ground states set by the activation energies of the Ln-related TL glow peaks, i.e. the $E_{VC} - E_A$ values, and the Ln^{3+} CT energies, $E^{CT}(Ln^{3+})$, are brought into agreement at the best by means of equation (4). As already mentioned in Section 4.2., the 4f energy levels of the Ln^{3+} ions that are included in the energy level diagrams (Figure 10) were placed with regard to the Eu^{3+}/Eu^{2+} 4f GS energy difference of 6.6 to 7.3 eV that was found in wide band gap compounds. Our choice of 6.6 eV was done in

Conclusions

view of the observed Dy^{3+} and Sm^{3+} emission that could be explained by assuming the hole-trapping mechanism explained in the previous section. Despite the small uncertainties in the location of the Ln 4f GS energies, the energy level diagrams are able to explain the Ln-related glow peaks and might be used in order to control TL processes and to design new TL materials with improved properties.

5. Conclusions

An experimental electron trapping and transport study on $\text{YPO}_4:\text{Ce}^{3+},\text{Ln}^{3+}$ and $\text{LuPO}_4:\text{Ce}^{3+},\text{Ln}^{3+}$ (Ln = Sm, Dy, Ho, Er, Tm) was presented and analyzed. It was concluded that after high energy radiation or direct Ce^{3+} excitation, the Ce^{3+} dopant ion becomes a hole-trap. The released electron on the other hand is trapped by the Ln^{3+} co-dopant. Both the $\text{Ce}^{4+}:4f^0$ and the $\text{Ln}^{2+}:4f^{n+1}$ ground states are stable at room temperature. During heating the trapped electron is thermally activated from the $\text{Ln}^{2+}:4f^{n+1}$ GS and recombines via the CB with Ce^{4+} . As a result of this recombination Ce^{3+} emission is observed. It was found that the systematic change in activation energies as a function of the type of Ln^{3+} co-doping ion that was derived from the thermo-luminescence glow peaks, is in good agreement with the Ln^{2+} GS energies with respect to the conduction band found via the $\text{O}^{2-} \rightarrow \text{Ln}^{3+}$ CT bands which for their part were identified in the VUV excitation spectra. Based on this analysis, energy level diagrams for both types of compounds were constructed that might be used in order to control TL processes and to design new TL materials with improved properties.

Acknowledgements

This work was supported by the Dutch Technology Foundation (STW).

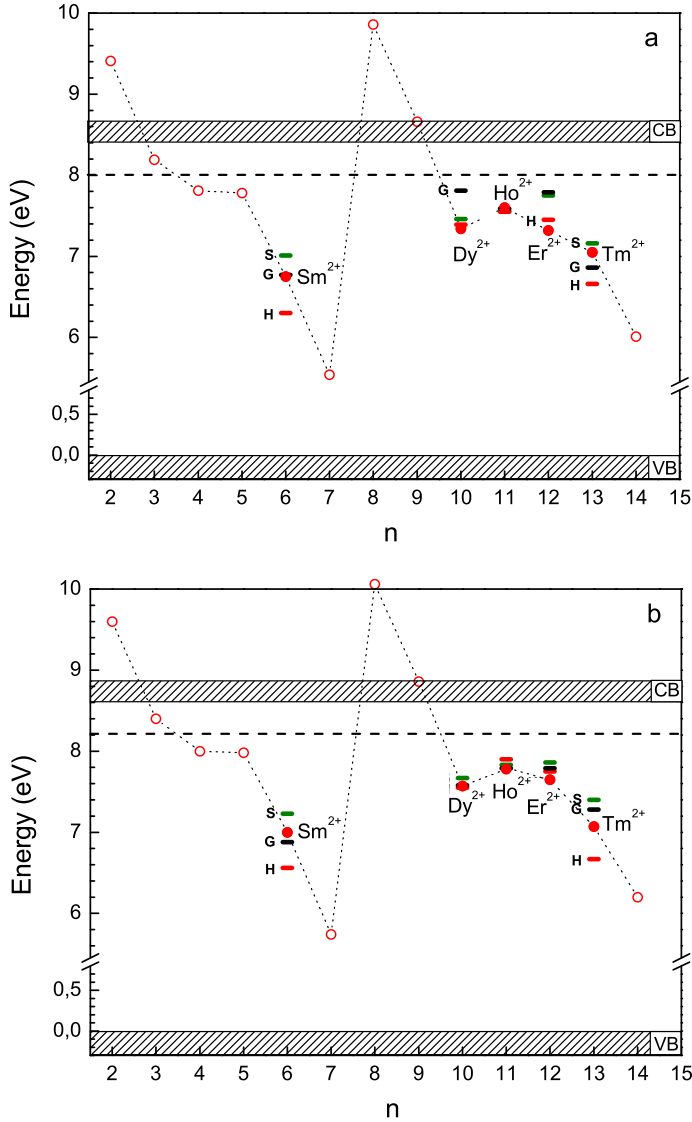


Fig. 10. Energy level diagrams of $YPO_4:Ln^{2+}$ (a) and $LuPO_4:Ln^{2+}$ (b); n is the number of electrons in the 4f shell of the divalent lanthanide ions. Filled circles indicate the host-dopant CT energies which have been identified in the VUV excitation spectra, whereas the open circles are prediction from the Dorenbos model. The dashed horizontal line indicates the lowest PO_4^{3-} group transition energy, $E(PO_4^{3-}, Ln^{3+})$. The energy levels based on the TL activation energies derived by three methods (S = simple formula, H = heating rate method, G = glow curve analysis) are displayed as well.

References

References

- [1] Kamada M., Murakami J., Ohno N., *J. Lumin.*, **87** (2000) 1042
- [2] Kamiyanagi Y., Kitaura M., Kaneyoshi M., *J. Lumin.*, **122** (2007) 509
- [3] Guo C., Zhang C., Lü Y., Tang Q., Su Q., *Phys. Status Solidi A*, **201** (2004) 1588
- [4] Jia D., Wang X., van der Kolk E., Yen W., *Opt. Commun.*, **204** (2002) 247
- [5] Jia D., Jia W., Evans D., Dennis W., Liu H., Zhu J., Yen W., *J. Appl. Phys.*, **88** (2000) 3402
- [6] Dorenbos P., *J. Phys.: Condens. Matter*, **15** (2003) 8417
- [7] Dorenbos P., *J. Lumin.*, **111** (2005) 89
- [8] Bos A.J.J., Dorenbos P., *Rad. Meas.*, **43** (2008) 222
- [9] Qi Z., Shi C., Liu M., Zhou D., Luo X., Zhang J., Xie Y., *Phys. Stat. Sol. (a)*, **201** (2004) 3109
- [10] Clabau F., Rocquefelte X., Jobic S., Deniard P., Whangbo M.H., Garcia A., Le Mercier T., *Solid State Science*, **9** (2007) 608
- [11] Hölsä J., Aitasalo T., Jungner H., Lastusaari M., Niittykoski J., Spano G., *J. Alloys and Comp.*, **374** (2004) 56
- [12] Arellano-Tanori O., Melendrez R., Pedroza-Montero M., Castanedeia B., Chernov V., Yen W.M., Barboza-Flores M., *J. Lumin.*, **128** (2008) 173
- [13] Milligan W. O., Mullica D. F., *Inorganica Chimica Acta*, **60** (1982) 39
- [14] Shannon R.D., *Acta Cryst.*, **A 32** (1976) 751
- [15] Nakazawa E., Shionoya S., *J. Phys. Soc. Jpn.*, **36** (1974) 504
- [16] van Pieterse L., *Proefschrift Universiteit Utrecht*, ISBN 90-393-2779-3 (2001)
- [17] Battisha I.K., *J. Sol-Gel Sc. Tech.*, **30** (2004) 163
- [18] Li J., Wang J., Tan H., Cheng X., Song F., Zhang H., Zhao S., *J. Cryst. Growth*, **256** (2003) 324
- [19] Dorenbos P., *J. Lumin.*, **91** (2000) 91
- [20] van Pieterse L., Reid M.F., Wegh R.T., Soverna S., Meijerink A., *Phys. Rev. B*, **65** (2002) 045113
- [21] van Pieterse L., Reid M.F., Burdick G.W., Meijerink A., *Phys. Rev. B*, **65** (2002) 045114-1

Chapter 4. Controlled Electron and Hole Trapping in $YPO_4:Ce^{3+},Ln^{3+}$ and $LuPO_4:Ce^{3+},Ln^{3+}$

- [22] Nakazawa E., Shiga F., *J. Lumin.*, **15** (1977) 255
- [23] Ni Y., Hughes J.M., Mariano A.N., *Amer. Mineral.*, **80** (1995) 21
- [24] Krumpel A.H., van der Kolk E., Zeelenberg D., Bos A.J.J., Krämer K.W., Dorenbos P., *J. Appl. Phys.*, **104** (2008) 073505
- [25] Chen R., McKeever S.W.S., *Theory of Thermoluminescence and Related Phenomena*, World Scientific, Singapore (1997)
- [26] Puchalska M., Bilski P., *Radiat. Meas.*, **41** (2006) 659
- [27] Dorenbos P., *J. Lumin.*, **108** (2004) 301
- [28] Lang R.J., *Can. J. Res.*, **14** (7) (1936) 127
- [29] Dorenbos P., *J. Phys.: Condens. Matter*, **15** (2003) 4797
- [30] Dorenbos P., *J. Lumin.*, **104** (2003) 239

Chapter 5

Charge Transfer Transitions in the Transition Metal Oxides $ABO_4:Ln^{3+}$ and $APO_4:Ln^{3+}$ ($A = La, Gd, Y, Lu, Sc$; $B = V, Nb, Ta$; $Ln = \text{Lanthanide}$)

Abstract

We have compiled and analyzed optical and structural properties of lanthanide doped non-metal oxides of the form $APO_4:Ln^{3+}$ and of transition metal oxides with formula $ABO_4:Ln^{3+}$. The main objective is to get a clearer understanding of such important parameters as band gap energy, $O^{2-} \rightarrow Ln^{3+}$ charge transfer energy or $Ln^{3+} \rightarrow B^{5+}$ inter-valence charge transfer energy. Such parameters provide the locations of the lanthanide 4f ground states relative to the conduction band and the valence band of the host, and these locations in turn determine the luminescent properties of a given material. Hence, understanding the relationship between the different types of charge transfer processes is of technological interest.

1. Introduction

Many lanthanide (Ln) doped transition metal (d-block) oxides of the form $ABO_4:Ln^{3+}$ ($A = La, Gd, Y, Lu$; $B = V, Nb, Ta$; $Ln = La, Ce, \dots Lu$) are well known compounds for different technological applications as laser host crystals [1, 2], solar cells [3] or phosphor materials [4]. Their luminescence properties depend on the location of the 4f energy levels of the Ln dopants relative to the valence band (VB) and the conduction band (CB) of the host. The energies of charge transfer (CT) transitions that can be identified in photoluminescence (PL) spectra can be used in order to establish those locations. In the ABO_4 transition metal oxides, a CT transition can be observed between the Ln dopant and a host ion or between the host ions themselves. Fig. 1 exemplifies the three different types of CT transitions which are of main interest throughout this paper: (i) Fundamental host transition due to electron transfer from the oxygen VB to the CB (band gap); (ii) inter-valence charge transfer (IVCT) transition from a Ln^{3+} ion to the CB; and (iii) electron transfer from an O^{2-} ion to the unfilled 4f

shells of the Ln^{3+} dopant. The oxygen 2p states form mainly the top of the VB and the d states of the B^{5+} ions form the bottom of the CB [5, 6, 7].

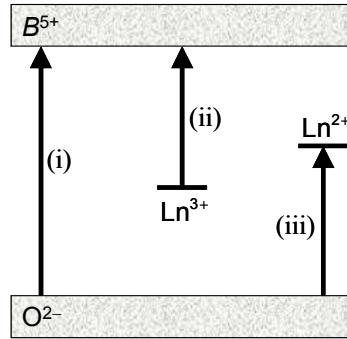


Fig. 1. Three different types of CT transitions: (i) Fundamental host transition, $O^{2-} \rightarrow B^{5+}$; (ii) IVCT transition, $Ln^{3+} \rightarrow B^{5+}$; (iii) electron transfer from ligand to dopant, $O^{2-} \rightarrow Ln^{3+}$.

At the beginning of this article, in section 2, an overview of the different methods of locating Ln 4f energy levels relative to the host bands by means of CT energies will be given. In particular, the method of Boutinaud based on the IVCT energies and the method of Dorenbos based on CT energies will be discussed. One main objective consists in comparing the different approaches with each other. Another objective is finding host-related parameters which help to predict the absolute location of the 4f energy levels in any compound. Section 3 presents first the crystallographic and electronic properties of the group 5 transition metal oxides $ABO_4:Ln^{3+}$ ($B = V, Nb, Ta$) and the non-metal oxides $APO_4:Ln^{3+}$ in tabular form. Next, the Eu^{3+} CT and the Pr^{3+} IVCT energies in these compounds are presented and discussed. It will be shown that both the $O^{2-} \rightarrow Eu^{3+}$ CT and the $Pr^{3+} \rightarrow B^{5+}$ IVCT energies for one specific type of compound as for instance the orthovanadates, $AVO_4:Ln^{3+}$, depend on the electronegativities as well as on the inter-atomic distances of the ions that are involved in the CT process. The dependence of the $Pr^{3+} \rightarrow B^{5+}$ IVCT energy on these two parameters for different transition metal oxides has been found earlier by Boutinaud [8]. His model and our attempt to express the $O^{2-} \rightarrow Eu^{3+}$ CT energies are an extension of the optical electronegativity model introduced by Jørgensen 4 decades ago [9]. The photoluminescence (PL) data that are used in this work were obtained by own measurements or from literature.

2. Knowledge on CT Energies

Lots of attempts were made in the last decades to predict the energy of CT transitions. The energies of CT transitions involving Ln dopant ions are intimately related with the position of the dopants ground state level with respect to the VB and the CB of the host crystal. Two different approaches to predict CT energies that gave the most promising results so far will be reviewed. (1) One of these approaches concentrates on correlations of the CT energy with numerical parameters as e.g. the optical electronegativity of one or both of the ions involved in the CT process or inter-atomic distances between electron donator and electron acceptor. Its strength is that one formula roughly expresses the CT energies of a large group of different compounds all doped with the same Ln ion. The original approach by Jørgensen [9] has been employed and refined by Boutinaud [8] in order to describe IVCT transitions. (2) The other approach in contrast concentrates on the energetic location of the lowest 4f and the lowest 5d states of the entire series of 14 Ln ions all singly doped in the same compound. It makes use of a characteristic zig-zag curve of the 4f electron binding energies that can be seen when going through the Ln series. The models of Dorenbos [10] and Nakazawa [11] are examples of this approach. In the following two sections these two approaches will be presented in more detail.

2.1. CT Energy and Related Numerical Parameters

2.1.1. The Model of Jørgensen

A simple expression for the first Laporte-allowed CT energy, E^{CT} , in an inorganic ionic compound was published by Jørgensen and is based on his definition of the *optical electronegativity*, χ_{opt} [9, 12]:

$$E^{CT} = (\chi_{opt}(X) - \chi_{opt}(M)) \cdot 3.72 \text{ eV} \quad (1)$$

X represents here the electron donor (ligand) and M the electron acceptor (metal ion) in the CT process. With a reversed sign, Eq. (1) describes the CT energy for an electron transfer from M to X . The optical electronegativities of the Ln ions are defined such that their values reflect the strength of the binding energy of the electron that is transferred to the Ln 4f shell. The binding energy is largest when the 4f shell becomes half (Eu) or completely (Yb) filled, and it is smallest for La and Gd. Expression (1) reflects the trend of CT energies for one specific Ln ion ($M = \text{lanthanide}$) reasonably

well going from one compound family to another (fluorides, chlorides, bromides, etc.). But it does not account for the difference in CT energies between members of e.g. the oxide family or the fluoride family of compounds [13]. Inside one particular type of compound as for instance the vanadates, AVO_4 , other parameters as the anion coordination number or the size of the rare earth ion do also have an effect on the CT energies [13]. Eq. (1) can be applied also to express the band gap energy of binary compounds with formula M_mX_n or compounds containing complexes of the form MX_n^{q-} [44].

2.1.2. The Model of Boutinaud

In Ln doped transition metal oxides a special metal to metal CT has been observed where the electron is transferred from the Ln dopant to the transition metal ion of the host. This CT is called Inter-Valence Charge Transfer (IVCT). Boutinaud [8, 14, 15] has developed an empirical model to describe IVCT transitions involving Pr^{3+} (and Tb^{3+}). His model not only considers the optical electronegativity as the model of Jørgensen but also the inter-atomic distances between Pr^{3+} (Tb^{3+}) and the transition metal ion B^{q+} . Using the position of the IVCT band of Pr^{3+} (or Tb^{3+}) doped closed-shell transition metal oxides, Boutinaud proposed the following linear relationship [8]:

$$E^{IVCT}(Pr^{3+}) = (1.96 - 1.66 \cdot \chi_{opt}(B^{q+})/d(Pr^{3+} - B^{q+})) \cdot 3.72 \text{ eV} \quad (2)$$

$d(Pr^{3+} - B^{q+})$ is the shortest inter-atomic distance (in Å) between Pr^{3+} and B^{q+} . Fig. 2 shows the Pr^{3+} IVCT energies in different compounds together with the straight line given by Eq. (2). The values for both the IVCT energies and the $\chi_{opt}(B^{q+})/d(Pr^{3+} - B^{q+})$ ratios inside Fig. 1 are taken from [8, 14, 16]. It will be shown in section 3.3. in more detail how Eq. (2) is related to Jørgensens formula (1), although here we deal with a metal to metal CT instead of an anion to metal CT.

The IVCT bands were identified in the excitation spectra of $Pr^{3+}:^1D_2$ and $Pr^{3+}:^3P_0$ emission in several transition metal oxides [14, 17, 18]. It was found that the Pr^{3+} IVCT has about the same energy as the Tb^{3+} IVCT energy. This implies that the location of the Pr^{3+} ground state is at about the same energy as the Tb^{3+} ground state within the energy level diagram, see Fig. 1. This is in agreement with an analysis on the temperature quenching behavior of the $Pr^{3+}:^3P_0$ and $Tb^{3+}:^5D_4$ emission in AVO_4 ($A = La, Gd, Y$) [17, 18], $CaNb_2O_6$ and $YNbO_4$ [8] (see also Section 3.4.). The model of Boutinaud describes very well the IVCT energies of Pr^{3+} for different oxides and shows therefore that the inter-atomic distance has an influence on IVCT transition energies.

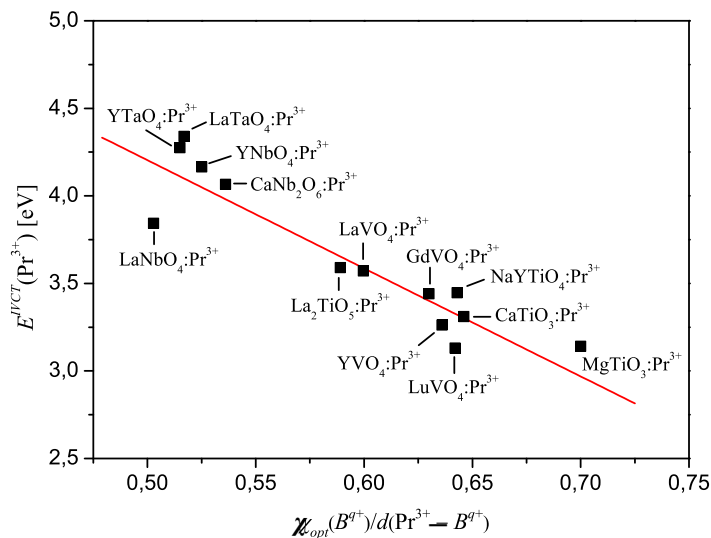


Fig. 2. $E^{IVCT}(\text{Pr}^{3+})$ plotted against the ratio between the optical electronegativity of the transition metal cation B^{q+} and the shortest $\text{Pr}^{3+} - B^{q+}$ distance; the numbers for each compound shown inside the figure were taken from [8, 14, 16].

2.2. The Zig-Zag Curve of Binding Energies

2.2.1. The Model of Dorenbos

Analyzing the lowest 4f-5d transition energies of Ln ions as dopants in different compounds, Dorenbos found that for all Ln ions when on the same site in the same compound this energy decreases as compared to its value for the free gaseous ion by the same host-specific amount. This energy decrease was named redshift or depression $D(q+, A)$; $q+$ stands for the Ln ionic charge and A for the compound name. From experimental techniques like ultraviolet photoelectron spectroscopy (UPS), X-ray photoelectron spectroscopy (XPS), photoconductivity measurements, excited state absorption (ESA), or luminescence quenching studies the energy difference between the delocalized VB or CB levels and a localized Ln 4f GS or 5d level can be determined [19, 20, 21, 22]. Dorenbos combined information from these techniques with information on the energy for charge transfer from an anion ligand to trivalent Ln ions in compounds to locate the 4f ground state of lanthanides relative to the top of the VB. The results have been depicted by him in special energy level diagrams [10, 23]. When going through the lanthanide series from La to Lu, the 4f GS locations relative to the VB and the CB of the host compound form a characteristic zig-zag or double-

seated curve similar to the one shown in Fig. 3. The curve has minima when the 4f shell is half and fully filled with electrons and maxima when it is filled with one or eight electrons. We point out that the diagrams proposed by Dorenbos are not based on the calculated energy levels of a quantum mechanical system but show energy differences that were measured or expected on grounds of simple, empirical relations. The shape of the zig-zag curve appears to be almost the same in all types of compounds, even though its location relative to VB and CB changes. This equality of shape means that when the energy of CT from the VB to only one Ln ion, for instance of Eu^{3+} , is known, the CT energies to all other lanthanides when doped on the same lattice site in the same compound are known as well:

$$E^{CT}(n) \cong E^{CT}(6) + \Delta E^{CT}(n) \quad (3)$$

n is the number of electrons in the 4f shell of the trivalent lanthanide ion where $n = 6$ for Eu^{3+} , and the host independent constant $\Delta E^{CT}(n)$ is compiled in [10]. Depending on the band gap of the host material, the 4f ground state of Eu^{2+} is separated from the 4f ground state of Eu^{3+} by about 5.7 eV to about 6.7 eV [24].

2.2.2. The Model of Nakazawa

On the basis of Jørgensens theoretical work on the variation of the lowest 4f-5d and CT transition energies of Ln ions as a function of the number of electrons in their 4f shell [9], Nakazawa published a theoretical approach which concentrates on the 4f-5d and CT transition energies using the examples of $YPO_4:Ln^{3+}$ [25] or $LaPO_4:Ln^{3+}$ [11].

Nakazawa started with a representation of the transition energies by means of Slater, Condon and spin-orbit interaction parameters and he derived a simple expression of the form

$$E^{CT}(n) = V_{CT0} + v_{CT}n - \Delta U(n+1), \quad (4)$$

where V_{CT0} and v_{CT} are empirical parameters describing the single-electron-scheme binding energies in (4) and $\Delta U(n+1)$ is the many-electron correction term given for each n in [11]. E^{CT} can then be obtained for all lanthanide ions by fitting few experimental values with formula (4). In Fig. 3 the zig-zag curve for CT energies in $YPO_4:Ln^{3+}$ as proposed by Dorenbos is compared to the one predicted by the model of Nakazawa [25]. Apart from few variations (at most 0.56 eV for Gd) the two curves are similar. As mentioned in section 2.1.1., the values of the optical electronegativities of the Ln ions are related to the binding energy of the electron added to the Ln 4f shell. When going through the Ln series from La, Ce to Lu, the binding energies form the same zig-zag curve as shown in Fig. 3

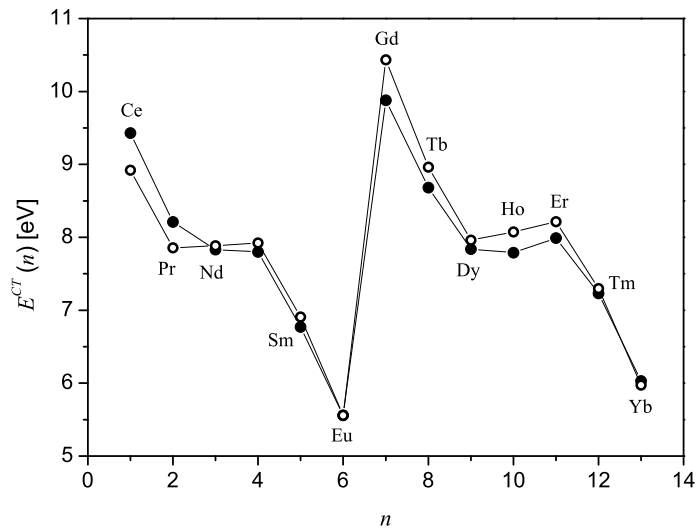


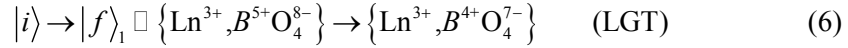
Fig. 3. $E^{CT}(n)$ for $\text{YPO}_4:\text{Ln}^{3+}$ determined from the models of Dorenbos (●) and Nakazawa (○) [25]; for both models $E^{CT}(6)$ 5.56 eV (223 nm) was chosen as reference; n = number of electrons in the Ln^{3+} 4f shell.

2.3. Relationship between IVCT Energy and 4f Electron Binding Energy

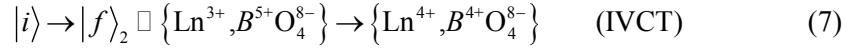
Dorenbos states that the Ln^{3+} CT energies shown in Fig. 3 for $\text{YPO}_4:\text{Ln}^{3+}$ give approximately the 4f ground state locations of the divalent Ln dopant ions (Ln^{2+}) relative to the VB of the host [10]. The complete zig-zag curve shown in Fig. 3, however, is not based exclusively on measured CT energies. It is also based on an assumed or alleged location of the lowest 5d states relative to the bottom of the CB. Then, by subtracting the predicted 4f-5d energy differences using the appropriate value for the redshift, one obtains also the Ln^{2+} :4f GS energy relative to the top of the VB. It was proposed in [10] that the lowest 5d level location of the trivalent Ln dopants behave in a similar fashion as those for the divalent ones. We obtain then a similar curve for the 4f ground state energies of the Ln^{3+} ions relative to the VB as the ones shown in Fig. 3. It appears now that the zig-zag curve for the trivalent lanthanides as proposed by Dorenbos in [10] contradicts with the results from the IVCT model of Boutinaud. The IVCT model of Boutinaud (B) (see Section 2.1.2.) shows that the energy difference between the 4f GS energies of Pr^{3+} and Tb^{3+} relative to the VB of the host, $\Delta E(\text{Pr}^{3+}, \text{Tb}^{3+})$, is negligible, whereas the model of Dorenbos (D) predicts the 4f GS energy of Tb^{3+} to be about 0.73 eV higher than the one of Pr^{3+} :

$$\Delta E^B(\text{Pr}^{3+}, \text{Tb}^{3+}) \cong 0 \text{ eV} < \Delta E^D(\text{Pr}^{3+}, \text{Tb}^{3+}) = 0.73 \text{ eV} \quad (5)$$

We restrict the following discussion to the transition metal compounds with formula ABO_4 ($B = \text{V, Nb, Ta}$). Furthermore we confine ourselves to a simple ionic picture in which we single out a BO_4^{3-} group with an adjacent Ln^{3+} ion to which we refer as the system $\{Ln^{3+}, BO_4^{3-}\}$ with initial state $|i\rangle$. The lowest BO_4^{3-} group transition (LGT) is treated to be a CT from O^{2-} to B^{5+} which changes the system as follows (Fig. 4 a).



Eq. (6) describes by definition an electron transfer from the top of the VB to the bottom of the CB. The IVCT will be treated as a CT from Ln^{3+} to B^{5+} which changes the system according to (Fig. 4 b):



In principle, the transferred electron may be bound by the Coulomb potential of Ln^{4+} or of the hole in the VB or it may reside as a free electron in the CB [26]. Let us assume here that in both cases, Eq. (6) and Eq. (7), the electron is transferred into the same electronic state that involves somehow the B^{4+} cation.

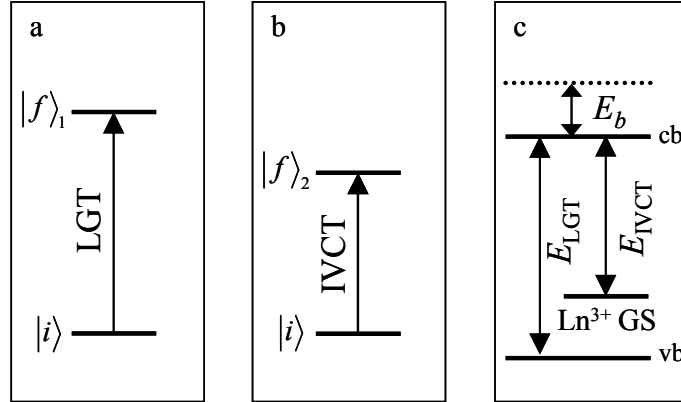


Fig. 4. Energy level schemes depicting the $\{Ln^{3+}, B^{5+}O_4^{8-}\} \rightarrow \{Ln^{3+}, B^{4+}O_4^{7-}\}$ LGT (a), and the $\{Ln^{3+}, B^{5+}O_4^{8-}\} \rightarrow \{Ln^{4+}, B^{4+}O_4^{8-}\}$ IVCT (b). In the scheme that combines the two CT transitions (c) the energy differences are depicted relative to a common ionization level (dotted horizontal line); E_{LGT} = LGT energy; E_{IVCT} = IVCT energy; E_b = binding energy; vb = valence band, cb = conduction band.

In order to relate energetically the LGT to the IVCT within one energy level diagram, we assume that the energy needed to remove the transferred electron from the B^{4+} cation is about the same both in the $\{Ln^{3+}, B^{4+}O_4^{7-}\}$ and the $\{Ln^{4+}, B^{4+}O_4^{8-}\}$ system. This means that the transferred electron in the final state $|f\rangle_1$ has about the same binding energy than the transferred electron in state $|f\rangle_2$. The total energy of the system in state $|f\rangle_1$, however, is larger than the total energy of the system in state $|f\rangle_2$. By looking on the binding energy of the electron instead of the energy of the whole system, equations (6) and (7) can be depicted in one diagram as shown in Fig. 4 c. The IVCT model of Boutinaud provides us then with the energy difference between the 4f ground state of Ln^{3+} (Pr^{3+} and Tb^{3+}) and the CB. The Dorenbos model on the other hand provides us with the energy difference between the lowest 4f state of Ln^{2+} and the top of the VB. The Boutinaud model and the Dorenbos model can now be united in order to provide the locations of the lowest 4f energy levels for all tri- and divalent lanthanides in the energy difference scheme of one compound.

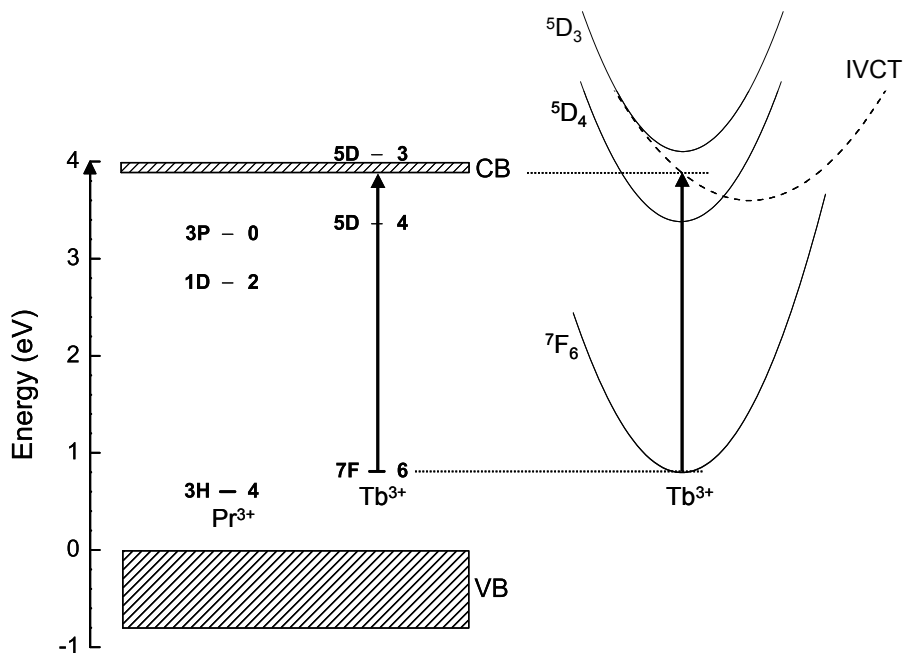


Fig. 5. Energy level diagram (left side) and configurational coordinate diagram (right side) of $GdVO_4:Ln^{3+}$ ($Ln = Pr, Tb$); arrows indicate the IVCT transition as used for energy level location.

Be it that Fig. 4 c describes the situation reasonably well, then the similarity of the activation energies found from the temperature quenching behavior of the $Pr^{3+}:^3P_0$ and $Tb^{3+}:^5D_4$ emission respectively is in line with the observed similarity of the Pr^{3+} and the Tb^{3+} IVCT energies as can be seen in Fig. 5: Placing the $Pr^{3+}:^3H_4$ and the $Tb^{3+}:^7F_6$ ground states at a similar energy implies that the $Pr^{3+}:^3P_0$ and the $Tb^{3+}:^5D_4$ energy levels are at the about the same energy as well. The quenching of the $Pr^{3+}:^3P_0$ and the $Tb^{3+}:^5D_4$ emission can happen via an IVCT state or the CB as shown in the configurational coordinate diagram on the right hand side in Fig. 5.

3. Characterization and Analysis of the $ABO_4:Ln^{3+}$ System

This chapter compiles important crystallographic and electronic properties of the $ABO_4:Ln^{3+}$ system. The $O^{2-} \rightarrow Eu^{3+}$ CT and the $Pr^{3+} \rightarrow B^{5+}$ IVCT will be discussed and a formula will be presented that relates the CT energy to the distance between Eu^{3+} and O^{2-} . It will be shown how the band gap energy can be expressed by means of the $O^{2-} \rightarrow Ln^{3+}$ CT and the $Ln^{3+} \rightarrow B^{5+}$ IVCT energies.

3.1. The Crystal Structures of the ABO_4 Compounds

Table 1 compiles structural information on the ABO_4 compounds studied in this work.

The orthovanadates AVO_4 ($A = \text{Ce}, \dots, \text{Lu}$) have a tetragonal zircon-type structure with space group $I4_1/amd$ (Nr. 141), whereas $LaVO_4$ has a monoclinic monazite-type structure with space group $P2_1/n$ (Nr. 14) (see Table 1). Despite the difference in structure, in all orthovanadates of rare earths the vanadium ions are coordinated by 4 oxygen atoms. Nevertheless, the band gap of $LaVO_4$, i.e. the lowest VO_4^{3-} group transition energy, $E(VO_4^{3-})$, is about 0.46 eV larger than that of all the other orthovanadates (see Table 2).

The structure of the rare earth orthoniobates $ANbO_4$ is temperature dependent. At low temperatures they have monoclinic scheelite (fergusonite)-type structure with space group $I2/a$ (Nr. 15), whereas at higher temperatures (500 – 850 °C [52]; for instance: $T > 495$ °C for $LaNbO_4$, and $T > 725$ °C for $NdNbO_4$ [53]) it transforms into the tetragonal scheelite-type structure with space group $I4_1/a$ (Nr. 88).

The orthotantalates $ATaO_4$ crystallize in three different structures: (1) the monoclinic fergusonite- or M-type with space group $I2/a$ (Nr. 15, for $A = \text{Nd}, \dots, \text{Er}$), (2) the structurally related M'-type with space group $P2_1/a$ (Nr. 13, for $A = \text{Nd}, \dots, \text{Er}$), and (3) the $P2_1/c$ type (Nr. 14, for $A = \text{La}, \text{Ce}, \text{Pr}$). Table 1 compiles the average interatomic distances, $d(\text{Ta}^{5+} - \text{O}^{2-})$, in $M-ATaO_4$ ($A = \text{Gd}, \text{Y}, \text{Lu}$) which were estimated from the two shortest $\text{Ta}^{5+} - \text{O}^{2-}$ distances given in the cited references for the M'-type of these compounds. The average distances between A^{3+} and O^{2-} , $d(A^{3+} - O^{2-})$, are assumed to be approximately the same for the M- and M'-type of the $ATaO_4$ compounds [55].

Table 1. A = f-block elements or P; B = d-block elements; r = effective ionic radius [27]; the space group is represented by its Hermann Mauguin symbol and number, as recorded in the International Tables for Crystallography [28]; I_5 = 5th ionization potential [29]; χ_P = electronegativity (Pauling scale) [30, 31]; $d(R-O)$ ($R = A, B$) = average inter-atomic distance in polyhedra of the ABO_4 structures (values in parenthesis are estimated); CN = coordination number (same reference as space group or inter-atomic distance).

| ABO_4 | $r(A^{3+})$ [pm] | $r(B^{5+})$ [pm] | Space Group (Number) | $d(O-A)$ [pm] | $d(O-B)$ [pm] | $I_5(B)$ [eV] | $\chi(A^3)$ (A^{3+}) | CN (A^{3+}) | CN (B^{5+}) |
|-----------------------|---------------------|---------------------|---|---------------------|------------------------|------------------|-----------------------------|--------------------|--------------------|
| LaVO ₄ | 121.6 | 35.5 | P2 ₁ /n (14) ³² | 259.7 ³² | 170.9 ³² | 65 | 1.63 | 9 | 4 |
| GdVO ₄ | 105.3 | 35.5 | I4 ₁ /amd (141) ³³ | 248.3 ³³ | 160.4 ³³ | 65 | 1.63 | 8 | 4 |
| YVO ₄ | 101.9 | 35.5 | I4 ₁ /amd (141) ³⁴ | 236.5 ³⁵ | 170.88 ³⁵ | 65 | 1.63 | 8 | 4 |
| LuVO ₄ | 97.7 | 35.5 | I4 ₁ /amd (141) ³⁵ | 233.1 ³⁵ | 170.67 ³⁵ | 65 | 1.63 | 8 | 4 |
| LaNbO ₄ | 116 | 48 | I2/a (15) ³⁶ | 250.5 ³⁷ | 209.8 ³⁸ | 51 | 1.6 | 8 | 4+2 |
| GdNbO ₄ | 105.3 | 48 | I2/a (15) ³⁹ | 239.4 ³⁸ | 207.3 ³⁸ | 51 | 1.6 | 8 | 4+2 |
| YNbO ₄ | 101.9 | 48 | I2/a (15) ^{39,40} | 236.3 ⁴⁰ | 207.5 ⁴⁰ | 51 | 1.6 | 8 | 4+2 |
| LuNbO ₄ | 97.7 | 48 | I2/a (15) ³⁹ | 232.3 ⁴¹ | 205.7 ⁴¹ | 51 | 1.6 | 8 | 4+2 |
| LaTaO ₄ | 116 | 64 | P2 ₁ /c (14) ^{42,43} | 254.4 ⁴³ | 199 ⁴³ | 45 | 1.5 | 8 | 4+2 |
| M-GdTaO ₄ | 105.3 | 64 | I2/a (15) ⁴⁴ | 241.1 ⁴³ | (193.25) ⁴³ | 45 | 1.5 | 8 | 4+2 |
| M'-GdTaO ₄ | 105.3 | 64 | P2/a (13) ⁴⁴ | 241.1 ⁴³ | 202.3 ⁴³ | 45 | 1.5 | 8 | 4+2 |
| M-YTaO ₄ | 101.9 | 64 | I2/a (15) ^{45,46} | 235.5 ⁴⁵ | (190.4) ⁴⁵ | 45 | 1.5 | 8 | 4+2 |
| M'-YTaO ₄ | 101.9 | 64 | P2/a (13) ⁴⁴ | 235.5 ⁴⁵ | 201.1 ⁴⁵ | 45 | 1.5 | 8 | 4+2 |
| M-LuTaO ₄ | 97.7 | 64 | I2/a (15) ⁴⁷ | 235.3 ⁴³ | (191.2) ⁴³ | 45 | 1.5 | 8 | 4+2 |
| M'-LuTaO ₄ | 97.7 | 64 | P2/a (13) ⁴⁷ | 235.3 ⁴³ | 199.7 ⁴³ | 45 | 1.5 | 8 | 4+2 |
| LaPO ₄ | 121.6 | 17 | P2 ₁ /n (14) ^{48,49} | 257.3 ⁴⁸ | 153.4 ⁴⁸ | 65 | 2.19 | 9 | 4 |
| GdPO ₄ | 110.7 | 17 | P2 ₁ /n (14) ^{49,50} | 246.9 ⁵⁰ | 153 ⁵⁰ | 65 | 2.19 | 9 | 4 |
| YPO ₄ | 101.9 | 17 | I4 ₁ /amd (141) ^{49,51} | 233.7 ⁵¹ | 154.3 ⁵¹ | 65 | 2.19 | 8 | 4 |
| LuPO ₄ | 97.7 | 17 | I4 ₁ /amd (141) ^{49,51} | 230.3 ⁵¹ | 153.4 ⁵¹ | 65 | 2.19 | 8 | 4 |
| SePO ₄ | 87 | 17 | I4 ₁ /amd (141) ^{49,51} | 220.6 ⁵¹ | 153.4 ⁵¹ | 65 | 2.19 | 8 | 4 |

The crystal structures of the orthophosphates APO_4 are similar to that of the orthovanadates, AVO_4 : $LaPO_4$ and $CePO_4$ are isostructural to $LaVO_4$, i.e. they have the monoclinic monazite-type structure with space group $P2_1/n$ (Nr. 14), whereas APO_4 ($A = \text{Sm, Eu, Gd, Y, Sc, Lu}$) have a tetragonal zircon-type structure with space group $I4_1/amd$ (Nr. 141).

3.2. Energy of Charge Transfer from the Valence Band to Eu^{3+}

Table 2 compiles the Eu^{3+} and band gap CT energies for the ABO_4 compounds.

Table 2. $E(BO_4^{3-})$ = lowest transition energy in BO_4 group; $E^{CT}(Eu^{3+})$ = CT energy of Eu^{3+} ; where no reference is given, the values are taken from own measurements.

| ABO_4 | $E(BO_4^{3-})$ [eV] | $E^{CT}(Eu^{3+})$ [eV] |
|---------------------|--|---|
| $LaVO_4$ | 4.26 ¹⁷ | 3.41 ¹⁷ , 3.94 |
| $GdVO_4$ | 3.9 ¹⁸ | --- |
| YVO_4 | 3.87 ^{54,83} , 3.76 ⁵⁶ | 4.77 ⁵⁷ |
| $LuVO_4$ | 3.83 ¹⁸ | --- |
| $ScVO_4$ | 3.72 ⁵⁸ , 3.69 ⁵⁴ | --- |
| $LaNbO_4$ | 4.84 ⁵⁹ (NbO_4) 4.13 ⁵⁹ (NbO_6) | 4.61 |
| $GdNbO_4$ | 4.58 ⁶⁰ | --- |
| $YNbO_4$ | 4.68 ⁶¹ , 4.4 ⁶² | 5.1 ⁶³ , 4.84 ⁶³ |
| $LuNbO_4$ | --- | 5.17 ⁴⁷ |
| $ScNbO_4$ | 4.77 ^{58, 64} | --- |
| $LaTaO_4$ | 4.77 ⁶⁵ | 4.43 ⁶⁵ |
| $M\text{-}GdTaO_4$ | 5.32 ⁶⁶ , 5.39 ⁶⁷ | 5 ⁶⁶ |
| $M'\text{-}GdTaO_4$ | 5.41 ⁶⁶ | 5 ⁶⁶ , 4.96 ⁴⁴ |
| $M\text{-}YTaO_4$ | 5.51 ⁶⁵ | 5.06 ⁶⁵ |
| $M'\text{-}YTaO_4$ | --- | 4.88 ⁶⁸ |
| $M\text{-}LuTaO_4$ | --- | --- |
| $M'\text{-}LuTaO_4$ | --- | 5.17 ⁴⁷ |
| $ScTaO_4$ | 4.77 ⁶⁹ | --- |
| $LaPO_4$ | 8 ⁷⁰ , 7.8 ⁷¹ | 4.84 ^{72, 11} |
| $GdPO_4$ | 7.75 ⁷¹ | 5 ¹¹ |
| YPO_4 | 8.16 ⁷¹ | 5.66 ¹¹ , 5.56 ^{11,25,54} |
| $LuPO_4$ | 8.55 ⁷¹ | 5.74 ¹¹ |
| $ScPO_4$ | 7.47 ⁵⁷ , 7.21 ⁷³ | 6.05 ⁵⁷ , 5.96 ⁵⁴ |

For $LaVO_4$ we compiled another value for the $O^{2-} - Eu^{3+}$ CT energy, $E^{CT}(Eu^{3+})$, than in our earlier work [17]. After a new analysis, a shoulder in the excitation spectrum of $LaVO_4:Eu^{3+}$ at about 315 nm has been assigned to the Eu^{3+} CT.

The $O^{2-} \rightarrow Eu^{3+}$ CT is an anion ligand to metal CT and can, in principle, be expressed by Eq. (1). Eq. (1) does, however, not account for variations in the value for the CT energy within for example the oxides family of compounds or within any other family of compounds. In this section we will propose a modification to Eq. (1) in order to reproduce the A -dependent ($A = La, Gd, Y, Lu$) Eu^{3+} CT energies for the transition metal oxides with formula $ABO_4:Eu^{3+}$ ($B = V, Nb, Ta$) and for the non metal oxides $APO_4:Eu^{3+}$. In the Eu^{3+} CT, oxygen is the electron donor and europium, the lanthanide, the electron acceptor. Thus, from the lanthanide's standpoint, the Eu^{3+} CT is the opposite of the IVCT, meaning, the lanthanide receives an electron instead of giving one off. This thought suggests that the IVCT model of Boutinaud (see Section 2.1.2) should also be applicable to the Eu^{3+} CT energy. In fact, a correlation has been observed between the Eu^{3+} CT energy and the ionic radius of the rare earth which is being replaced by the Eu^{3+} dopant in a rare earth oxide [13]: The Eu^{3+} CT increases non-linearly with decreasing size of the host cation. Following the idea of Boutinaud, we may express the Eu^{3+} CT energy, $E^{CT}(Eu^{3+})$, given in Table 2, as a function of the average inter-atomic distance, $d(O^{2-} - Eu^{3+})$, between the Eu^{3+} dopant ion and its oxygen ligands in a compound with formula $ABO:Eu^{3+}$.

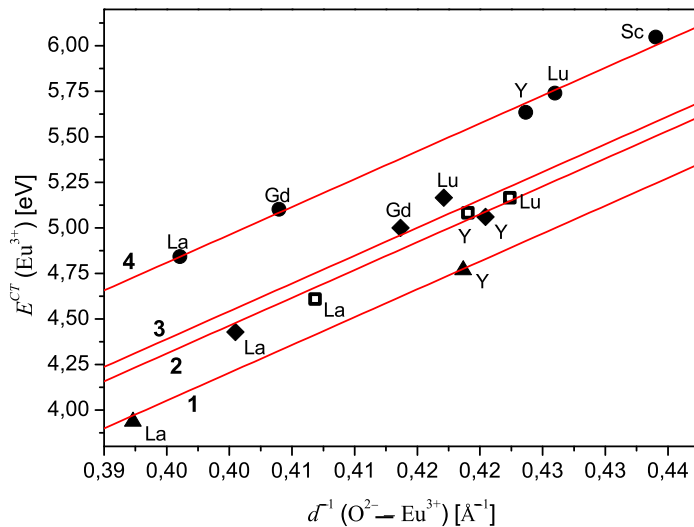


Fig. 6. $E^{CT}(Eu^{3+})$ plotted against the reciprocal of the average interatomic distance $d(O^{2-} - Eu^{3+})$ for the vanadates (curve 1, ▲), the niobates (curve 2, ■), the tantalates (curve 3, ◆) and the phosphates (curve 4, ●); host cation A is specified inside the figure.

In order to account for anion relaxation that occurs when Eu^{3+} substitutes for a host rare earth, A^{3+} , with a different ionic radius we assume that the average $\text{O}^{2-} - \text{Eu}^{3+}$ distance is expressed as

$$d(\text{O}^{2-} - \text{Eu}^{3+}) \cong d(\text{O}^{2-} - A^{3+}) + 0.5 \cdot (r(\text{Eu}^{3+}) - r(A^{3+})) \quad (6)$$

Fig. 6 shows $E^{CT}(\text{Eu}^{3+})$ plotted against $d^{-1}(\text{O}^{2-} - \text{Eu}^{3+})$ for $ABO_4:\text{Eu}^{3+}$ ($A = \text{La, Gd, Y, Lu}$; $B = \text{V, Nb, Ta}$) and $APO_4:\text{Eu}^{3+}$ ($A = \text{La, Gd, Y, Lu, Sc}$). We observe for each type of compound that the $\text{O}^{2-} \rightarrow \text{Eu}^{3+}$ CT energy increases with decreasing size of the substituted lattice rare earth cation. Such relationship between the Eu^{3+} CT energy and the decreasing lattice site has been observed earlier [54]. In order to get a better understanding of this relationship we look at Eq. (1) that expresses the difference between two energy values: One related to the electron donor, and one to the electron acceptor. Eq. (1) can principally be modified in the following way so as to reproduce the trend shown in Fig. 6.

$$\begin{aligned} E^{CT}(\text{Eu}^{3+}) &= \left\{ a \cdot \chi_{opt}(\text{O}^{2-}) - \left(1 - \frac{b}{d(\text{O}^{2-} - \text{Eu}^{3+})} \right) \cdot \chi_{opt}(\text{Eu}^{3+}) \right\} \cdot 3.72 \text{ eV} \\ &= \left\{ a \cdot \chi_{opt}(\text{O}^{2-}) - \chi_{opt}(\text{Eu}^{3+}) + \frac{b \cdot \chi_{opt}(\text{Eu}^{3+})}{d(\text{O}^{2-} - \text{Eu}^{3+})} \right\} \cdot 3.72 \text{ eV} \end{aligned} \quad (7)$$

To motivate this equation, let us look at two compounds, viz. $\text{LaBO}_4:\text{Eu}^{3+}$ and $\text{LuBO}_4:\text{Eu}^{3+}$ ($B = \text{V, Nb, Ta, P}$). As the ionic radius of La^{3+} is about 18.3 up to 23.9 pm, depending on the coordination number of La^{3+} , larger than that of Lu^{3+} , the O^{2-} to Eu^{3+} distance will be larger in $\text{LaBO}_4:\text{Eu}^{3+}$ compared to $\text{LuBO}_4:\text{Eu}^{3+}$, see Eq. (6). The binding energy of the electron transferred to the Eu^{3+} dopant ion that is involved in the CT process will be affected by the Coulomb interaction with the neighboring negative anions. A closer distance to the adjoining oxygen ions will decrease the electron binding at the lanthanide site and consequently the energy of CT for Eu^{3+} on a Lu^{3+} site tends to be higher than on a La^{3+} site. In Eq. (7) this is accounted for by the correction term $1 - b/d(\text{O}^{2-} - \text{Eu}^{3+})$. We anticipate also that the binding of the electron on the donating oxygen ligand may depend on the anion to cation distance. A smaller size rare earth cation can have two effects: (i) A small ionic radius is accompanied with a higher value for the electronegativity. It leads to slightly stronger binding of the oxygen ligand. (ii) A closer distance to the positive rare earth leads to stronger Coulomb binding of the electron. Fig. (7) displays schematically the situation. We expect, however, that the energy of the O^{2-} ion that is involved in the CT process will not be affected too much when going from $\text{LaVO}_4:\text{Eu}^{3+}$ to $\text{LuVO}_4:\text{Eu}^{3+}$ as it is mainly surrounded by B^{5+} ions (see Fig. 7) that provide the strongest binding anyway.

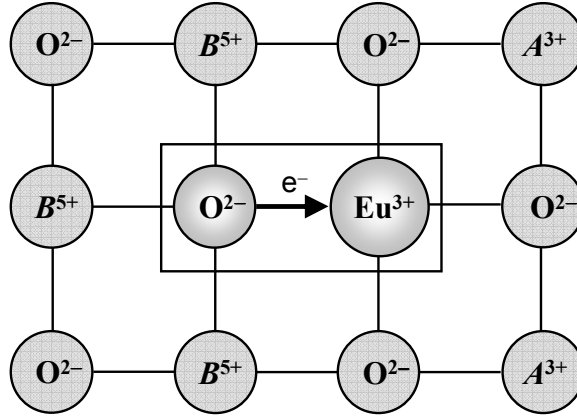


Fig. 7. Simplified Eu^{3+} CT transition scheme including the nearest neighbors for a compound with formula $ABO_4:Eu^{3+}$; the arrow pointing from the O^{2-} ion to the Eu^{3+} ion indicates the direction of electron transfer.

Table 3 displays the fitting parameters that were used in Eq. (7) in order to get the straight lines shown in Fig. 6.

Table 3. Fitting parameters of the Eu^{3+} CT energy in $ABO_4:Eu^{3+}$ expressed by Eq. (7); $C1 \equiv b \cdot \chi_{opt}(Eu^{3+})$; the second parameter $C2 \equiv a \cdot \chi_{opt}(O^{2-}) - \chi_{opt}(Eu^{3+})$ is specified at $d^{-1}(O^{2-} - Eu^{3+}) = 0.4 \text{ \AA}^{-1}$.

| B | $C1$ | $C2$ |
|-----|------|------|
| V | 8.22 | 1.13 |
| Nb | 8.22 | 1.20 |
| Ta | 8.22 | 1.22 |
| P | 8.22 | 1.34 |

An inverse proportionality between the direct band gap energy and the inter-atomic distance can be found in the simple binary compounds with formula A_1O_1 , such as the alkaline earth metal oxides ($A = Ba, Sr, Ca, Mg$) [13, 74], the group 10 element oxides ($A = Ni, Pd$) [75], or the group 12 element oxides ($A = Zn, Cd$) [76]. In the case of the alkaline earth oxides the valence bands are mainly formed by oxygen p states, whereas the bottom of the conduction band consists mainly of metal s and d states [77, 78]. Although the particular electronic configuration of each metal has an influence on the width of the band gap, we might assume that the physical process that causes the

inverse proportional relationship between the CT energy and the inter-atomic distance is similar both in the alkaline earth metal oxides and the Eu^{3+} doped transition metal oxides. Indeed, it is known for many compounds that the band gap is inversely proportional to the size of the host cation, the states of which form the CB [13]. It has also been observed that the band gap is directly proportional to the Eu^{3+} CT energy, the constant of proportionality being approximately 3 [13].

3.3. The Energy of the $Pr^{3+} - B^{5+}$ Inter-Valence Charge Transfer

In the $ABO_4:Ln^{3+}$ ($A = \text{La, Gd, Y, Lu}$; $B = \text{V, Nb, Ta, P}$) compounds the B cation has always oxidation state 5+ with a noble gas electron configuration: $V^{5+} [\text{Ar}]$, $Nb^{5+} [\text{Kr}]$, $Ta^{5+} [\text{Xe}]$, $P^{5+} [\text{Ne}]$. Column 3 in Table 1 shows that the P^{5+} ion has a much smaller effective ionic radius and a larger electronegativity than the other cations. This is related with a stronger binding between the oxygen ligands and phosphorus, and consequently the band gap in the orthophosphates is larger than the one of the transition metal oxides as can be seen in Table 2. In the small band gap transition metal oxides no 5d-4f emission can be observed. This can be explained by assuming that all Ln 5d states are located above the lowest excited BO_4^{3-} ($B = \text{V, Nb, Ta}$) state. In the phosphates the lowest 5d state is energetically located inside the band gap and 5d-4f emission is observed [79]. If both the Ln^{3+} 4f ground state and the lowest 5d energy level are energetically located inside the band gap, the first intense Ln^{3+} 4f-5d excitation band is at lower energy than the weak $Ln^{3+} \rightarrow B^{5+}$ IVCT band. Consequently, the IVCT band is completely overwhelmed and not observable in excitation spectra. If on the other hand the Ln^{3+} 4f ground state is located inside the band gap but the lowest 5d state is above it than an $Ln^{3+} - B^{5+}$ IVCT can be observed. This explains why IVCT transitions have only been observed in Ln doped transition metal oxides and not in APO_4 phosphates.

In $YTaO_4:Ln^{3+}$ the lowest energy 4f-5d excitation band of Tb^{3+} emission is expected at the same wavelength of about 275 nm as the Pr^{3+} and Tb^{3+} IVCT band [15, 61]. Lammers and Blasse [67] assigned the weak excitation band at 295 nm of Tb^{3+} emission in $GdTaO_4:Tb^{3+}$ to the spin-forbidden transition from the $Tb^{3+}:4f^8$ GS to the $4f^7 5d^1 :^9D$ level. The model of Boutinaud predicts the $Tb^{3+} - Ta^{5+}$ IVCT band at about 298 ± 13 nm [8]. In those situations it is difficult to assign the observed band either to 4f-5d or IVCT transitions.

Another interesting feature was observed for the vanadates, $AVO_4:Pr^{3+}$, and the titanates, $ATiO_3:Pr^{3+}$ [56]: The IVCT energy increases linearly with increasing $Pr^{3+} - B^{5+}$ ($B = \text{V, Ti}$) distance itself, where the latter one is affected by the size of the A^{q+} cation. This is implied in Eq. (2) although it seems not to be the case for the niobates and the tantalates [56]. In order to account for the observed linear dependence of the Pr^{3+} IVCT energy on the $Pr^{3+} - B^{5+}$ distance, we can again modify Eq. (1) in order to approximate the Pr^{3+} IVCT energy within the orthovanadates or within the tantalates by

$$\begin{aligned}
 E^{IVCT}(\text{Pr}^{3+}) &= \left\{ \left(1 - \frac{a}{d(\text{Pr}^{3+} - B^{5+})} \right) \cdot \chi_{opt}(\text{Pr}^{3+}) - b \cdot \chi_{opt}(B^{5+}) \right\} \cdot 3.72 \text{ eV} \\
 &= \left\{ \chi_{opt}(\text{Pr}^{3+}) - b \cdot \chi_{opt}(B^{5+}) - \frac{a \cdot \chi_{opt}(\text{Pr}^{3+})}{d(\text{Pr}^{3+} - B^{5+})} \right\} \cdot 3.72 \text{ eV}
 \end{aligned} \tag{8}$$

As can be seen from column 6 in Table 1, the O^{2-} to B^{5+} distance is not affected very much by the rare earth cation of the host. That means that the Pr^{3+} to B^{5+} distance is determined mainly by the O^{2-} to Pr^{3+} distance. Therefore the relationship between the binding energy of the B^{5+} cation and the Pr^{3+} to B^{5+} distance has been neglected in Eq. (8). Eq. (8) explains the change in Pr^{3+} IVCT energy when going from $\text{LaVO}_4:\text{Pr}^{3+}$ to $\text{LuVO}_4:\text{Pr}^{3+}$. It does not explain the difference in IVCT energies when going through the transition metal oxides as done by Boutinaud. In that latter case Eq. (2) holds.

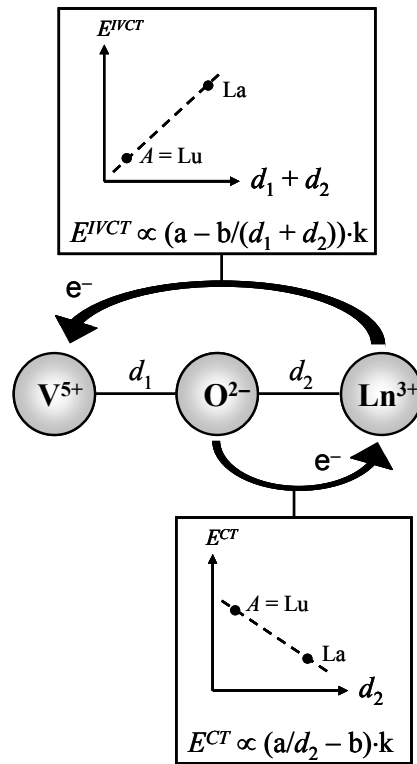


Fig. 8. One-dimensional CT transition scheme for the orthovanadates, $AVO_4:Ln^{3+}$; the arrows pointing from one ion to another one indicate the direction of electron transfer between the ions. Inside the two boxes the dependence of the $O^{2-} \rightarrow Ln^{3+}$ CT (lower box, $Ln = \text{Eu}$) energy and the $Ln^{3+} \rightarrow V^{5+}$ IVCT (upper box, $Ln = \text{Pr}$) energy on the inter-atomic distances d_1 and d_2 is shown; k is a constant.

The difference between Eq. (7) and Eq. (8) is schematically depicted in Fig. 8 using the vanadates as an example. The upper box summarizes the relationship between the $Ln^{3+} \rightarrow V^{5+}$ IVCT energy and the Ln^{3+} to V^{5+} distance, and the lower box shows the dependence of the $O^{2-} \rightarrow Ln^{3+}$ CT energy on the O^{2-} to Ln^{3+} distance.

3.4. The Band Gap Energy and its Relationship with Electronegativity and Ionization Potentials

In the case of the transition metal oxides, the band gap energy, $E(BO_4^3)$, increases with decreasing value for the 5th ionization potential, $I_5(B)$, listed in column 7 of Table 1, and with decreasing value for the Pauling electronegativity, $\chi_P(B)$, of the metal cation B , listed in column 8 of Table 1. A large 5th ionization potential, as for the vanadates, implies a relatively strong binding when an electron is transferred to the B^{5+} ion, and therefore the band gap energies are relatively low. Besides the properties of the B^{5+} cation also the size of the A^{3+} cation within an ABO_4 group of compounds ($B = V, Nb, Ta, P$) affect the band gap as can be seen in Table 2. This latter observation will be discussed in more detail in the following section.

3.4.1. The Band Gap of Transition Metal Oxides

In the AVO_4 rare earth metal orthovanadates it was observed earlier by Blasse and Brill that the maximum of the vanadate (VO_4^{3-}) emission band depends on the size of the rare earth cation A^{3+} [58, 80, 81]: the smaller its effective ionic radius, $r(A^{3+})$, with a certain coordination number is, the more the maximum of the VO_4^{3-} emission band is shifted towards longer wavelengths. Also the band gap decreases with decreasing size of A^{3+} , as can be seen in Table 2. The same correlation was observed for the alkaline earth tungstates, AWO_4 ($A = Ba, Ca, Cd, Cu, Pb, Sr, Zn$) [7]: also here the band gap energy depends approximately linearly on the effective ionic radius of the A^{2+} ions, viz., the smaller the $r(A^{2+})$, the lower the band gap energy is. Lacombe-Perales *et al.* argue that the decrease in band gap energy is caused by an increase of the crystal-field splitting of the O^{2-} 2p states (it raises the top of the VB) and of the W^{6+} 5d states (it lowers the bottom of the CB), in combination with a hybridization of these oxygen and tungsten states with the p , d , or f valence electrons of the A^{2+} cations. A similar argument could hold for the orthovanadates where the CB consists mainly of V^{5+} 3d states.

The orthoniobates and orthotantalates differ from the vanadates and tungstates [7] by the fact that they all have a monoclinic structure, independent from the size of the A^{3+} cation. In the case of the tantalates, the correlation between $E(TaO_4^{3-})$ and $r(A^{3+})$ is comparable with the orthophosphates [82]: The smaller $r(A^{3+})$, the larger $E(BO_4^3)$ (see Table 2). $ScBO_4$ ($B = Nb, Ta, P$) appears to be a special case. The relation between

$E(NbO_4^{3-})$ and the size of A^{3+} is not clear in the orthoniobates due to the inconsistent assignment of band gap values in the literature (see Table 2). Both in the niobates and the M' -type tantalates, however, the B^{5+} ($B = Nb, Ta$) ions are coordinated by six oxygen atoms. The special structure of the orthoniobates and orthotantalates may indicate a different type of interaction between the A^{3+} ions and the surrounding oxygen ions. It might be that the binding energy of the oxygen atoms, which is affected by the Coulomb potential and therewith the size of the A^{3+} ions, might be the dominant parameter in BO_4 group transitions. This thought will be explained in more detail for the orthophosphates in section 3.4.2.

In Fig. 9 the observed trends in Eu^{3+} CT and Pr^{3+} IVCT energies mentioned in Sections 3.2. and 3.3. are depicted in one energy level scheme. Fig. 9 illustrates that the energy of CT from the VB to a trivalent Ln dopant ion tends to increase with smaller size of A^{3+} . The lowest BO_4^{3-} group transition energy, that has been expressed within a simple ionic picture by Eq. (6) in section 2.3., decreases for $B = V$ and increases for $B = Ta$ (see Table 2) with decreasing size of A^{3+} . Fig. 9 makes clear why the Pr^{3+} IVCT energy decreases with decreasing size of A^{3+} for the orthovanadates, while the Eu^{3+} CT energy increases simultaneously.

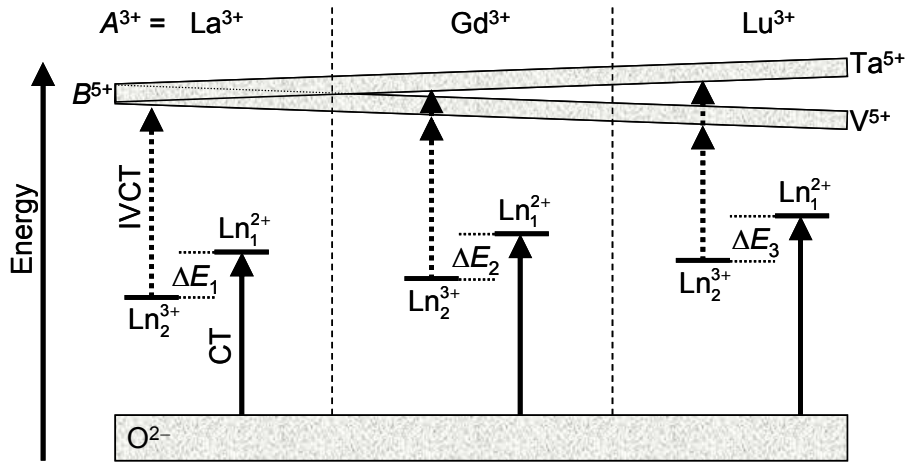


Fig. 9. Energy level diagram for the transition metal oxides $ABO_4:Ln^{3+}$ ($A = La, Gd, Lu$), showing the change in $O^{2-} \rightarrow A^{3+}$ CT energy and $O^{2-} \rightarrow B^{5+}$ CT energy for different host cations, and the effect this change has both on the $O^{2-} \rightarrow Ln_1^{2+}$ CT and the $Ln_2^{3+} \rightarrow B^{5+}$ IVCT energies, where $B = V$ (1) and $B = Ta$ (2); the ΔE indicate the energy difference between the 4f ground states of the Ln_1^{2+} and the Ln_2^{3+} ions.

In view of Fig. 9, the Pr^{3+} IVCT energy is expected to show less dependence on the size of A^{3+} in the tantalates in comparison to the vanadates. This is indeed the case

when looking at the different Pr^{3+} IVCT energies for the tantalates and vanadates that have been collected by Boutinaud *et al.* [56]. The difference between the Pr^{3+} IVCT energy in $LaTaO_4:Pr^{3+}$ and the one in $YTaO_4:Pr^{3+}$ is negligible, whereas the difference between the corresponding energy in $LaVO_4:Pr^{3+}$ and the one in $YVO_4:Pr^{3+}$ is about 0.31 eV [16].

When we neglect the effect of lattice relaxation after an electron transfer on the location of Ln 4f ground states, the lowest BO_4^{3-} group transition energy of a transition metal oxide with formula $ABO_4:Ln^{3+}$ ($A = \text{rare earth}$; $B = V, Nb, Ta$) can be expressed as

$$E_A(BO_4^{3-}) = E_A^{CT}(Ln_1^{3+}) + E_A^{IVCT}(Ln_2^{3+}) - \Delta E_A(Ln_1^{2+}, Ln_2^{3+}) \quad (9)$$

where $\Delta E_A(Ln_1^{2+}, Ln_2^{3+})$ is the energy difference between the 4f ground states of Ln_1^{2+} and Ln_2^{3+} .

Table 4 compiles both the band gap energy, $E_A(BO_4)$, and the found energy difference $\Delta E_A(Eu^{2+}, Pr^{3+})$ for the vanadates, the niobates and the tantalates. $E_A(BO_4)$ was taken from Table 2, and $\Delta E_A(Eu^{2+}, Pr^{3+})$ was derived with the help of Eq. (9), whereby we have taken the values of $E_A^{CT}(Eu^{3+})$ from Table 2 and the values of $E_A^{IVCT}(Pr^{3+})$ from reference [16].

Table 4. Band gap energies, $E_A(BO_4)$, and energy differences, $\Delta E_A(Eu^{2+}, Pr^{3+}) = E_A^{CT}(Eu^{3+}) + E_A^{IVCT}(Pr^{3+}) - E_A(BO_4^{3-})$ (see Eq. 9) for the vanadates, niobates and tantalates. The energies are given in eV.

| ABO_4 | $E_A(BO_4)$ | $\Delta E_A(Eu^{2+}, Pr^{3+})$ |
|--------------------|-------------|--------------------------------|
| LaVO ₄ | 4.26 | 3.25 |
| YVO ₄ | 3.87 | 4.16 |
| LaNbO ₄ | 4.84 | 3.6 |
| YNbO ₄ | 4.4 | 4.86 |
| LaTaO ₄ | 4.77 | 4 |
| YTaO ₄ | 5.5 | 3.83 |

When we compare two compounds with formulas $A1BO_4:Ln^{3+}$ and $A2BO_4:Ln^{3+}$, where $A1$ and $A2$ indicate two different rare earth host cations, then we find the following relations from Table 4:

$$E_{A1}(BO_4^{3-}) > E_{A2}(BO_4^{3-}) \Leftrightarrow \Delta E_{A1} < \Delta E_{A2} \quad (10)$$

Relation (10) is an observation and will necessarily be influenced by the unavoidable variations in the assignment of the CT excitation bands that have to be taken into consideration.

Conclusion

3.4.2. The Band Gap of Non-Metal Orthophosphates

Similar to the orthoniobates and the orthotantalates, also in the orthophosphates the band gap shows an inverse proportionality to the size of A^{3+} . Both in the monazite and the xenotime structure of the orthophosphate with formula APO_4 , oxygen atoms coordinate to two A atoms and one P atom [49]. This means that not only the P^{5+} ions but also the A^{3+} ions have, due to their size and charge, an effect on the stabilization of the oxygen ions which are involved in the PO_4^{3-} group transition: The smaller the A^{3+} ions and the higher their charge, the larger the electrons binding energy within the O^{2-} ions will be. This explains the correlation between band gap and size of A^{3+} as shown in Table 2. But we also have observed another interesting aspect in the orthophosphates which seems to contradict the former explanation: In the VUV excitation spectra of $APO_4:Ce^{3+},Ln^{3+}$ ($A = Y, Lu; Ln = Sm, Dy, Ho, Er, Tm$), monitoring Ln^{3+} emission, we could notice a linear relation between the lowest PO_4^{3-} excitation energy and the effective ionic radius of the Ln^{3+} co-dopant [82], similar to AVO_4 ($A = V, W$): The smaller the radius, the lower the PO_4^{3-} transition energy. The local lattice distortion around an activator A_2 in a compound with formula $A_1PO_4:A_2^{3+}$ does therefore bring about a fundamental different effect than the same ion would cause in a compound with formula A_2PO_4 .

4. Conclusion

Any charge transfer (CT) energy in an inorganic ionic compound can basically be expressed as a difference between two parameters, one referring to the electron donor and the other one to the electron acceptor. Jørgensen approximated the CT energy between a ligand and a central atom with the help of the so-called optical electronegativities of these two ions. His simple expression describes reasonably well the trend in CT energies when going from one family of compounds to another one (fluorides, chlorides, bromides,...). The CT energy, however, is not constant but varies between different members of these compound families. Boutinaud *et al.* found a linear relation between the $Pr^{3+} \rightarrow B^{q+}$ ($B =$ transition metal) inter-valence charge transfer (IVCT) energy and the quotient between the optical electronegativity of the B^{q+} cation and the $Pr^{3+}-B^{q+}$ distance. His formula reflects the trend of IVCT energies inside various transition metal oxides. Following the idea of including the inter-atomic distances, we found a linear relation between the $O^{2-} \rightarrow Eu^{3+}$ CT energies and the $O^{2-} - Eu^{3+}$ distances in both the transition metal oxides, $ABO_4:Eu^{3+}$, and the phosphates, $APO_4:Eu^{3+}$. Within the energy level diagrams that were introduced by Dorenbos few years ago, the lowest BO_4^{3-} group transition energy, i.e., the band gap, should be expressible in the case of the transition metal oxides as the sum of the Eu^{3+} CT and the Pr^{3+} IVCT energies minus the difference between the Eu^{2+} and the Pr^{3+} ground state

energies. With this, it becomes apparent that the electronic properties of the BO_4^{3-} ion depend on the size of the (rare earth) cation adjacent to it. Yet, the band gap of the orthophosphates $APO_4:Ln^{3+}$ can not be expressed in this manner because they do not show any IVCT excitation bands. Although within the phosphates the band gap energy also shows a dependency on the size of the A^{3+} ion, their generally larger band gap in comparison to the transition metal oxides can not be explained with the same parameters that explain the difference in band gap energies between the latter types of oxides, meaning for instance between the vanadates and the tantalates. The fact that the diverse parameters in Table 1, describing structural and electronic properties, are unable to connect the orthophosphates with the transition metal oxides points to the complexity of the nature of CT transitions.

Acknowledgements

This work was supported by the Dutch Technology Foundation (STW).

References

References

- [1] Zhang L., Hu Z., Lin Z., Wang G., *J. Cryst. Growth*, **260** (2004) 460
- [2] Barnes N.P., Storm M.E., Cross P.L., Skolant M.W., *J. Quantum Electron.*, **26** (1990) 558
- [3] Liu J., Yao Q., Li Y., *Appl. Phys. Lett.*, **88** (2006) 173119
- [4] Yu M., Lin J., Wang S., *Appl. Phys. A: Mater. Sci. Proc.*, **80** (2005) 353
- [5] Kutzler F.W., Ellis D.E., *Phys. Rev. B*, **29** (1984) 1008
- [6] Machida M., Murakami S., Kijima T., *J. Phys. Chem. B*, **105** (2001) 3289
- [7] Lacomba-Perales R., Ruiz-Fuertes J., Errandonea D., Martínez-García D., Segura A., *EPL*, **83** (2008) 37002
- [8] Boutinaud P., Cavalli E., Bettinelli M., *J. Phys.: Condens. Matter*, **19** (2007) 386230
- [9] Jørgensen C.K., *Modern Aspects of Ligand Field Theory*, North-Holland Publishing Company – Amsterdam, London (1971)
- [10] Dorenbos P., *J. Phys.: Condens. Matter*, **15** (2003) 8417
- [11] Nakazawa E., Shiga F., *Jpn. J. Appl. Phys.*, **42** (2003) 1642
- [12] Lever A.P.B., *Inorganic Electronic Spectroscopy*, Elsevier Amsterdam (1968)
- [13] Dorenbos P., *J. Lumin.*, **111** (2005) 89
- [14] Boutinaud P., Mahiou R., Cavalli E., Bettinelli M., *Chem. Phys. Lett.*, **418** (2005) 181
- [15] Boutinaud P., Putaj P., Mahiou R., Cavalli E., Speghini A., Bettinelli M., *Spectr. Lett.*, **40** (2007) 209
- [16] Boutinaud P., Pinel E., Oubaha M., Mahiou R., Cavalli E., Bettinelli M., *Opt. Mater.*, **28** (2006) 9
- [17] Krumpel A.H., van der Kolk E., Dorenbos P., Boutinaud P., Cavalli E., Bettinelli M., *Mater. Sc. Eng. B*, **146** (2008) 114
- [18] Krumpel A.H., van der Kolk E., Cavalli E., Boutinaud P., Bettinelli M., Dorenbos P., *J. Phys.: Condens. Matter*, **21** (2009) 115503
- [19] Sato S., *J. Phys. Soc. Japan*, **41** (1976) 913
- [20] Thiel C.W., Gruguel H., Wu H., Sun Y., Lapeyre G.J., Cone R.L., Equall R.W., Macfarlane R.M., *Phys. Rev. B*, **64** (2001) 085107

Chapter 5. Charge Transfer Transitions in $ABO_4:Ln^{3+}$ ($B =$ Transition Metal) and $APO_4:Ln^{3+}$

- [21] Pedrini C., Rogemond F., McClure D.S., *J. Appl. Phys.*, **59** (1986) 1196
- [22] Lawson J.K., Payne S.A., *J. Opt. Soc. Am B*, **8** (1991) 1404
- [23] Dorenbos P., *J. Phys.: Condens. Matter*, **15** (2003) 2645
- [24] Dorenbos P., van der Kolk E., *Appl. Phys. Lett.*, **89** (2006) 061122-1
- [25] Nakazawa E., *J. Lumin.*, **100** (2002) 89
- [26] Mahlik S., Grinberg M., Cavalli E., Bettinelli M., Boutinaud P., *J. Phys.: Condens. Matter*, **21** (2009) 105401
- [27] Shannon R.D., *Acta Cryst.*, **A 32** (1976) 751
- [28] Hahn T. (Editor), *International Tables for Crystallography, Volume A*, (2005) DOI 10.1107/97809553602060000100
- [29] Huheey J.E., Keiter E.A., Keiter R.L., *Inorganic Chemistry. Principles of Structure and Reactivity*, Addison Wesley (1993)
- [30] Pauling L., *J. Am. Chem. Soc.*, **54** (1932) 3570
- [31] Pauling L., *The Nature of the Chemical Bond*, 3rd ed., Cornell University Press: Ithaca NY (1960)
- [32] Rice C.E., Robinson W.R., *Acta Cryst.*, **B 32** (1976) 2232
- [33] Mahapatra S., Ramanan A., *J. Alloys Compd.*, **395** (2005) 149
- [34] Wang X. Loa I., Syassen K., Hanfland M., Ferrand B., *Phys. Rev. B*, **70** (2004) 064109
- [35] Chakoumakos B.C., Abraham M.M., Boatner L.A., *J. Solid State Chem.*, **109** (1994) 197
- [36] Tsunekawa S., Takei H., *Phys. Stat. Sol. A*, **50** (1978) 695
- [37] Mariathasan J.W.E., *Acta Cryst. B*, **41** (1985) 179
- [38] Trunov V.K., Kinzhbalo L.N., *Dokl. Akad. Nauk SSSR*, **263** (1982) 348
- [39] Tsunekawa S., Kamiyama T., Sasaki K., Asano H., Fukuda T., *Acta Cryst. A*, **49** (1993) 595
- [40] Weitzel H., Schröcke H., *Z. Kristallogr.*, **152** (1980) 69
- [41] Beda A.G., Bush A.A., Volkov A.F., Meshcheryakov V.F., *Kristallografiya*, **47** (2002) 357
- [42] Kurova T.A., Aleksandrov V.B., *Dokl. Akad. Nauk SSSR*, **201** (1971) 1095
- [43] Hartenbach I., Lissner F., Nikelski T., Meier S.F., Müller-Bunz H., Schleid T., *Z. Anorg. Allg. Chem.*, **631** (2005) 2377

References

- [44] Liu X., Xu X., Gu M., Xiao L., Han K., Zhang R., *Appl. Surf. Sc.*, **253** (2007) 4344
- [45] Brixner L.H., Chen H.-Y., *J. Electrochem. Soc.*, **130** (1983) 2435
- [46] Ferguson R.B., *Canad. Mineral.*, **6** (1957) 72
- [47] Blasse G., Dirksen G.J., Brixner L.H., Crawford M.K., *J. Alloys Compd.*, **209** (1994) 1
- [48] Mullica D.F., Grossie D.A., *Inorganica Chimica Acta*, **95** (1984) 231
- [49] Ni Y., Hughes J.M., Mariano A.N., *Amer. Mineral.*, **80** (1995) 21
- [50] Mullica D.F., Grossie D.A., Boatner L.A., *Inorganica Chimica Acta*, **109** (1985) 105
- [51] Milligan W. O., Mullica D. F., *Inorganica Chimica Acta*, **60** (1982) 39
- [52] Brixner L.H., Whitney J.F., Zumsteg F.C., Jones G.A., *Mat. Res. Bull.*, **12** (1977) 17
- [53] Takei H., Tsunekawa S., *J. Cryst. Growth*, **38** (1977) 55
- [54] Blasse G., Bril A., *Philips Tech. Rev.*, **31** (1970) 304
- [55] Wolten G.M., *Acta Cryst.*, **23** (1967) 939
- [56] Boutinaud P., Mahiou R., Cavalli E., Bettinelli M., *J. Lumin.*, **122** (2007) 430
- [57] van Pieterse L., Meijerink A., *J. Alloys Compd.*, **300** (2000) 426
- [58] Blasse G., Bril A., *J. Chem. Phys.*, **50** (1969) 2974
- [59] Hsiao Y.J., Fang T.H., Chang Y.S., Chang Y.H., Liu C.H., Ji L.W., Jywe W.Y., *J. Lumin.*, **126** (2007) 866
- [60] Liu X.M., Lin J., *J. Lumin.*, **122** (2007) 700
- [61] Schipper W.J., Hoogendorp M.F., Blasse G., *J. Alloys Compd.*, **202** (1993) 283
- [62] Lee S.K., Chang H., Han C.H., Kim H.J., Jang H.G., Park H.D., *J. Solid State Chem.*, **156** (2001) 267
- [63] Xiao X., Yan B., *J. Non-Cryst. Sol.*, **351** (2005) 3634
- [64] Blasse G. Dirksen G.J., *Mat. Chem Phys.*, **14** (1986) 485
- [65] Blasse G., Bril A., *J. Lumin.*, **3** (1970) 109
- [66] Li B., Gu Z., *J. Mater. Sc.*, **32** (2000) 1139
- [67] Lammers M.J.J., Blasse G., *Mat. Res. Bull.*, **19** (1984) 759
- [68] Hwang M.H., Kim Y.J., *Ceramics International*, **34** (2008) 1117
- [69] Brixner L.H., *J. Chem. Edu.*, **57** (1980) 588
- [70] Sasum U., Kloss M., Rohmann A., Schwarz L., Haberland D., *J. Lumin.*, **72** (1997) 255

Chapter 5. Charge Transfer Transitions in $ABO_4:Ln^{3+}$ ($B = \text{Transition Metal}$) and $APO_4:Ln^{3+}$

- [71] Nakazawa E., Shiga F., *J. Lumin.*, **15** (1977) 255
- [72] van Schaik W., Lizzo S., Smit W., Blasse G., *J. Electrochem. Soc.*, **140** (1993) 216
- [73] Trukhin A., Boatner L.A., *Mat. Sc. Forum*, **239** (1997) 573
- [74] Protheroe A.R., Steinbrunn A., Gallon T.E., *Surf. Sc.*, **126** (1983) 534
- [75] Matar S.F., Campet G., *J. Phys. Chem. Sol.*, **68** (2007) 331
- [76] Duffy J.A., *J. Phys. C: Solid St. Phys.*, **13** (1980) 2979
- [77] Taurian O.E., Springborg M., Christensen N.E., *Solid State Commun.*, **55** (1985) 351
- [78] Springborg M., Taurian O.E., *J. Phys. C: Solid State Phys.*, **19** (1986) 6347
- [79] Dorenbos P., *J. Lumin.*, **91** (2000) 91
- [80] Blasse G., Bril A., *J. Chem. Phys.*, **48** (1968) 217
- [81] Blasse G., *Philips Res. Rept.*, **23** (1968) 344
- [82] Krumpel A.H., Bos A.J.J., Bessière A., van der Kolk E., Dorenbos P., *Phys. Rev. B.*, **80** (2009) 085103
- [83] Toma S.Z., Palumbo D.T. *J. Electrochem. Soc.*, **117** (1970) 236

Summary

Locating Energy Levels of Lanthanide Ions in Inorganic Ionic Compounds

The luminescence properties of lanthanide (Ln) activated compounds depend on the energetic locations of the Ln 4f and 5d energy levels relative to the conduction band (CB) and the valence band (VB) of the particular host. In this thesis three different energies have been identified in experimental data that allow the construction of energy level diagrams that display these locations: (i) The energies of charge transfer (CT) transitions between two ions which were taken from photoluminescence (PL) excitation spectra; (ii) activation energies for temperature quenching of the activator's luminescence based on PL emission spectra; (iii) thermoluminescence (TL) activation energies derived from Ln-related glow curves. In this work we have applied TL to two different types of compounds and we have shown how the energy level diagrams might contribute to a future TL technology.

In addition to the construction of energy level diagrams for different compounds based on experimental data (Chapters 2 – 4), we also studied the change in luminescence properties when going from one compound to another one (Chapter 5). Chapter 2 presents a detailed photoluminescence (PL) study on the orthovanadates, $AVO_4:Ln^{3+}$ ($A = La, Gd, Lu$; $Ln = Ce, Pr, Eu, Tb$). It was found that the band gap energy, that is the lowest VO_4^{3-} transition energy, is about 0.5 eV higher in $LaVO_4$ than in $GdVO_4$ and $LuVO_4$. Furthermore, we could confirm in the emission spectra of $GdVO_4:Ce^{3+}$ and $LuVO_4:Ce^{3+}$ an observation that has been done in other vanadates already in the 1960's by Blasse and Brill: The smaller the effective ionic radius of A with a certain coordination number is, the more the maximum of the vanadate emission band is shifted to longer wavelengths. None of the PL spectra shows 5d-4f emission or 4f-5d excitation. This indicates that in the energy level diagrams of $AVO_4:Ln^{3+}$ ($A = La, Gd, Lu$) the 5d states of the Ln dopant ions are located inside the CB. The diagrams of $GdVO_4$ and $LuVO_4$ also explain why no $Tb^{3+}:^5D_3$ emission could be observed in these orthovanadates as this state is energetically located inside the CB. The ground state energies of the divalent ions are all energetically located inside the CB as well, except for $LaVO_4:Eu^{3+}$, from which follows that the orthovanadates, AVO_4 , can not contain Ln dopant ions with oxidation state 2. For the same reason these Ln dopant ions can not even serve as meta-stable electron-traps. On the other hand the ground state energies of Ce^{3+} , Pr^{3+} and Tb^{3+} are energetically located above the VB and could

therefore serve as stable hole-traps. From an analysis of the temperature dependent $\text{Pr}^{3+} : ^3\text{P}_0$ and $\text{Tb}^{3+} : ^5\text{D}_4$ luminescence quenching it could be concluded that the Pr^{3+} and Tb^{3+} 4f ground states have a similar energetic location relative to the host bands within the energy level diagrams.

Chapter 3 presents a detailed PL and TL study on Ln mono- and Ce-Ln co-doped NaLaF_4 . Based on PL-, TL-spectra and information from literature about the energy difference between the $4f^6$ GSE of Eu^{3+} and the $4f^7$ GSE of Eu^{2+} in wide band gap compounds a complete energy level diagram for $\text{NaLaF}_4:\text{Ln}^{3+}$ has been constructed. In the case of Ln mono-doped NaLaF_4 we found that the TL was due to 4f-4f emission from the Ln^{3+} dopant ion. $\text{NaLaF}_4:\text{Ln}^{3+}$ (Ln = Ce, Pr, Tb) show 2 TL-bands, whereas $\text{NaLaF}_4:\text{Ln}^{3+}$ (Ln = Nd, Dy, Ho, Er) feature only one TL-band. $\text{NaLaF}_4:\text{Ln}^{3+}$ (Eu, Gd, Yb) show either no or very weak TL. In Ce-Ln co-doped NaLaF_4 the TL emission was mainly due to 5d-4f emission from Ce^{3+} . The Ln-specific glow peaks, however, could not be explained by means of the energy level diagram alone. It was shown that in addition to the energy level diagram two assumptions, viz. the presence of two host related electron traps and the presence of V_k -centers, are necessary for explaining all Ln-specific glow peaks. We concluded that (i) an Ln ion can serve as an electron trap only when its $\text{Ln}^{2+} : 4f^{n+1}$ GSE is located below or close to the activation energies of the host related E1- and E2-electron-traps relative to the CB; (ii) an Ln ion can serve as a hole trap only when its $\text{Ln}^{3+} : 4f^n$ GSE is located above the V_{kA} -center GSE, E_A , relative to the VB.

Chapter 4 presents X-ray excited emission-, and VUV excitation-spectra together with TL glow curves of both $\text{YPO}_4:\text{Ce}^{3+}, \text{Ln}^{3+}$ and $\text{LuPO}_4:\text{Ce}^{3+}, \text{Ln}^{3+}$ (Ln = Sm, Dy, Ho, Er, Tm). Based on the emission and excitation spectra accurate energy level diagrams for both types of compounds have been constructed. In view of these diagrams it was concluded that after high energy radiation or direct Ce^{3+} excitation, the Ce^{3+} dopant ion becomes a hole-trap. The released electron on the other hand may be trapped by the Ln^{3+} co-dopant. Both the $\text{Ce}^{4+} : 4f^0$ and the $\text{Ln}^{2+} : 4f^{n+1}$ ground states are stable at room temperature. During heating (from room temperature up to 500 °C) the trapped electron is released from the $\text{Ln}^{2+} : 4f^{n+1}$ GS and recombines via the CB with Ce^{4+} . As a result of this recombination Ce^{3+} emission can be observed. The activation energy that is needed in order to release the electron from its trap was derived from the Ln-related glow peak. The energy level diagrams show that the Ln^{2+} GS locations found via TL activation energies are in good agreement with the respective values given by the $\text{O}^{2-} \rightarrow \text{Ln}^{3+}$ CT bands which for their part were identified in the VUV excitation spectra. Similar to the previous study on NaLaF_4 , this work shows that the constructed diagrams might be used in order to control TL processes and to design new TL materials with improved properties.

Chapter 5 finally compiles and analyzes optical and structural properties of

Summary

lanthanide doped non-metal oxides of the form $APO_4:Ln^{3+}$ and of transition metal oxides with formula $ABO_4:Ln^{3+}$ ($A = La, Gd, Y, Lu$; $B = V, Nb, Ta$; $Ln = La, Ce, \dots Lu$). Many of these compounds have been studied in-depth in the previous chapters. The main objective was to get a clearer understanding of such important parameters as band gap energy, meaning the lowest BO_4 group transition energy, $O^{2-} \rightarrow Ln^{3+}$ charge transfer energy or $Ln^{3+} \rightarrow B^{5+}$ inter-valence charge transfer energy. At the beginning of the 1970's, Jørgensen showed that the CT energy between a ligand and a central atom can be approximated roughly with the difference of the so-called optical electronegativities of these two ions. His simple expression describes reasonably well the trend in CT energies when going from one family of compounds to another one (fluorides, chlorides, bromides, ...). The CT energy, however, varies as well inside each of these compound families, an observation that the formula of Jørgensen does not account for. More than three decades later, Boutinaud *et al.* found a linear relation between the energy of a special metal to metal CT, namely an $Pr^{3+} \rightarrow B^{q+}$ ($B =$ transition metal) inter-valence charge transfer (IVCT), and the quotient between the optical electronegativity of the B^{q+} cation and the $Pr^{3+}-B^{q+}$ distance. His formula reflects the trend of IVCT energies inside various transition metal oxides. Following the idea of including the inter-atomic distances, we found a linear relation between the $O^{2-} \rightarrow Eu^{3+}$ CT energies and the $O^{2-} - Eu^{3+}$ distances in both the transition metal oxides, $ABO_4:Eu^{3+}$, and the phosphates, $APO_4:Eu^{3+}$. We could show that our expression for the Eu^{3+} CT energy as well as the formula of Boutinaud for the Pr^{3+} IVCT energy are an extension of the simple optical electronegativity formula given by Jørgensen. Within the energy level diagrams that were introduced by Dorenbos few years ago, the lowest BO_4^{3-} group transition energy should be expressible in the case of the transition metal oxides as the sum of the Eu^{3+} CT and the Pr^{3+} IVCT energies minus the difference between the Eu^{2+} and the Pr^{3+} ground state energies. With this, it becomes apparent that and how the electronic properties of the BO_4^{3-} ion depend on the size of the (rare earth) cation adjacent to it. Yet, the band gap of the orthophosphates $APO_4:Ln^{3+}$ can not be expressed in this manner because they do not show any IVCT excitation bands. Although within the phosphates the band gap energy also shows a dependency on the size of the A^{3+} ion, their generally larger band gap in comparison to the transition metal oxides can not be explained with the same parameters that explain the difference in band gap energies between the latter types of oxides, meaning for instance between the vanadates and the tantalates. The fact that the diverse parameters in Table 1, describing structural and electronic properties, are unable to connect the orthophosphates with the transition metal oxides points to the complexity of the nature of CT transitions.

Samenvatting

Lokaliseren van energieniveaus van lanthanide ionen in anorganische ionische verbindingen

De luminescentie-eigenschappen van lanthanide (Ln) geactiveerde verbindingen hangen af van de locatie van de Ln 4f en 5d energieniveaus ten opzichte van de geleidingsband (CB) en de valentieband (VB) van het betreffende gastrooster. In deze dissertatie zijn drie verschillende energieën bepaald uit experimentele data, waarmee energieniveaudiagrammen kunnen worden geconstrueerd, die deze locaties laten zien: (i) Uit fotoluminescentie (PL) excitatiespectra zijn de energieën van ladingsoverdracht (CT) overgangen tussen twee ionen verkregen; (ii) gebaseerd op PL emissiespectra zijn de activatie-energieën voor temperatuurdoxing van de luminescentie van de activator bepaald; (iii) uit Ln-gerelateerde gloeicurven zijn de thermoluminescentie (TL) activatie-energieën afgeleid. We hebben TL toegepast op twee verschillende typen verbindingen en hebben aangetoond hoe de energieniveaudiagrammen kunnen bijdragen aan een nieuwe TL techniek.

Naast het uit experimentele data construeren van energieniveaudiagrammen voor verschillende verbindingen (hoofdstuk 2 – 4) hebben we onderzocht hoe de luminescentie-eigenschappen van de verbindingen ten opzichte van elkaar veranderen (hoofdstuk 5).

Hoofdstuk 2 bevat een gedetailleerde fotoluminescentie-studie van de orthovanadaten, $AVO_4:Ln^{3+}$ ($A = La, Gd, Lu$; $Ln = Ce, Pr, Eu, Tb$). Hieruit bleek dat de bandkloof-energie, dat wil zeggen de laagste VO_4^{3-} overgangsenergie, ongeveer 0.5 eV hoger is in $LaVO_4$ dan in $GdVO_4$ en $LuVO_4$. Bovendien konden we een observatie in de emissiespectra van $GdVO_4:Ce^{3+}$ en $LuVO_4:Ce^{3+}$, die al in de jaren 60 door Blasse en Brill was gedaan, bevestigen: Hoe kleiner de effectieve ionstraal van A met een zeker omringingsgetal is, hoe verder het maximum van de vanadaat-emissieband is verschoven naar langere golflengten. Geen van PL spectra vertoont 5d-4f emissie of 4f-5d excitatie. Dit duidt erop dat in de energieniveaudiagrammen van $AVO_4:Ln^{3+}$ ($A = La, Gd, Lu$) de 5d toestand van de Ln-doteringsionen zich binnen de CB bevindt. Dat verklaart ook waarom er in de diagrammen van de orthovanadaten $GdVO_4$ en $LuVO_4$ geen $Tb^{3+}:^5D_3$ emissie kon worden waargenomen. Ook de grondtoestandenergieën van de divalente ionen bevinden zich allemaal binnen de CB, behalve die van $LaVO_4:Eu^{3+}$, waaruit volgt dat de orthovanadaten, AVO_4 , geen doteringsionen met oxidatietoestand 2 kunnen bevatten. Om dezelfde reden kunnen deze Ln-doteringsionen niet als metastabiele elektronenval dienen. Aan de andere kant bevinden de

grondtoestandenergieën van Ce^{3+} , Pr^{3+} en Tb^{3+} zich wel boven de VB en kunnen dus dienen als stabiele gatenvallen. Uit een analyse van de temperatuurafhankelijke $Pr^{3+}:^3P_0$ en $Tb^{3+}:^5D_4$ luminescentiedoving kon worden geconcludeerd dat de Pr^{3+} en Tb^{3+} 4f grondtoestanden zich op een vergelijkbare locatie bevinden in de energieniveaudiagrammen ten opzichte van de gastroosterbanden.

Hoofdstuk 3 bevat een gedetailleerde PL- en TL-studie over Ln-mono- en Ce-Ln-co-gedoteerd $NaLaF_4$. Gebaseerd op PL-, TL-spectra en informatie uit de literatuur over het energieverval tussen de $4f^6$ grondtoestandenergie (GSE) van Eu^{3+} en de $4f^7$ GSE van Eu^{2+} in zogenaamde brede-bandkloof-verbindingen is een compleet energieniveaudiagram voor $NaLaF_4:Ln^{3+}$ geconstrueerd. In het geval van Ln-mono-gedoteerd $NaLaF_4$ bleek dat de TL zijn oorsprong heeft in 4f-4f emissie van het Ln^{3+} -doteringsion. $NaLaF_4:Ln^{3+}$ (Ln = Ce, Pr, Tb) vertoont twee TL-banden, terwijl er bij $NaLaF_4:Ln^{3+}$ (Ln = Nd, Dy, Ho, Er) slechts één TL-band zichtbaar is. $NaLaF_4:Ln^{3+}$ (Eu, Gd, Yb) vertoont ofwel geen ofwel zeer zwakke TL. In Ce-Ln-co-gedoteerd $NaLaF_4$ heeft de TL voornamelijk zijn oorsprong in de 5d-4f emissie van Ce^{3+} . De Ln-specifieke gloeicurven konden echter niet verklaard worden met alleen het energieniveaudiagram. Het is aangetoond dat er naast het energieniveaudiagram ook nog twee aannames, namelijk de aanwezigheid van twee gastrooster-gerelateerde elektronenvallen en de aanwezigheid van V_k -centers, nodig zijn om alle Ln-specifieke gloeicurven te verklaren. We hebben geconcludeerd dat (i) een Ln-ion alleen kan dienen als een elektronenval wanneer de $Ln^{2+} 4f^{n+1}$ grondtoestandenergieën zich ten opzichte van de CB onder of dichtbij de activatie-energieën bevinden van de gastroostergerelateerde E1- en E2-elektronenvallen; (ii) een Ln-ion alleen kan dienen als een gaterval wanneer de $Ln^{3+} 4f^n$ grondtoestandenergieën zich ten opzichte van de VB boven V_{kA} -center GSE, E_A , bevinden.

Hoofdstuk 4 bevat door X-ray geëxciteerde emissiespectra en VUV excitatiespectra in combinatie met TL-gloeicurven van zowel $YPO_4:Ce^{3+}, Ln^{3+}$ als $LuPO_4:Ce^{3+}, Ln^{3+}$ (Ln = Sm, Dy, Ho, Er, Tm). Gebaseerd op de emissie- en excitatie-spectra zijn nauwkeurige energieniveaudiagrammen geconstrueerd voor beide typen verbindingen. Uit deze diagrammen hebben we geconcludeerd dat na bestraling met hoog-energetische fotonen of na directe Ce^{3+} excitatie het Ce^{3+} -ion een gaterval wordt. Aan de andere kant kan het vrijgekomen elektron worden ingevangen door het Ln^{3+} co-doteringsion. Zowel de $Ce^{4+}:4f^0$ als de $Ln^{2+}:4f^{n+1}$ grondtoestanden zijn stabiel bij kamertemperatuur. Gedurende verwarmen (van kamertemperatuur tot 500 °C) wordt het ingevangen elektron losgemaakt van de $Ln^{2+}:4f^{n+1}$ GS en recombineert het via de CB met Ce^{4+} . Door deze recombinitie kan Ce^{3+} emissie worden waargenomen. De benodigde activatie-energie om het elektron uit zijn val te halen is afgeleid uit de Ln-gerelateerde gloeipiek. Het energieniveaudiagram laat zien dat de Ln^{2+} GS locaties, die zijn gevonden via TL activatie-energieën, goed overeenkomen met de waarden volgend uit de $O^{2-} \rightarrow Ln^{3+}$ CT banden, die uit de VUV excitatiespectra zijn gehaald. Net als met de eerdere studie over $NaLaF_4$ laat ons werk hier zien dat de geconstrueerde diagrammen gebruikt kunnen worden om TL processen te controleren

Samenvatting

en om nieuwe TL materialen te ontwerpen met betere eigenschappen.

Hoofdstuk 5 bevat tenslotte een verzameling en analyse van de optische- en structuurbetreffende eigenschappen van lanthanide-gedoteerde niet-metallische oxiden van de vorm $APO_4:Ln^{3+}$ en van overgangsmetaal-oxiden met structuurformule $ABO_4:Ln^{3+}$ ($A = La, Gd, Y, Lu$; $B = V, Nb, Ta$; $Ln = La, Ce, \dots Lu$). Veel van deze verbindingen zijn al diepgaand onderzocht in de vorige hoofdstukken. Het belangrijkste doel was om een beter begrip te krijgen van belangrijke parameters zoals bandkloof-energie, d.w.z. de laagste BO_4 groepsovergangsenegie, $O^{2-} \rightarrow Ln^{3+}$ ladingsoverdrachtsenergie of $Ln^{3+} \rightarrow B^{q+}$ intervalentie-ladingsoverdrachtsenergie. Begin jaren 70 heeft Jørgensen aangetoond dat de CT energie tussen een ligand en een centraal atoom grofweg kan worden benaderd met het verschil tussen de zogenaamde optische elektronegativiteiten van deze twee ionen. Zijn eenvoudige uitdrukking beschrijft de trend in CT energieën redelijk goed, gaande van de ene familie verbindingen naar de andere (fluoriden, chloriden, bromiden,...). De CT energie verandert echter ook binnen elk van deze bindingsfamilies. Dit is een observatie waar de formule van Jørgensen geen rekening mee houdt. Meer dan drie decaden later hebben Boutinaud *et al.* ontdekt dat er een lineair verband is tussen de energie van een specifieke metaal naar metaal CT, namelijk een $Pr^{3+} \rightarrow B^{q+}$ ($B =$ overgangsmetaal) inter-valentie ladingsoverdracht (IVCT), en het quotiënt tussen de optische elektronegativiteit van het B^{q+} cation en de $Pr^{3+}-B^{q+}$ afstand. Zijn formule geeft de trend weer van IVCT energieën in verscheidene overgangsmetaal-oxiden. In navolging van het idee om de inter-atomaire afstanden mee te nemen, hebben we een lineair verband ontdekt tussen de $O^{2-} \rightarrow Eu^{3+}$ CT energieën en de $O^{2-} - Eu^{3+}$ afstanden in zowel de overgangsmetaal-oxiden, $ABO_4:Eu^{3+}$, en de fosfaten, $APO_4:Eu^{3+}$. We konden aantonen dat zowel onze uitdrukking voor de Eu^{3+} CT energie als de formule van Boutinaud voor de Pr^{3+} IVCT energie een uitbreiding zijn van de eenvoudige optische elektronegativiteitsformule van Jørgensen. In de energieniveaudiagrammen, die een paar jaar geleden door Dorenbos zijn geïntroduceerd, zou in het geval van the overgangsmetaal-oxiden de laagste BO_4^{3-} groepsovergangsenegie moeten kunnen worden uitgedrukt als de som van de Eu^{3+} CT en de Pr^{3+} IVCT energieën minus het verschil tussen de Eu^{2+} en de Pr^{3+} grondtoestandenergieën. Hiermee wordt duidelijk dat en hoe de elektronische eigenschappen van het BO_4^{3-} -ion afhangen van de grootte van het aangrenzende (zeldzame aarde) cation. De bandkloof van de orthofosfaten $APO_4:Ln^{3+}$ kan echter niet op deze manier worden uitgedrukt, omdat deze geen IVCT excitatiebanden vertonen. Hoewel binnen de fosfaten de bandkloof-energie ook afhankelijk is van de grootte van het A^{3+} -ion, kan hun relatief grotere bandkloof in vergelijking met de overgangsmetaaloxiden niet worden verklaard met dezelfde parameters die het verschil in bandkloof-energieën uitleggen tussen de laatstgenoemde oxiden, d.w.z. bijvoorbeeld tussen de vanadaten en de tantalaten. Het feit dat de verschillende parameters uit tabel 1, welke de structuur- en elektronische eigenschappen beschrijven, niet in staat zijn om de orthofosfaten te verbinden met de overgangsmetaaloxiden, wijst op de complexiteit van het karakter van CT overgangen.

List of Publications

Krumpel A.H., van der Kolk E., Dorenbos P., Boutinaud P., Cavalli E., Bettinelli M., “Energy level diagram for lanthanide-doped lanthanum orthovanadate”, *Mater. Sc. Eng. B*, **146** (2008) 114

Krumpel A.H., van der Kolk E., Zeelenberg D., Bos A.J.J., Krämer K.W., Dorenbos P., “Lanthanide 4f-level location in lanthanide doped and cerium-lanthanide co-doped NaLaF₄ by photo- and thermoluminescence”, *J. Appl. Phys.*, **104** (2008) 073505

Krumpel A.H., van der Kolk E., Cavalli E., Boutinaud P., Bettinelli M., Dorenbos P., “Lanthanide 4f-level location in AVO₄:Ln³⁺ (A = La, Gd, Lu) crystals”, *J. Phys.: Condens. Matter*, **21** (2009) 115503

Krumpel A.H., Bos A.J.J., Bessière A., van der Kolk E., Dorenbos P., “Controlled Electron and Hole Trapping in YPO₄:Ce³⁺,Ln³⁺ and LuPO₄:Ce³⁺,Ln³⁺ (Ln = Sm, Dy, Ho, Er, Tm)”, *Phys. Rev. B.*, **80** (2009) 085103

Krumpel A.H., Boutinaud P., van der Kolk E., Dorenbos P., “Charge Transfer Transitions in the Transition Metal Oxides ABO₄:Ln³⁺ and APO₄:Ln³⁺ (A = La, Gd, Y, Lu, Sc; B = V, Nb, Ta; Ln = Lanthanide)”, submitted to *J. Lumin.*

Acknowledgements

At the end of this work I want to give thanks to all those who have been in many respects an indispensable help to me in the past four years.

I thank my promoter, Pieter Dorenbos, for his kindness, his enthusiasm and his helpfulness. He gave me the possibility to work on this topic and he always lent me his support with professional advice. I also could approach my supervisor, Erik van der Kolk, at any time with all questions. His incomparable patience and competent criticism have contributed to the success of this work. Beside Pieter and Erik, the co-authors of my articles take a considerable part in the content of this work: Marco Bettinelli, Adrie Bos, Philippe Boutinaud, Enrico Cavalli, Karl Krämer, and Dana Zeelenberg. Thank you very much for your critical comments, your help and all the discussions!

I thank all my colleagues for the nice atmosphere and de gezellige momenten: Martijn de Boer, Alastair Cunningham, Marlies Goorden, Jan Heemskerk, Jan Huizenga, Thea Miedema, Romée Kars, Marc Korevaar, José Villena Lozano, Edith Rogers, Dennis Schaart, Stefan Seifert, Gustavo Tapias, Alice Versendaal, Lorette de Vries, Jakob Wallinga. Johan de Haas is an excellent technician, moreover helpful, friendly, and an irreplaceable help not only to most of the Ph.D. students. Folkert Geurink has helped me so many times with my PC, whether my private one or the one at work. José Buurman not only has supported me in the bureaucratic matters but I remember many private conversations we have had. I'll miss a lot the coffee break conversations with Herman van Dam which used to drag out; maybe we can continue them by e-mail... Thank you, Herman, also very much for having translated the summary chapter of this thesis. Candice is unique, and I think she can imagine that I'll miss her very much. I wish her all the best with the new chapter in her life. Thank you to all of you!

There are some former colleagues and friends I always think of with great pleasure: Danang Birowosuto, my room-mate for about three years; Andrea Simon and Alessandra Carrara, my former next-door neighbors; Greg, small but eminently capable.

Piotrek Putaj taught me that aesthetics is not only of philosophy-historical importance. And even though he disliked my shoes, I was on good terms with him. Together with Ivan Khodyuk we have had and hopefully will have many nice dinners together.

During the last months I had a charming room-mate: I want to thank Enrica Seravalli for her support and her understanding. I enjoyed every moment we have been together. Many thanks also to Diane Abou and Christophe Bouvier for all the nice dinners and chats we had! It is nice to know people like them.

Acknowledgements

Marnix Maas has become a good friend of mine. I remember endless discussions about everything and anything, and so many wonderful evenings. He has helped me so many times, and he has also translated the propositions accompanying this thesis. Susana Sarmiento is another very special person that became a close friend of mine. She has also always been there for me and I'm very happy that I got to know her. Thank you both very much.

Zum Schluss möchte ich meiner Familie für ihre Unterstützung und ihr Verständnis danken, besonders meiner Frau Albina: Mein Schatz, ich liebe Dich über alle Maßen. Deine Anwesenheit gibt mir Ruhe, Geborgenheit und Kraft. Ich möchte Dir für Deine kleinen und großen Aufmerksamkeiten danken, für Deine Liebe, Deine Geduld, Deine Uneigennützigkeit und Dein Verständnis, die alles Schlechte überstrahlen und mich immer wieder an das Gute erinnern, an das, was von wirklicher Bedeutung ist.

During my Ph.D. period I have had both good and bad times. The nicest experience I have ever had so far was the birth of my son whom I love above all else. He reminds me every single day how miraculous life is. The saddest experience was the death of two family members and a friend of mine.

Our modern scientific world view does not give satisfactory answers to such experiences, and above all it does not afford consolation.

“The unbelieving sons and daughters of modernity seem [...] to need more, than what is accessible to them, in translation, of religious tradition – as if the semantic potential of the latter was still not exhausted.”¹

In order to avoid a return to the myth we have to be aware of the present one.

*Andreas H. Krumpel
Delft, June 2009*

¹ Habermas J., *Glauben und Wissen*, Suhrkamp Frankfurt am Main (2001) 25

Curriculum Vitae

Andreas H. Krumpel was born on October 20, 1978 in Berlin, Germany. He lived 13 years in South America (Colombia and Mexico) before he obtained his secondary school degree from the today's Hermann-Vöchting Gymnasium in Blomberg, Germany. After that he studied physics at the Westfälische Wilhelms-Universität Münster, Germany, and did his diploma project on "modeling of the operation of quantum gates realized by dipole-coupled semiconductor quantum dots". Post-graduate, he started his Ph.D. research at the Reactor Institute Delft. The results of this research are presented in the thesis at hand.

